INDUCTION COUPLERS: CONTACTLESS ON-ORBIT ACTUATION FOR SPACE ROBOTICS

A Dissertation

Presented to the Faculty of the Graduate School

of Cornell University

in Partial Fulfillment of the Requirements for the Degree of

Doctor of Philosophy

by

Benjamin Zaaron Reinhardt

May 2015

INDUCTION COUPLERS: CONTACTLESS ON-ORBIT ACTUATION FOR SPACE ROBOTICS

Benjamin Zaaron Reinhardt, Ph.D.

Cornell University 2015

Induction couplers exploit eddy-current effects to create force and torque on a target without mechanical contact. Nearly all spacecraft structures include conductive material, so induction couplers may be the closest realizable technology to science fiction's tractor beam: a device that generates contactless force on an uncooperative target.

Contactless forces can potentially enable on-orbit servicing missions that are currently infeasible because they are too dangerous and expensive. On-oribt servicing enables tasks we take for granted on earth but are difficult in space like maintenence, repair, and disposal.

Relative movement between two uncooperative spacecraft traditionally requires either mechanical grapplers or thrusters. Contactless actuators can act in the place of mechanical grapplers in many situations, reducing the risks associated with mechanical contact and sudden non-compliant dynamics coupling. Induction couplers reduce or eliminate the need for thrusters while maneuvering near a larger object — increasing lifetimes, reducing costs, and eliminating risks from plume impingement.

Contactless actuation technology asks three major questions:

- How do you model and characterize dynamic eddy-current interactions?
- How can an inspector use induction couplers to move in six degrees of freedom?

- How do you design an inspection system that can successfully control itself with induction couplers?

This thesis describes solutions to each of these challenges, laying the groundwork for safe and practical on-orbit servicing.Induction couplers can produce millinewton actuation forces with a lower specific power than other contactless actuators. The inspector can move in six degrees of freedom by following trajectories composed of four motion primitives, each with two possible control laws. Finally, a new algorithm based on the idea of controllable volumes informs the inspector's physical layout so that it can maximize the use of its induction couplers.

BIOGRAPHICAL SKETCH

Ben spent his first 18 years in places with the initials N.C. – first Northern California and then North Carolina. He graduated from the North Carolina School of Science and Math in 2006. While he thought he wanted to be a physicist, a summer working in a physics lab taught him that the best part wasn't doing the science, but building the tools: the engineering bug had bitten.

Ben studied Mechanical Engineering and History at Caltech from 2006 to 2010. He spent most of the time learning math and building things - amphibious robots, full-sized Trojan Horses, and ice walls. His history thesis focused on the intimate ties between technology and shifts in culture and politics, specifically the feedback loops between the shifting world of early Medieval Europe and the development and adoption of barrels. During this time, he also worked as an HVAC technician, a cilia-modeling research assistant, and an intern at Aerovironment. Several intense months thinking about amphibious robots and the implications of mobility in Medieval Europe generated a constantly-nagging interest in building new types of locomotion.

That nagging interest (and the fact that it was the next mountain to conquer) lured Ben to the Ph.D. program at Cornell University. There he found an outlet to combine robotic mobility and an often-surprseed obsession with spaceflight in the unconventional approaches of the Space Systems Design Studio. He recieved one of the first NASA Space Technology Research Fellowships to support his research on induction-coupler technology. As part of the NSTRF he worked at both JPL and Ames Research Center on induction couplers and a room-sized microgravity simulator.

Ben plans to give people superpowers and make humanity a space-faring species.

This document is dedicated to anybody seeking superpowers.

ACKNOWLEDGEMENTS

Thank you! to Mason Peck. As my research advisor and committee chair, he was there for me through thick and thin. No idea is too crazy to discuss, nor can any grammar error hide from his eagle eyes. Thank you Mason!

Thank you! to my committee members Ross Knepper and Hadas Kress-Gazit, for focusing my efforts though the research possibility maze. Thank you! to Brandon Hencey, for surrigate advisorship. Thank you! to Brian Wilcox, my ever-patient NSTRF mentor who always kept my eyes on the prize - a free-floating six-dof inspection vehicle.

Thank you! to SSDS lab members past and present: Rodrigo Zeledon, Lorraine Weiss, Zac Manchester, Laura Jones, and especially Joe Shoer who sent me down the eddy-current path in the first place with an incredibly deceptive video.

Thank you! to Terry Fong, who welcomed me to the Ames Intelligent Robotics Group with open arms and Mark Micire who gave me a reason to go to Ames for the first time. Thank you! to Marcia Sawyer, who saved me from bureaucracy a thousand times. Thank you! to Patti Wojeck whose magic made the ride far more smooth. Thank you! to Andy Ruina and Brian Kirby for many meta-ideas and advice. Thank you! to Ephrahim Garcia, who initially lured me to Cornell.

Thank you! to many friends and collegues who helped me on more axes than I can name: Matthew Kelly, Spyros Manipopulos, Tim Lannin, Matthew Sheen, Peter Radrecki, Justin Dobbs, the IRG group, Jon DeCastro, Chris Mavrogiannis. Thank you! to my Mother and my Grandparents, who gave me the drive and grit to both start and finish this whole endeavor.

Thank you! to you, dear reader, for reading this work: I did the research and wrote it down for you, so that you might build upon it and create the world that has never been.

TABLE OF CONTENTS

LIST OF TABLES

LIST OF FIGURES

Preface

> How foolish for a man with metal bones to stand against me
>
> *Magneto*

> Magnetism, as you recall from physics class, is a powerful force that causes certain items to be attracted to refrigerators.
>
> *Dave Barry*

This thesis is a two part exploration into induction coupler technology. The divisions reflect a research arc in which a novel spacecraft actuation technology exposes a nest of robotics problems. Part I introduces induction couplers and explores their unique properties in the context of space applications. Part II looks at the technology more broadly as a dynamical system through a robotics lens.

The Internet has created a brave new world for transmitting knowledge. Digital content enables much richer explanations than those that can be confined to static text. Supplemental materials, along with a copy of this work will be maintained in perpetuity at `www.benjaminreinhardt.com/research`.

Part I

Induction Couplers for Spacecraft Actuation

CHAPTER 1

INTRODUCTION

1.1 What are Induction Couplers?

Induction couplers are actuators that exploit eddy-current effects to create force and torque without mechanical contact. They require only a conductive target. Their ability to actuate near a target with neither propellant nor mechanical contact can provide a completely new way to perform robotic locomotion and manipulation in space. Because most man-made satellites include conductive material in their structure, induction couplers may be the closest realizable technology to science fiction's tractor beam: a device that can produce contactless force on an uncooperative target.

Induction couplers offer two major advantages for spaceflight applications. First, fully deployed spacecraft are fragile and rarely offer straightforward means for mechanical grappling; interactions without the potential for contact damage are valuable. Second, induction couplers operate on electricity alone; they provide the ability to maneuver without propellant, eliminating risks associated with thruster-plume impingement[8] and extending the usable lifetime of the chaser spacecraft.

Induction couplers and induction-coupled spacecraft combine three major research areas: On-Orbit Servicing (OOS), contactless spacecraft actuators, and eddy-current force modeling.

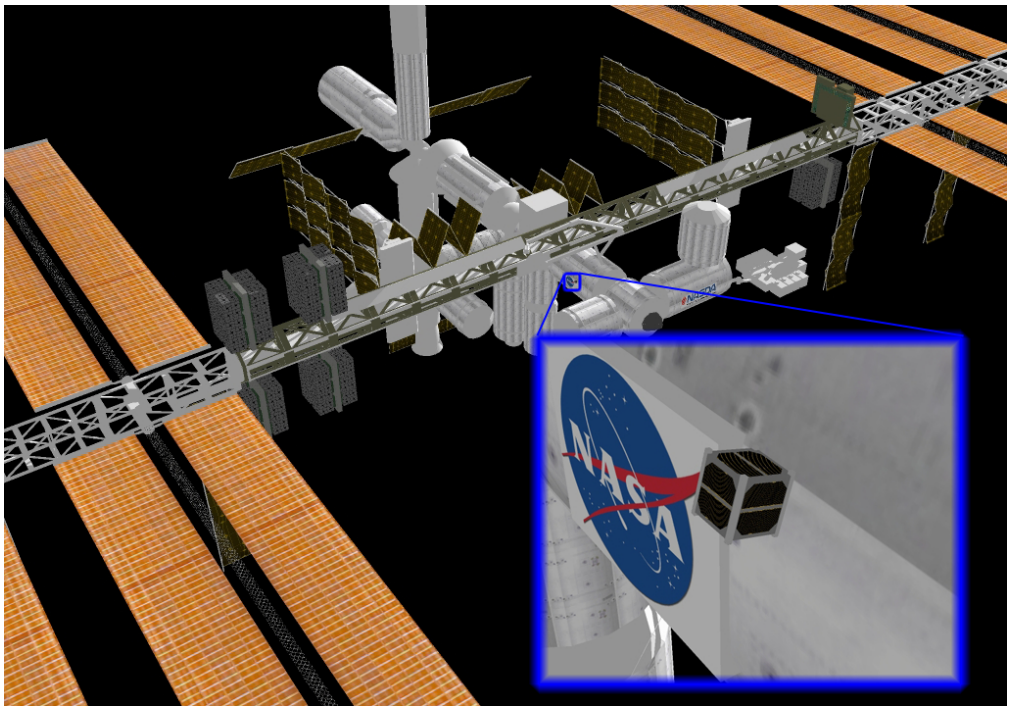

Figure 1.1: A chaser traverses the surface of the ISS using induction couplers

1.2 On-Orbit Servicing

OOS is a valuable but difficult robotic task[19][23]. Just as on Earth, large assets like the International Space Station (ISS) or geostationary satellites experience wear and unexpected problems that require inspection, repair, or refueling[50][115]. These tasks are well suited for robots because it is less dangerous and expensive to send an inspection vehicle to Geostationary Orbit (GEO) or outside the ISS than a human spacewalker[17][2]. Induction couplers can generate force interactions between OOS robots and their targets without mechanical contacts. Contactless actuation has many applications, especially propellantless locomotion.

The benefits of OOS provides strong motivation for advancing induction coupler technology [2] [104]. Underwater autonomous service vehicles regularly inspect pipelines and ships[112], but no such analogy exists in space. A small inspection

spacecraft (Fig. 1.1) can use induction couplers to perform similar tasks. This inspector can fulfill a number of functions: verify spacecraft health; perform mechanical tasks; or provide logistical support for astronauts during Extravehicular Activity (EVA) [17]. The ability to traverse the exterior of the ISS without the constraints of rails, specific attachment points, or finite propellant supplies can free valuable resources like astronaut time and augment overall safety through an increased frequency for inspection and repair. These benefits are not limited to the ISS - a similar inspection spacecraft could enable unique OOS missions to inspect and repair other large satellites.

OOS tasks fall into four major categories [109]: inspection[12], refueling[69], repair[58], and orbit alteration[60]. All of these tasks require a robotic spacecraft to operate in close proximity to the surface of a target. Robotic proximity operations carry significant risk because spacecraft are fragile and respond to impacts with hard-to-predict rigid-body and flexible motions. Thus, it is critical to avoid contact except under controlled conditions.[41]

There are many proposed robotic OOS systems for use on the ISS and other satellites in both Low-Earth Orbit (LEO) and GEO[62]. These include AeroAstro's Escort [38] for LEO, DARPA's Phoenix system for GEO[104], and AERCam [27] [17] and Dextre [19] for the ISS. Recent developments in space robotics have emphasized the cubesat standard for vision systems [108] and planning for capture with robotic arms[24].

Presently, an inspector can use one of three different methods to maneuver close to the surface of its target: it can mechanically grapple the surface to pull itself along; it can use propellant and thrusters; or it can use cooperative, non-contacting electromagnetic systems installed both on the inspector and the target.

Grappling has many potential risks in an uncertain, low-friction environment[66]. Propellant is a finite resource and can damage sensitive surfaces through plume impingement[56][8]. Cooperation is infeasible in many situations because most spacecraft launch without the necessary subsystems: current spacecraft are *not* designed to be inspected or repaired by robots.

1.3 Contactless Actuation

In addition to induction couplers, four major categories of proposed technologies produce contactless forces between a spacecraft and a target: coulomb tethers, Electromagnetic Formation Flight (EMFF) architectures, flux-pinning interfaces, and light-based actuators. All of them use electromagnetic effects to generate force-at-a-distance through a vacuum, but differ in operating principles, range, and application.

Coulomb tethers forces between two or more spacecraft to control satellite formations [92] in both open [63] and closed loop control [65][64]. Coulomb forces can also prevent collisions[110] and deploy fractionated spacecraft systems [74]. EMFF systems use interactions between controlled dipoles to produce inter-spacecraft forces[94, 46]. They have the distinction of being the only contactless actuator with an on-orbit demonstration [80]. Flux-pinned interfaces use the potential wells of magnetic fields embedded in superconductors to control inter-spacecraft positioning[96, 67]. Formation flight[68], docking[53], and on-orbit assembly[28] are two applications of their passively stable configurations.

All of the previous approaches impose pre-launch hardware requirements on each interacting spacecraft. Lasers can produce contactless force on an uncooper-

ative target, either through reflection[7] or potential wells [13][32]. However, lasers are best at manipulating micron-scale spacecraft[54], which makes them impractical for interactions between most spacecraft. At present, mechanical contact is the only general solution for interacting with uncooperative targets, motivating the development of induction couplers as an alternative.

1.4 Eddy-Current Forces

The ISS and most spacecraft are composed of aluminum honeycomb with aluminum facesheets, aluminum isogrid, and aluminum truss elements. Induction couplers exploit this abundance of aluminum through eddy-current force. Specifically, by introducing a changing magnetic field, a robotic inspector can induce eddy currents in these non-magnetic but conductive components and use the reaction force between the field and the currents for actuation[97].

Eddy-currents are an annoyance to be minimized in most applications. They reduce the efficiency of electrical systems and motors, dissipating energy as heat[72] and generating forces opposed to motion. However, these motion-opposing forces can also interact with any conductive surface. This unique capability can propel mag-lev devices[70, 77], and manipulate non-ferrous trash[89], and contactlessly damp unwanted motion[99]. At least two studies have explored the possibilities for passive eddy-current damping on orbit [81, 103], but not active actuation.

Different models of eddy-currents abound, but most are unsuitable for actively controlled spacecraft dynamics because they apply only to narrow situations. Analytical solutions focus on specific geometries and ignore time-varying dynamics[102, 71]. Most numerical methods also ignore time-varying dynamics

and are computationally expensive[39]. Finite Element Analysis (FEA) is the standard approach to solving quasistatic eddy-current problems. However, even those few commercially available FEA packages like `COMSOL` and `ANSYS` that can account for a moving source field are computationally expensive and require hand-tuning for each new geometry. These drawbacks make them unsuitable for dynamic simulations with several degrees of freedom and rigid body dynamics [75].

Paudel and Bird introduced an analytical solution that both relaxes the geometry restrictions and accounts for a moving magnetic source [76]. Their method finds the force between a time-varying, moving magnetic source field and a large flat conductive plate leading to a computationally-lightweight solution for the force from a generic, time-vary magnetic field with a single frequency component.

The steady-state model is a good approximation when

1. There are no interactions between the fields of multiple couplers.
2. The mechanical frequencies are much lower than the propagation speed of the magnetic field through the conductor.
3. The changing magnetic field has only one frequency component.

This thesis simplifies and extends the Paudel-Bird model so that it can easily integrate simulations of complex spacecraft behaviors.

Experimental demonstrations are the real test of any new technology. Even high quality models demand verification, and many unmodeled effects, problems, and lessons manifest during physical experiments. Induction couplers have two attributes that confound experiments: strong state dependence and forces on the order of terrestrial disturbances. These issues motivated the development of a

simple but novel 1-Degree of Freedom (DOF) low-friction test bed.

Air bearing test beds have simulated microgravity dynamics, both translational and rotational, for over 45 years[93]. Traditional planar air bearing systems are ideal for testing 3-DOF dynamics, but have a number of drawbacks that make them unattractive for testing 1-DOF systems like early-stage induction couplers. The second DOF introduces extraneous variables when testing 1-DOF systems. Sensing the state of the 3-DOF system in real-time requires video processing software that is either custom built or expensive[113]. Closed loop control requires on-board computing, adding to the complication of the system[11]. Planar air bearings require extremely flat surfaces and rapidly consume deceptively expensive compressed gas.

Rotational test-beds can also simulate 1-DOF microgravity dynamics. These test-beds consist of a target on the end of a long arm attached to a low-friction rotational axis[101]. The throw over which they can approximate linear translation is limited by the length of the arm. The bearings holding the rotational axis experience more off-axis torque as the arm length increases so the friction increases with the throw of the system. This connection between friction and throw length is the primary downside for eddy-current experiments, which require a large variation in the throw of the system.

1.5 Contributions

Part one contains five primary contributions:

1. A control law that enables a single induction coupler to pull on a target -

chapter 2.

2. An induction coupler model for dynamic motion - chapter 3.
3. Experimental characterization of eddy-current forces from rotating magnetic arrays - chapter 3.
4. Lyapunov stability for eddy-current detumbling - chapter 4.
5. A low-cost system for microgravity experiments - chapter 5.

As a preview, part two contains three additional contributions:

1. The four motion primitives an induction-coupled inspector can use to navigate the surface of a target - chapter 7.
2. Experimental demonstration of induction coupler motion primitives - chapter 7.
3. A new algorithm for simultaneously generating the design and controller for complex dynamical systems - chapter 8.

CHAPTER 2

ATTRACTIVE FORCES WITH A SINGLE MAGNET

This chapter shows why pulling is a hard problem for induction couplers and describes a set of control laws that a single induction coupler to pull on a target.

2.1 Properties of Eddy-Current Forces

Eddy-current forces share several properties, regardless of their source. Two of these properties are especially important to developing eddy-current-based actuators: the asymmetry between attractive and repulsive eddy-current forces and the duality between forces created by electromagnets and permanent magnets.

2.1.1 Governing Equations

The eddy-current forces created by induction couplers are not intuitive to most, so it is informative to build up the model from well-known principles. Maxwell's equations lie at the core of induction coupler's governing equations:

$$\nabla \times \mathbf{E} = -\frac{d\mathbf{B}}{dt} \tag{2.1}$$

$$\nabla \times \mathbf{B} = \mu_0 \mathbf{J} + \mu_0 \epsilon_0 \frac{\partial \mathbf{E}}{\partial t} \tag{2.2}$$

$$\nabla \cdot \mathbf{B} = 0 \tag{2.3}$$

Any material with finite conductivity experiences a voltage gradient in response to a time-varying magnetic field.

$$\mathbf{J} = \sigma \mathbf{E} \tag{2.4}$$

The voltage difference induces a current in the material that in turn generates its own magnetic field. The resulting field has a vector potential that obeys

$$\mathbf{B} = \nabla \times \mathbf{A} \tag{2.5}$$

$$\mathbf{E} = -\frac{d\mathbf{A}}{dt} - \nabla V \tag{2.6}$$

If the conductive plate is linear and simply connected, these governing equations can be combined into a partial differential equation describing the propagation of $\mathbf{A}$ through the plate [97]:

$$\nabla^2 \mathbf{A} = \mu_0 \sigma \frac{d\mathbf{A}}{dt} \tag{2.7}$$

A solution for $\mathbf{A}$ gives B on the surface of the plate and Maxwell's stress tensor can find force between the plate and the magnetic source. Because there is no electric field exterior to the plate, Maxwell's stress tensor ($\overleftrightarrow{\sigma}$) reduces to

$$\overleftrightarrow{\sigma} = \frac{1}{\mu_0}\left[\mathbf{B} \otimes \mathbf{B} - \frac{B^2}{2}(\hat{\mathbf{x}} \otimes \hat{\mathbf{x}} + \hat{\mathbf{y}} \otimes \hat{\mathbf{y}} + \hat{\mathbf{z}} \otimes \hat{\mathbf{z}})\right] \tag{2.8}$$

Where $\otimes$ is the dyadic product. Integrating the stress tensor across the target's surface gives the net force, $\mathbf{F}$ between the surface and the magnetic field (and thus the coupler.) While straightforward, this result is useless for dynamic modeling without the solution to (2.7). Any solution to a three-dimensional time-varying partial differential equation requires numerical methods or assumptions about the problem's geometry. In the 1-DOF case, the simple solution in section 2.1.3 takes advantage assumptions about symmetry and propagation speed. Further on, chapter 3 delves deeper into 3-DOF solutions.

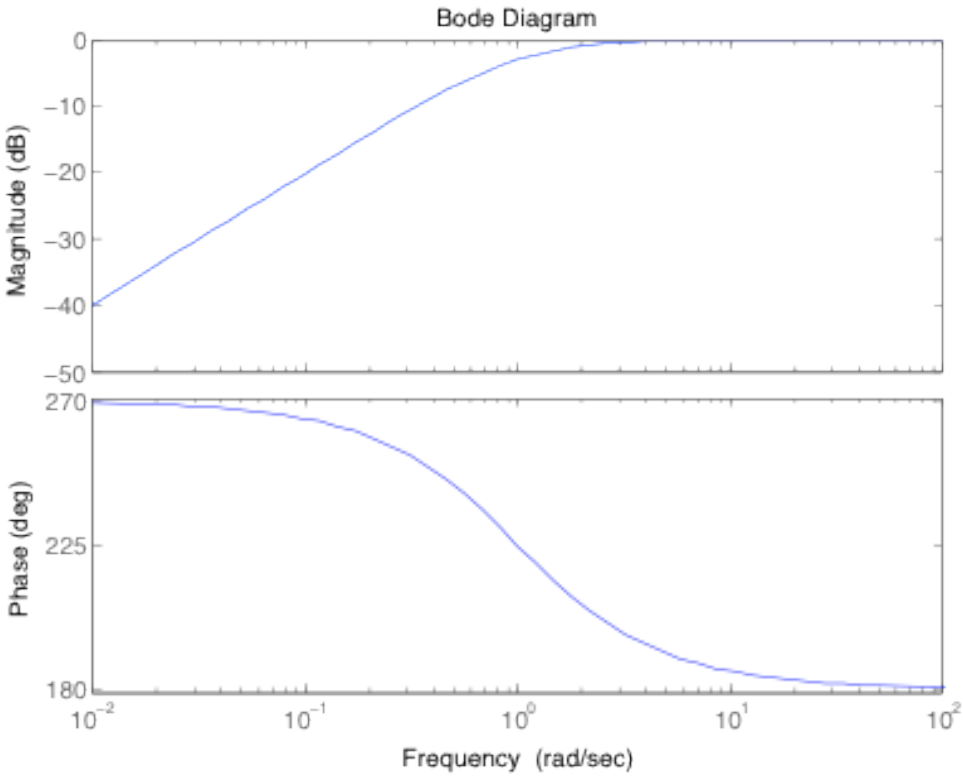

Figure 2.1: Frequency response for an induced current to an applied magnetic field.

2.1.2 Attraction/Repulsion Asymmetry

A demonstration of the eddy currents' ability to produce net repulsive impulses over an actuation cycle is as simple as placing a coil of wire on a conductive surface and plugging it in to the wall. The coil jumps into the air and hovers. Previous work[72] has analytically found a nearly 180 degree phase shift between the oscillating current through an electromagnet and the currents it induces at sufficiently high frequencies. In this case is above 10 Hz. Most frequencies associated with an eddy-current actuator fall into this high frequency range. The near-180 degree difference in phase causes the current density in the conductor ($\mathbf{J}$) and the magnetic field ($\mathbf{B}$) to have the same frequency but opposing signs, so their cross product is always negative. As the force between the actuation magnet and the plate is

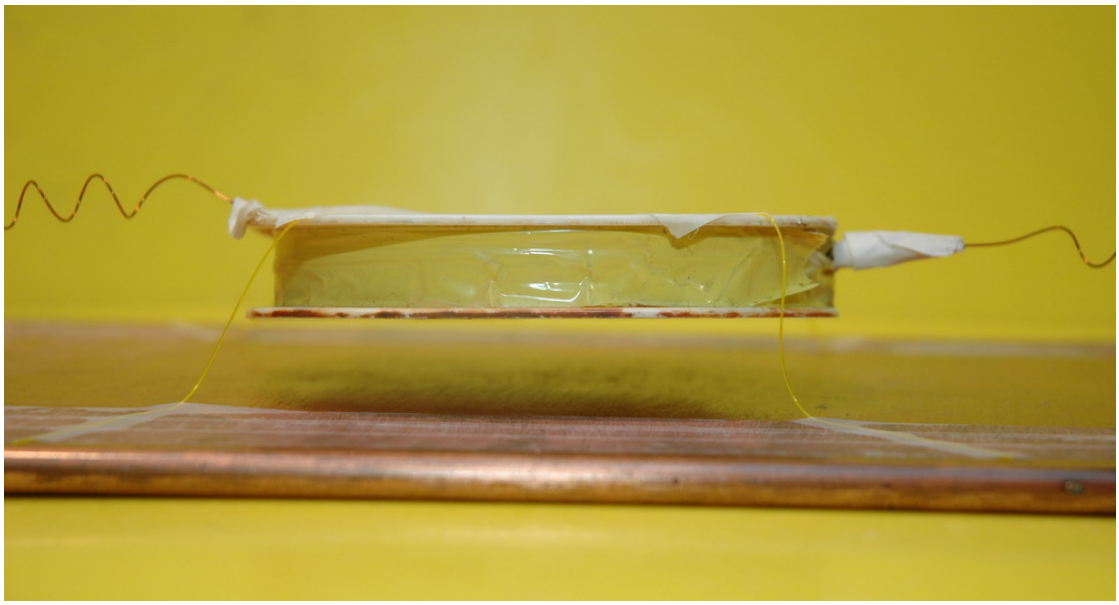

Figure 2.2: An oscillating current levitates a coil over a conductive target.[106]

proportional to the product of the magnetic field and the induced current[102], the magnetic field causes a repulsive force on the conductor. Due to the phase shift between the magnetic field and induced current, any repeating input to the electromagnet-conductor system produces a net repulsive impulse over the cycle in the absence of other dynamics.

Creating a net repulsive momentum transfer to a target with a permanent magnet is as simple as moving the magnet from an effectively infinite distance towards a conductor. A dipole moving at any velocity directly towards a conductive plate with a surface perpendicular to the dipole induces circular current loops in the conductor centered on the line of the magnetic dipole. The net force given by integrating $\mathbf{F} = \mathbf{J} \times \mathbf{B}$ across the entire plate is in the same direction as the velocity of the magnet, and thus produce a repulsive impulse. The same effect can be produced by monotonically increasing the current through an electromagnet near a conductive surface. Clearly, it is simple to produce repulsive forces and impulses with eddy currents induced either by a moving permanent magnet or a

time-varying electromagnet.

Eddy current systems are not incapable of producing attractive forces and impulses - moving a permanent magnet away from a conductor or turning off an adjacent electromagnet imposes an attractive impulse on the target. However, in order to achieve the initial conditions necessary in order to create an attractive impulse, an electromagnet had to be turned on or a permanent magnet brought close to the conductor. As discussed previously, these actions cause a repulsive impulse that in a low-friction space environment that cancels out the subsequent attractive impulse, thus at best producing no net attractive force over the complete set of actions and possibly driving the target away. The implication of this physical reality is that if you approach and leave in the same manner, the cycle is unable to produce an attractive impulse. Conveniently, a magnetic field also induces eddy currents in a target and reduces its momentum if the target has a relative velocity away from the magnet. This damping behavior is the key to a full actuation cycle that produces a net attractive momentum change on a target. The key to creating a net attractive cycle is that it must be asymmetric.

2.1.3 Permanent Magnet-Electromagnet Duality

In the 1-D case, the actuation force, F_{eddy}(t), that can be produced by the relative velocity of permanent magnet and the conductor, $v_m(t)$, is

$$F_{eddy} = C_1 \frac{v_m - v_T}{\|r\|^3} \tag{2.9}$$

The force produced by a current $i_m(t)$ through an electromagnet is

$$F_{eddy} = C_2 \frac{C_3 i \frac{di}{dt} - v_T}{\|r\|^3} \tag{2.10}$$

Thus, with perfect control over the velocity of the magnet, there is a suitable $v_m(t)$ that can produce the same $F_{eddy}(t)$ with a moving permanent magnet as the force produced by an electromagnet. The symmetry of the 1-D case causes the duality between the F_{eddy}(t) generated by electromagnets and moving permanent magnets because the force can be treated as a scalar value that scales with either $v_m(t)$ or $i_m(t)$. For a force caused by some $v_m(t)$, the appropriate choice of $i_m(t)$ can produce the same force and vice-versa, resulting in the same impulse over time. Therefore, any discussion in terms of a moving permanent magnet is applicable to an actuator utilizing an electromagnet as well.

The duality between electromagnets and permanent magnets as eddy-current actuators is useful because it allows for EC actuation schemes to be developed independent of the final implementation of the physical actuator. The duality between eddy currents induced by permanent magnets and electromagnets allows the following discussion of the proof-of-concept actuation cycle to be framed only in terms of a moving permanent magnet because descriptions of maneuvers are simpler and easier to visualize when described in terms of an actuator using a controlled permanent magnet. It is critical to remember that many conclusions for an actuator using a moving permanent magnet apply to an actuator using a controlled electromagnet as well.

2.2 Attractive Actuation Cycle

In order for eddy currents to be used in an actuator, they must be able to transfer momentum to the target in both the attractive and repulsive directions with respect to the actuator. While instantaneous attractive forces are possible, producing a

net attraction over a closed cycle is not possible for system with a fixed target. However, it is possible to achieve the attractive momentum transfer necessary for a successful actuator through a multi-step actuation cycle that takes advantage of the eddy force dynamics combined with the free body dynamics of the system. This section establishes the conditions that a cycle must meet in order to have successfully attracted the target, outline the general cycle, and then go into greater detail with a sample actuation cycle.

2.2.1 Cycle Conditions

In the most general case, the initial conditions which lead to successful attraction are those for which there is a time history of actuation commands to the magnet, $v_m(t)$, that lead to "successful" final conditions of the cycle. A successful cycle is one in which has the following two final conditions:

1. The momentum of the target experiences a net change in the direction of the magnet.
2. The magnet starts and ends the cycle far from the target.

Condition (1) ensures that either the target has been captured and is moving towards the magnet at the end of the cycle, or that over repeated successful cycles, the momentum of the target can be changed to be in the direction of the magnet. Condition (2) is necessary because for an actuation cycle to be complete and repeatable the magnet must start and end the cycle in the same place and logically any actuator magnet must be brought near the plate from somewhere else to initiate the actuation. Due to the r^{-3} nature of the eddy current force[86],

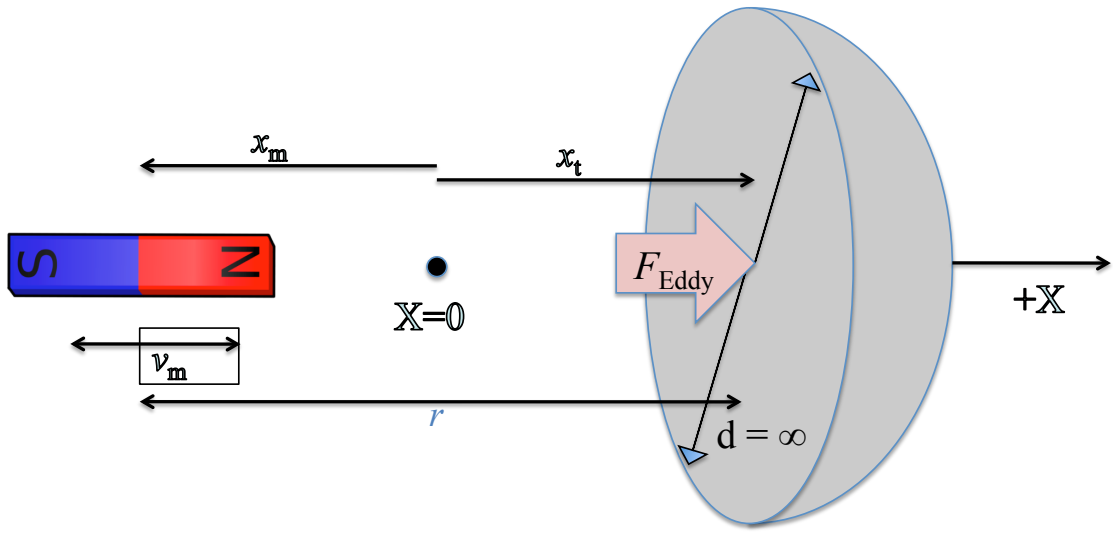

Figure 2.3: Diagram for attraction-cycle model.

F_{eddy} decreases quickly with the distance to the target. Thus, a magnet that is effectively infinitely far away does not have to be a large physical distance from the plate, making this condition applicable to real situations.

2.2.2 Model Assumptions

The attractive force actuation cycle uses a simplified model (Fig. 2.3) for demonstration purposes. This model is built on a number of assumptions that simplify the system in order to illustrate the underlying dynamics but does not alter the fundamental results as they are removed or made more complicated.

1. The model produces a changing magnetic field through a moving permanent magnet. The position and velocity of the magnet are directly controlled.
2. The model has a single translational DOF in which the magnet and target plate move along the Z-axis with the magnet in the Z direction of the target.

3. There is a fixed coordinate system with its origin at the target's initial position.

4. The model assumes no friction.

5. The target is a conductive half sphere oriented with its face towards the magnet that has a finite mass mt but an infinite radius.

6. When calculating F_{eddy}(t) the model finds the instantaneous force at each time t rather than solving the full PDEs that dictate the propagation of the magnetic field and induced eddy currents within the conductive material.

2.2.3 Justifications for Model Assumptions

Assumption (1) makes the model more physically intuitive than one in which the actuation forces are provided by an electromagnet. It is easier to discuss forces that depend only on relative motion between a magnet and a target than forces dependent on a combination of relative velocity and an electromagnetically generated field's magnitude and rate of change. The external control of the magnet's position and velocity can be physically realized by moving a permanent magnet on a rail or with thrusters. Assumption (2) simplifies the model without limiting its applicability. The model does not need more than one translational DOF magnetic fields and currents can be linearly superimposed, so the actuation cycle can be generalized to multiple degrees of freedom.

Assumption (4) is valid because the actuation cycle takes place in space - a very low friction environment. Assumption (5) allows F_{eddy}(t) to be calculated analytically and for analytical conversion between the $v_m(t)$ of a moving permanent magnet and the $i_m(t)$ of an electromagnet. Force calculations with an infinite

radius are not a large deviation from the physical situation because the magnetic field drops off quickly away from the dipole axis and the skin effect causes the current to decrease exponentially with depth inside the conductor. Thus, although the forces on parts of the target, which would not actually exist, are calculated, their contribution to the total force is very small.

Assumption (6) is justified because:

1. The relative permeability of aluminum is very close to one so the magnetic field propagates at close to the speed of light, which for the centimeter to meter scales of the problem is effectively instantaneous.
2. The frequency of the actuation cycle (0.1 Hz) is shorter than the frequencies at which force hysteresis caused by induction occurs (3 Hz) by an order of magnitude.[6]
3. Due to the symmetry of the problem, the magnetic field from the eddy-currents themselves acts only as a scaling factor to the total force. [100]

2.2.4 Cycle Creation

It is clear that simply moving a magnet towards the plate and then immediately pulling it away at the same speed does not produce a net attraction moving the magnet towards the plate initially repels the plate, increasing the distance between the plate and the magnet, and thus decreasing the magnitude of the attractive forces when the magnet is then drawn away. The repulsive forces caused by moving the magnet towards the plate and subsequent increase in separation distance means that any actuation cycle that does not take advantage of the dynamics of the

plate-magnet system is unable to produce a net attractive force. Thus, in order to produce net attraction, an asymmetric actuation cycle is necessary.

However, EC forces are inherently non-conservative, and introduce damping into the relative motion between the magnet and the target. An actuation cycle can use the damping effect to dissipate some of the momentum imparted to the target when the magnet is moved in from infinity. Thus, a net attraction between a magnet and the actuation target can be achieved by taking advantage of the damping of relative velocity between the two due to the eddy forces.

2.2.5 Attraction Cycle Phases

The proposed actuation cycle can be broken down into three steps that together make a continuous cycle - the initial conditions of each step are the final conditions of the previous step. The three phases of the cycle and the time intervals associated with them are:

1. Approach Phase ($t_0 \leq t < t_1$)
2. Capture Phase ($t_1 \leq t < t_2$)
3. Pull Phase ($t_2 \leq t \leq t_3$)

The following section first presents the outline of each and its role in creating a complete cycle that causes a net attractive force on the target. Following the outline are results of a simulation that works backwards through the cycle in order to determine the region in phase space for which the target can be successfully attracted. The state variables of the system are the position (x_m) and velocity (v_m) of the actuating magnet as well as the position(x_T) and velocity (v_T) of the

conductive target. These coordinates are measured in an inertial reference frame with $x = 0$ at the initial position of the target. The mutual force caused by the interaction between the magnetic field and the induced currents in the target (F_{eddy}) is calculated at the target. This force is proportional to where r is the relative position of the magnet and the target - $r = x_m - x_T$.

Approach Phase

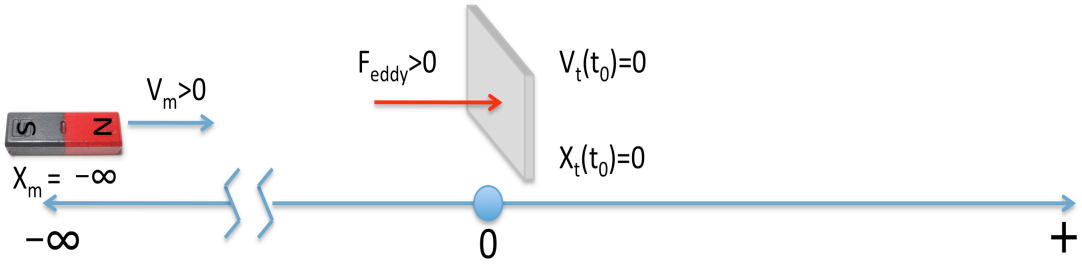

Figure 2.4: System at beginning of approach phase $t = t_0$

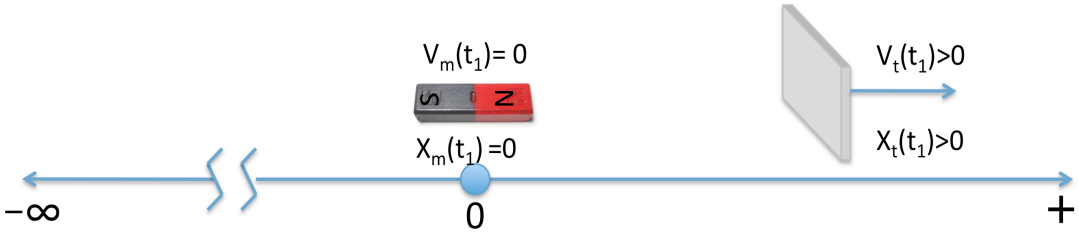

Figure 2.5: System at end of approach phase $t = t_1$

In order to create a complete and repeatable cycle that reflects a physical situation, the magnet must begin and end the cycle at $x_m = -\infty$. This initial state is intuitive because any magnet has to approach the target from a distance that is effectively infinite, or in the case of an electromagnet, the current must be increased from zero to some finite value. For all cycles, $x_T(t_0) = 0$ and $v_T(t_0)$ is

unconstrained - the initial velocity of the target determines whether it is possible to capture and subsequently pull the target.

During the approach phase, the magnet approaches the target at some $v_m > 0$. Assuming $v_m > v_T$ (otherwise the magnet would remain infinitely far from the target) this causes $F_{eddy} > 0$ and the magnet accelerates to the right. This positive acceleration is an unfortunate necessity in order to decrease r so that the magnet can produce a non-trivial F_{eddy} to the left on the target later in the cycle.

At the end of the approach phase, the magnet stops at $x_m(t_1) = 0$ in order to begin the capture phase. The exact value of this stopping point is for illustrative purposes and would change based on the application of an implemented cycle. The target continues to move in the positive direction with $v_T(t_1) > 0$.

Capture Phase

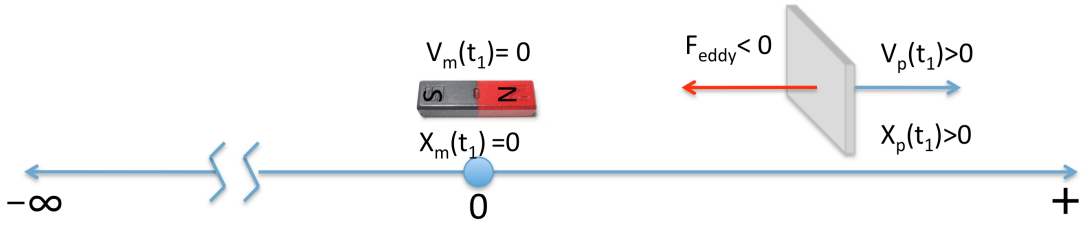

Figure 2.6: System at beginning of capture phase $t = t_1$

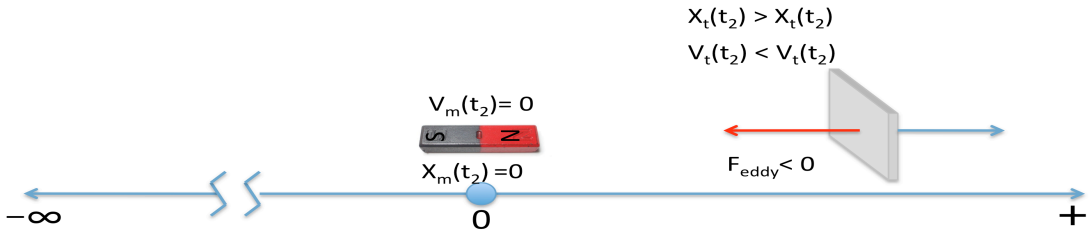

Figure 2.7: System at end of capture phase $t = t_2$

The goal of the capture phase is to use the damping that occurs between the

stopped magnet and the moving target in order to reduce $\frac{dr}{dt}$. This reduction in the momentum of the target creates a situation in which F_{eddy} has a sufficiently large magnitude to make $v_m < 0$ when the magnet moves to the left, achieving a successful final state with the magnet moving to the left.

At the beginning of the capture phase, the state of the system is the same as at the end of the approach phase. The magnet is held at $x_m(t_1) = 0$ with $v_m(t_1) = 0$ and the target is at some positive position $x_T(t_1) > 0$, moving with $v_T(t_1) > 0$.

During the capture phase, the magnet is held at $x_m = 0$ by an external force. F_{eddy} acts as a damping force on the target as $\frac{dr}{dt} < 0$ and the $v_m = 0$. At the end of the capture phase the magnet has not moved from the origin, $x_m(t_2) = 0$ and $v_m(t_2) = 0$. The target remains to the right of its starting position, $x_T(t_2) > 0$, with a positive velocity, but $v_T(t_2) < v_T(t_1)$ which makes the future impulse imparted by pulling the magnet to the left larger than the momentum of the target.

Pull Phase

The goal of the pull phase is to successfully cause v_m to change direction. This change in the direction of the target velocity is achieved when F_{eddy} finally imparts an impulse to the target sufficient to reduce its momentum below zero, thus completing the goal of the actuation cycle.

At the beginning of the pull phase, the magnet is still at the origin, $x_m(t_2) = 0$ and begins moving to the left with $v_m(t_2) < 0$ until it returns to its position at the beginning of the cycle: $x_m(t_3) = x_m(t_0) = -\infty$. At the beginning of the phase the target is located at a position to the right of the origin and has a positive velocity. As the magnet moves from $x_m(t_2) = 0$ to $x_m(t_3) = -\infty$ the resulting

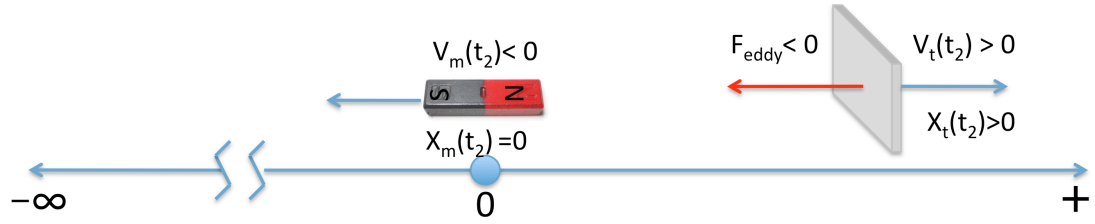

Figure 2.8: System at beginning of pull phase $t = t_2$

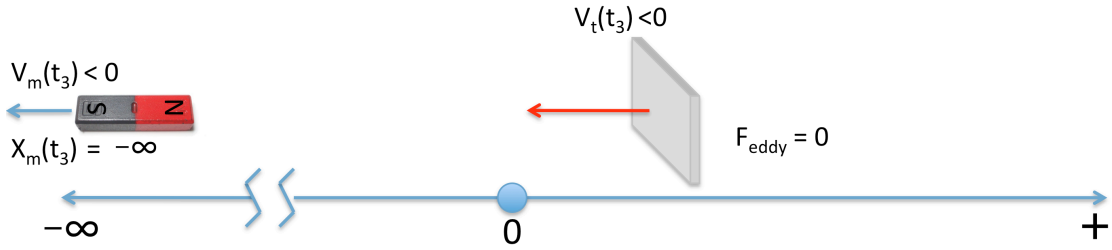

Figure 2.9: System at end of pull phase $t = t_3$

$\frac{dr}{dt} < 0$ causes F_{eddy} to be to the left, imparting a negative impulse on the target, which makes $v_m(t_3) < 0$ if the cycle has successfully attracted the target. The cycle has successfully attracted the target even if $x_T(t_3) > 0$ because the fact that $x_m(t_3) = -\infty$ means that $\|r\| = \infty$ and $F_{eddy} = 0$ so that eventually the fact that $v_T(t_3) < 0$ causes $x_T(t > t_3) < 0$ which is the goal of an attractive actuation.

The condition of the pull phase in order for the cycle to successfully attract the target is that before $\|r\|$ becomes large enough that F_{eddy} is negligible, the impulse imparted by the magnet as it moves to the left must be greater than the momentum of the target at t_2.

2.3 Successful Attraction Cycle

A given EC actuation cycle cannot successfully attract a target for every initial $v_T(t_0)$. The actuation cycle fails to attract the target if the magnet cannot move

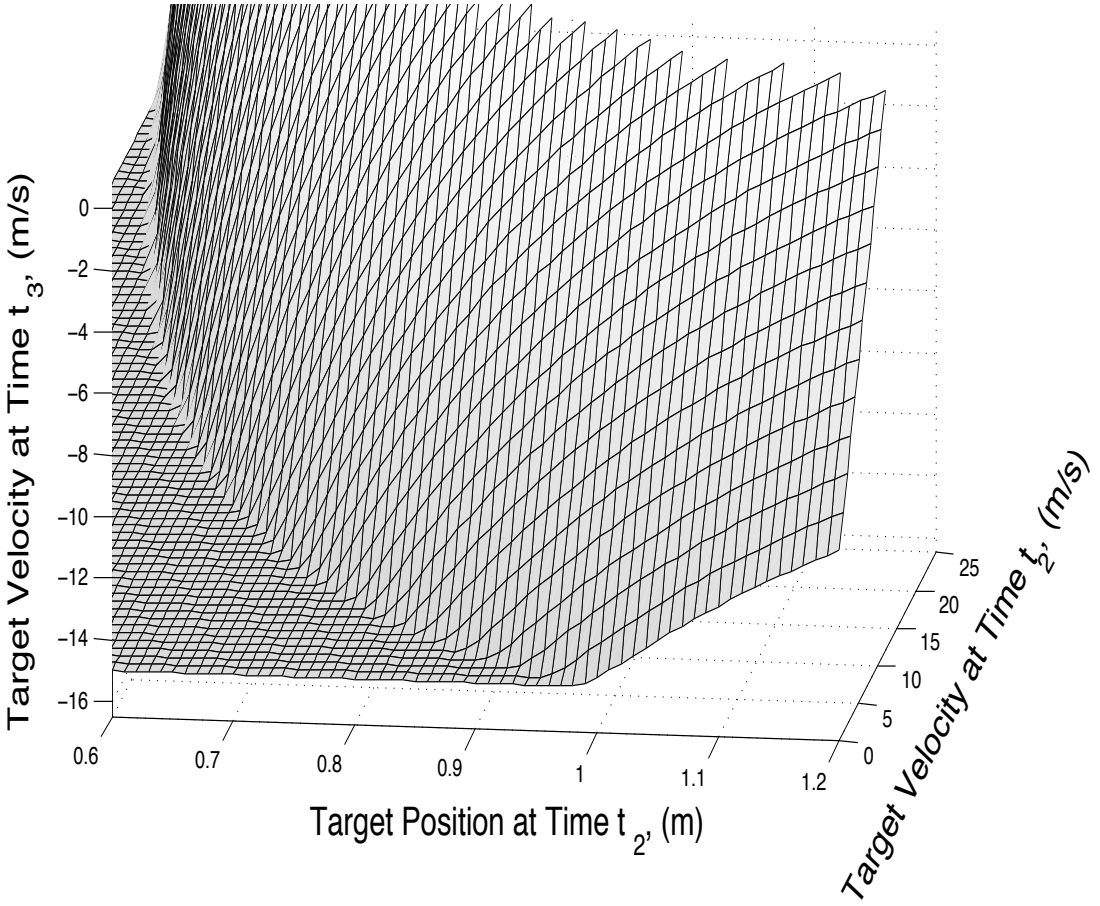

Figure 2.10: Final target velocity as a function of initial target conditions for $v_m = -15$

faster than the target or the target gains too much velocity due to the approach of the magnet. Due to the three discrete phases of the cycle, the desired final conditions of each phase are those that correspond to successful initial conditions of the following phase. These successful initial conditions are those that lead to the desired final conditions of the phase in question. Ultimately, the initial conditions of the target which allow for successful attraction are those which can be affected by a given magnet and its associated properties such that at the end of the cycle $v_T(t_3) < 0$.

Fig. 2.10 shows a plot of the initial conditions for the pull phase that result in

a successful complete cycle. The method used to determine the set of initial $v_T(t_0)$ can be successfully attracted works backwards through the cycle in three discrete steps corresponding to the phases of the cycle, in a manner similar to backwards dynamical programming. At each phase, this method finds the initial conditions of that phase which propagate through the dynamics of that phase into the desired final conditions of that phase. These initial conditions then become the desired final conditions of the previous phase. Thus, the successful final condition of the cycle ($v_T(t_3) < 0$) yields the initial conditions that can lead to successful attraction of the target.

This section presents the process of solving for the initial conditions leading to successful attraction for a sample open-loop actuation cycle. Each phase of the cycle has a key control parameter: $v_m(t)$ during the approach phase, $t_2 - t_1$ during the capture phase, and $v_m(t)$ during the pull phase. These are constant throughout each phase. Each simulation varied the parameter values to demonstrate effect of their variation. Differences in the actuating magnet's motion have significant effects on the viable initial conditions of each phase.

Simulation of the pull phase yields a set of initial conditions ($x_T(t_2)$, $v_T(t_2)$) that can lead to $v_T(t_3) < 0$. Due to the r^{-3} nature of axis-symmetric eddy-current forces, relatively small increases in $x_T(t_2)$ as compared to $v_T(t_2)$ results in $v_T(t_3) > 0$ and the failure of the cycle to successfully attract the target. A graph of $v_T(t_3)$ on the z axis vs. $v_T(t_2)$ and $x_T(t_2)$ (Fig. 2.10) shows that the final velocity monotonically increases with the initial conditions of the pull phase. The monotonic nature of the relationship between the initial and final conditions in the pull phase means that all successful initial states of the pull phase are all those which lie below the line $v_T(t_3) = 0$ projected onto the $v_T(t_2)$ $x_T(t_2)$ plane. Points

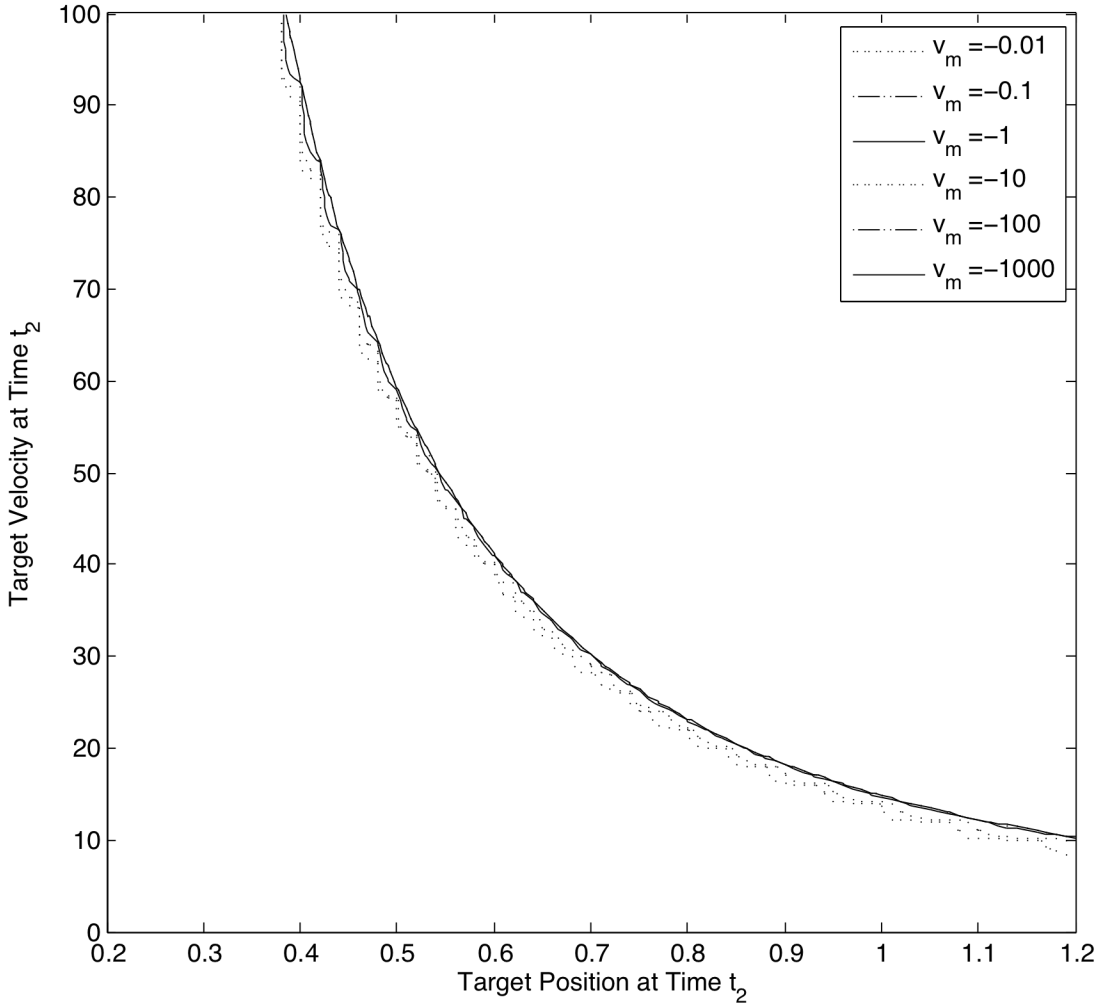

Figure 2.11: Initial conditions of the pull phase yielding $v_T(t_3) = 0$ for varying magnet pull velocities.

lying below this line are the desired final states of the capture phase.

Fig. 2.11 shows the critical $v_T(t_3) = 0$ line for a number of constant magnet pull speeds that vary over several orders of magnitude. Note that the shape of the curve barely changes despite the large range of pull speeds. This invariance to change in the speed of the magnet indicates that the magnet quickly leaves the r-values for which F_{eddy} is significant with respect to the momentum of the target and instead the initial conditions of the target($x_T(t_2)$, $v_T(t_2)$) dominate the pull

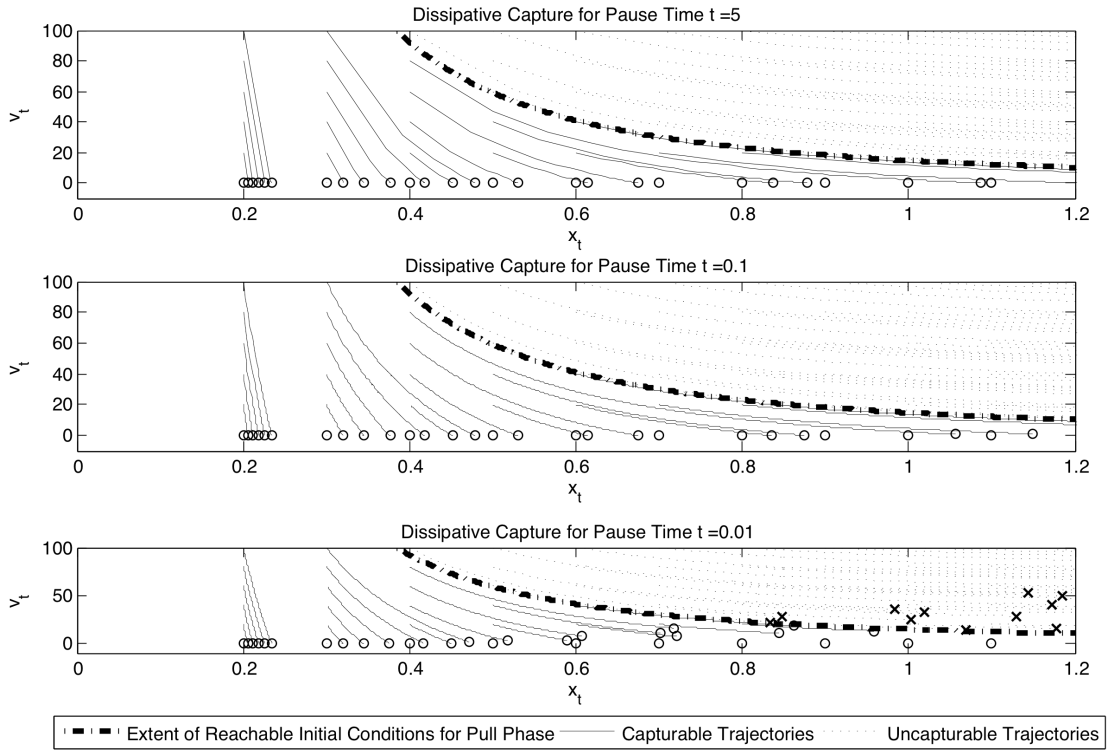

Figure 2.12: Capture phase for different magnet pause times ($t_2 t_1$) showing trajectories that lead to a net attraction.

phase.

Continuing the process of backwards dynamical programming, a simulation of the capture phase yielded the set of ($x_T(t_1)$, $v_T(t_1)$) which propagates to the line of ($x_T(t_2)$, $v_T(t_2)$) that in turn propagates to $v_T(t_3) = 0$ in the pull phase. Three simulations of varying initial conditions of the capture phase (Fig. 2.12) demonstrate the effect of varying $t_2 - t_1$, the pause time during which the magnet holds still at zero in order to dissipate energy after approaching the target. The contrast between the successfully attracted initial conditions in $t_2 - t_1 = 0.01$ and $t_2 - t_1 = 0.1$ but the relative similarity between those in $t_2 - t_1 = 0.1$ and $t_2 - t_1 = 5$ is noteworthy. The intuitive conclusion is that for any pull phase $v_m(t)$ profile, there is a point during the capture phase at which all the energy that can

be dissipated by eddy-current interactions has been dissipated, and the target has either escaped the region in which F_{eddy} is large enough to have an effect, or has been reduced to a very small v_T within that region.

The process for finding the desired set of $v_T(t_0)$ at the beginning of the approach phase which leads to a successful attraction is essentially the same as for the capture and pull phases except that $x_T(t_0)$ is always zero due to the choice of the reference frame. The set of initial conditions, $v_T(t_0)$, which leads to successful attraction over the entire cycle are those which propagate to points below the line of ($x_T(t_1)$, $v_T(t_1)$) found in the capture phase. This is the actual set of initial conditions that allow the target to be captured by this proof-of-concept cycle.

A notable trend in the set of attractable initial conditions arises when the approach speed of the magnet is varied over a number of simulations. The changes in the approach speed have a significant effect on the set of attractable $v_T(t_0)$; increasing the approach speed increases the highest values of the set of $v_T(t_0)$ that can be attracted, but also increases the lowest value of the set. Thus, there is a trade-off between the approach speed of the magnet and the range of $v_T(t_0)$ that can be successfully attracted over the course of the actuation cycle.

The relationship between the approach speed and the set of $v_T(t_0)$ that can be attracted is one of great interest, as it can lead to control laws for an attractive eddy-current actuation cycle. The relationship can be framed in terms of the energy imparted to the target by the approaching magnet (which increases v_T) and the ability of the magnet to affect the target over the rest of the cycle dominated by $r(t_1)$.

In situations where $v_T(t_0)$ is small, a lower $v_m(t)$ (top half of Fig. 2.13) min-

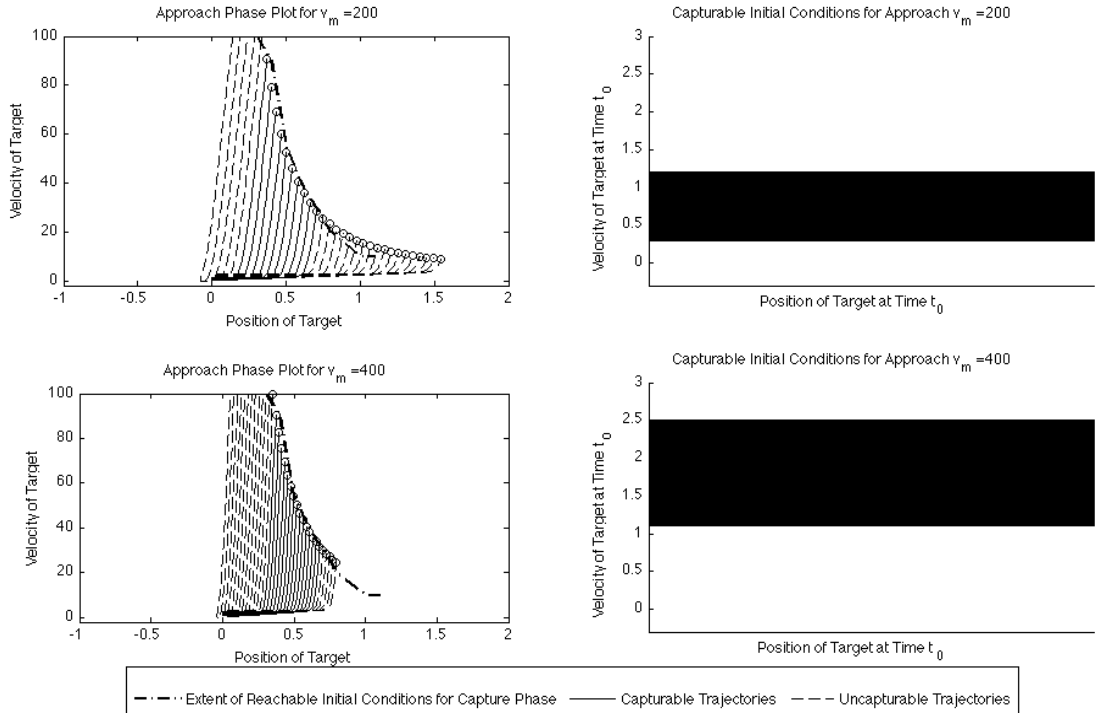

Figure 2.13: Plots of approach phase for different approach speeds (Left) and the initial conditions of the target at time t_0 that leads to a successful capture (Right).

imizes the amount of energy imparted to the target, while still not moving the target out of the range of r in which the magnet can affect the target. However, in this same situation of a lower $v_m(t)$ a target with a higher $v_T(t_0)$ already has a large amount of energy. The energy added to the target by the approaching magnet is smaller with respect to its initial energy and instead the possible F_{eddy} is dominated by the fact that $r(t_1)$ is much larger because the target had more time to move away as the magnet approached it.

In situations with small $v_T(t_0)$ in which $v_m(t)$ is larger (bottom half of fig. 9), the target gains large amounts of kinetic energy because r quickly becomes small and the target and magnet interact for longer. The kinetic energy transferred to the target in this situation is sufficient to cause $\frac{dr}{dt}$ to become large enough that F_{eddy} is very small before the energy of the target can be damped out by F_{eddy}.

Increasing $v_m(t)$ when approaching targets with larger $v_T(t_0)$ still increases their kinetic energy, but as a smaller fraction of their original kinetic energy. The dominant effect, rather than the increase in kinetic energy, is that a larger $v_m(t)$ causes $r(t_1)$ to become small enough that F_{eddy} can successfully interact with the target over the rest of the cycle. The relationship between $v_m(t)$ and both low and high $v_T(t_0)$ can be seen graphically in fig. 9 by noting how trajectories with lower $v_T(t_0)$ become unattractable with high $v_T(t_1)$ and low $x_T(t_1)$ whereas trajectories with higher $v_T(t_0)$ become unattractable with low $v_T(t_1)$ and high $x_T(t_1)$. A quantitative relationship is beyond the scope of this proof-of-concept cycle, but the results still provide a valuable intuition into the cycle.

2.4 Conclusion

This chapter shows how an induction coupler can both push and pull on a target. While induction couplers can easily repel a target with a pulsed or a sinusoidal input, generating attractive forces is more complicated. A net attractive force requires a three-phase cycle that takes into account the damping dynamics of the eddy-current system, as demonstrated by the proof-of-concept actuation cycle. The ability of the cycle to successfully attract a target depends on the relationship between a number of parameters: the initial kinetic energy of the target, determined by $v_T(t_0)$; the amount of energy that the approaching magnet transfers to the target, determined by $v_m(t)$; and the ability of the magnet to damp out the energy of the target through F_{eddy}, determined by $r(t_1)$. An initial magnet velocity $v_m(t)$ that is too great causes the target velocity at the end of the capture phase, $v_T(t_1)$, to be too large for F_{eddy} to stop the target before the relative separation becomes too large for F_{eddy} to affect the target. On the flip side, a $v_m(t)$ that is too

small allows $r(t_1)$ to become too large for F_{eddy} to have a significant effect on the targets trajectory. This chapter describes the actuation cycle in terms of a moving permanent magnet for simplicity and physical intuition, but an electromagnet-based coupler could achieve the same effects. The duality between electromagnet and permanent-magnet induction couplers is important to keep in mind. Attraction/repulsion aysmmetry is only one characteristic where the same conclusions apply to both electromagnet and permanent magnet induction couplers.

CHAPTER 3

INDUCTION COUPLERS FOR ON-ORBIT INSPECTION

This chapter describes induction couplers in more detail, models their state-dependent forces, and describes design considerations driven by the important system properties in in section 3.1. Experiments validate the model and provide measurements of power consumption and force output in section 3.2. Finally, section 3.3 shows how an inspection spacecraft can traverse a planar surface in simulation.

3.1 Induction Coupler Behaviors

An induction coupler exerts force by creating a time-varying magnetic field that induces eddy currents through the conductive materials in a target. The field then exerts a force on these currents and through them, the target (Fig. 3.1). These forces have many dependencies, but most relevant is their strong coupling to the configuration of inspector and its target. This section discusses how to model an induction coupler, its properties, and the resulting design considerations for an induction-coupled spacecraft.

3.1.1 Force Model

There are many solutions for the time-varying magnetic potential $\mathbf{A}$ in section 2.1.1; few of them can find forces in situations where the field's geometry changes over time in the target's frame. The solution in [75] solves the geometry problem

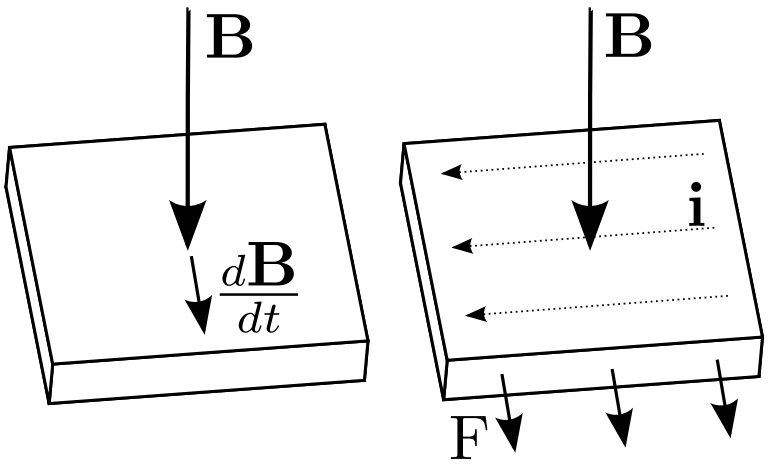

Figure 3.1: Graphical intuition for eddy-current forces.

and analytically solves for **A** and **F** due to a moving magnetic source, agnostic to the field's geometry. While valuable, the solution in [75] finds two separate forces (F_x and F_z) with respect to the target surface. This form is still unsuitable for spacecraft applications, which need a three-dimensional force as a function of the coupler's orientation and position.

A useful model of induction-coupler forces for spacecraft dynamics emerges from a combination of the solution in [75] with a few simplifying assumptions. In this situation, an induction coupler with an axis of symmetry perpendicular to a conductive target surface surface produces a time-varying magnetic field, generating a force between itself and the target. Fig. 3.2 shows the situation.

$$\mathbf{F} = C\left[(1-\beta)\,\hat{\boldsymbol{a}}\times\hat{\boldsymbol{n}} + \beta\hat{\boldsymbol{n}}\right]\omega \tag{3.1}$$

ω is the coupler's frequency, $\hat{\boldsymbol{a}}$ is its axis of symmetry, $\hat{\boldsymbol{n}}$ is a vector normal to the surface. C is a scale factor on the the force **F** that accounts for factors other than a coupler's input speed. C is a function of the magnet properties, target properties, and the separation between the coupler and the surface, g. β is the thrust ratio between the components of the force perpendicular and tangent to the target's surface. When ω is small, β is negligible, creating a force approximately tangential

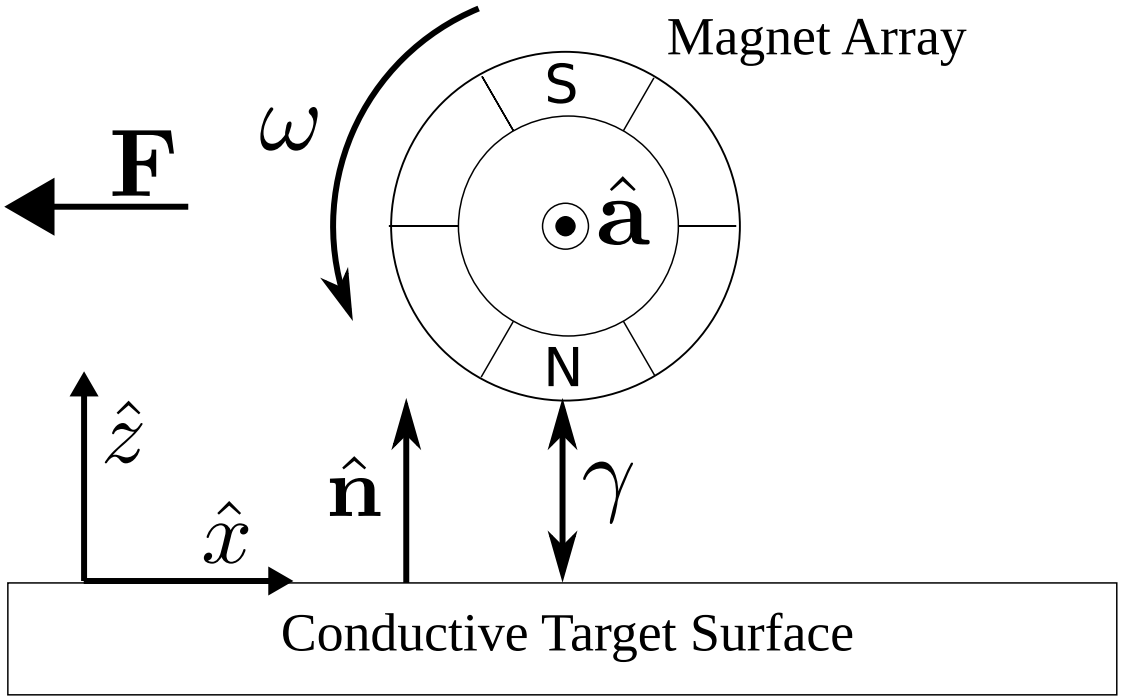

Figure 3.2: Diagram for a single induction coupler seen along its spin axis

to the target surface in both the simplified and full force model (Fig. 3.3). The model's simplifying assumptions are:

1. The frequency and translational speed of the coupler are both small. At low speeds, the relationship between **F** and ω is approximately linear.
2. The coupler's axis remains perpendicular to the target's surface.
3. The coupler is close enough to the target that its surface is effectively an infinite plate.

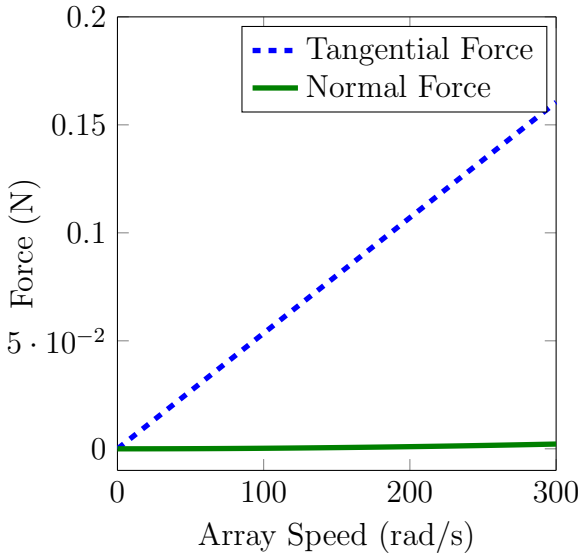

Figure 3.3: Shear and normal forces on the induction coupler from unsimplified model.

3.1.2 Design Considerations

Induction couplers can generate time-varying magnetic fields with either mechanically moving permanent magnets or electromagnets driven by time-varying currents. Each type of magnet excels at producing forces in certain directions. A single electromagnet can produce forces directly away from a target [85], while rotating permanent magnets primarily produce shear forces (Fig. 3.3). The experiments and simulations in this chapter focus on permanent-magnet couplers and their shear forces to produce actuation in a plane parallel to a target.

Permanent-magnet induction couplers operate by spinning permanent magnets with a varying speed, ω. The array spins about an axis $\hat{\boldsymbol{a}}$ near a conductive surface with a normal vector $\hat{\boldsymbol{n}}$ (Fig. 3.2). The many dependencies in induction-coupler forces create several design tradeoffs. Increasing the number of dipoles in the array increases $|\mathbf{B}|$ while decreasing $\nabla\mathbf{B}$, leading to a tradeoff between the time-averaged field strength and $\frac{d\mathbf{B}}{dt}$. Additionally, the array can either consist of

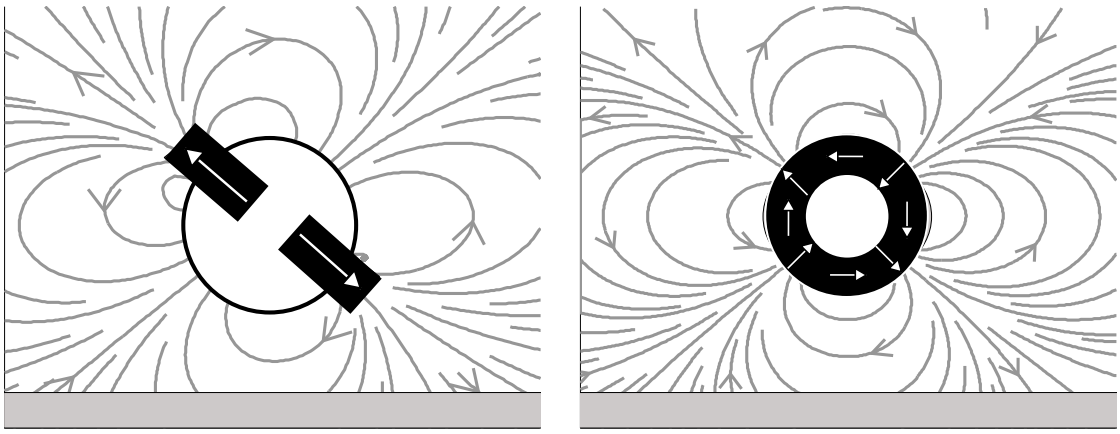

Figure 3.4: The two-magnet orthogonal array (left) generates a field similar to that of a two pole-pair Halbach array(right.) Each generates force by spinning about an axis out of the page.

dipoles orthogonal to the spin axis or a circular Halbach rotor (Fig. 3.4). An orthogonal array is less complex and easier to build, but the field of an equally sized Halbach rotor has a larger magnitude and is simpler to model[114]. For simplicity, preliminary experiments use a two-magnet orthogonal array that is well-approximated by a four-magnet Halbach rotor, but a high performance system would want to implement Halbach rotor induction couplers.

A spacecraft generating a time-varying magnetic field can produce forces in all three translational degrees of freedom and all three rotational degrees of freedom for complete six DOF actuation. Single induction couplers can only produce forces normal and tangential to their target, while systems of induction couplers can produce force in any direction relative to the target by taking advantage of a target's topography. Induction coupler systems can also generate torques: couplers situated away from the spacecraft's Center of Mass (CoM) on a moment arm can produce a coupled torque and force while two paired induction couplers separated by a moment arm can produce forceless torques. Thus, spacecraft using systems of induction couplers are not subject to the limitations of single induction couplers

in isolation.

The design for any system and mission using induction couplers needs to consider several parameters that govern their forces. These parameters include: the strong dependency on the gap to the target, the strength of the magnetic field, the properties of the target, and nonlinearities between the speed input and output force. The force magnitude decreases with g^{-4}, limiting an inspector's effective operating distance from its target. Larger magnets provide stronger fields that increase the force in exchange for more inertia and weight. The thickness and conductivity of the target scale the induced current and thereby the force. Finally, a system needs to consider that a coupler's input speed affects its force nonlinearly at high speeds. At low speeds this relationship is approximately linear (see Fig. 3.7) but increasing speed past a certain point shows diminishing returns because the penetration depth (or skin depth) of the induced current decreases at high frequencies.

Utilizing spinning magnetic fields on a spacecraft raises several valid but addressable concerns: changing magnetic fields could damage sensitive electronics or produce unwanted interactions with the earth's magnetic field, while mechanically spinning magnets can create problematic angular momentum. The skin effect[22] shields sensitive electronics from a coupler's eddy currents. Currents will only penetrate 0.1 mm into an aluminum-skinned target at 50 Hz - well below a coupler's operating limits. The coupler's relatively high frequency also prevents adverse interactions between the coupler's and the Earth's magnetic field. The earth's field is effectively static because the coupler frequency is far larger than the spacecraft's orbital period and each coupler cycle is closed, producing no net force between the two. The coupler's momentum could be absorbed by reaction wheels

or counteracted by counterspinning masses. Additionally, an induction coupler's bi-directional operating mode also helps counteract unwanted angular momentum because a coupler will switch direction frequently instead of spinning up like gyros. Ultimately, the coupler's angular momentum is a solvable design consideration.

3.2 Induction Coupler Experiments

Experiments on a low friction air track verify the simplified force model in equation 3.1. The experimental setup consists of an angled aluminum target plate mounted on a cart that moves along a low-friction air track. The cart is actuated by two induction couplers (Fig. 3.5) consisting of small commercial-off-the-shelf (COTS) motors (BaneBots MP-36004-540). Two arrays attach to the motors, each containing two neodymium magnets orthogonal to the spin axis. Table 3.1 shows the parameters used in the experiment.

During the experiment, the couplers accelerate the cart in both directions along the track to exercise the full range of eddy-current forces. The coupler's rotational speeds are manually controlled while a microcontroller records the rms voltage to the motors and a camera captures the cart's movement. `MATLAB` scripts extract the cart's position and acceleration over time, lining up the motor signals with the resulting movement.

The results in Fig. 3.6 demonstrate that the couplers can produce milliNewton shear forces parallel to a surface for less than one Watt. These forces agree with the model (Fig. 3.7), supporting its usefulness as a simulation tool. At 3.33 mN/Watt, the experimental specific force compares favorably to other non-contacting actuation technology (Table 3.2).

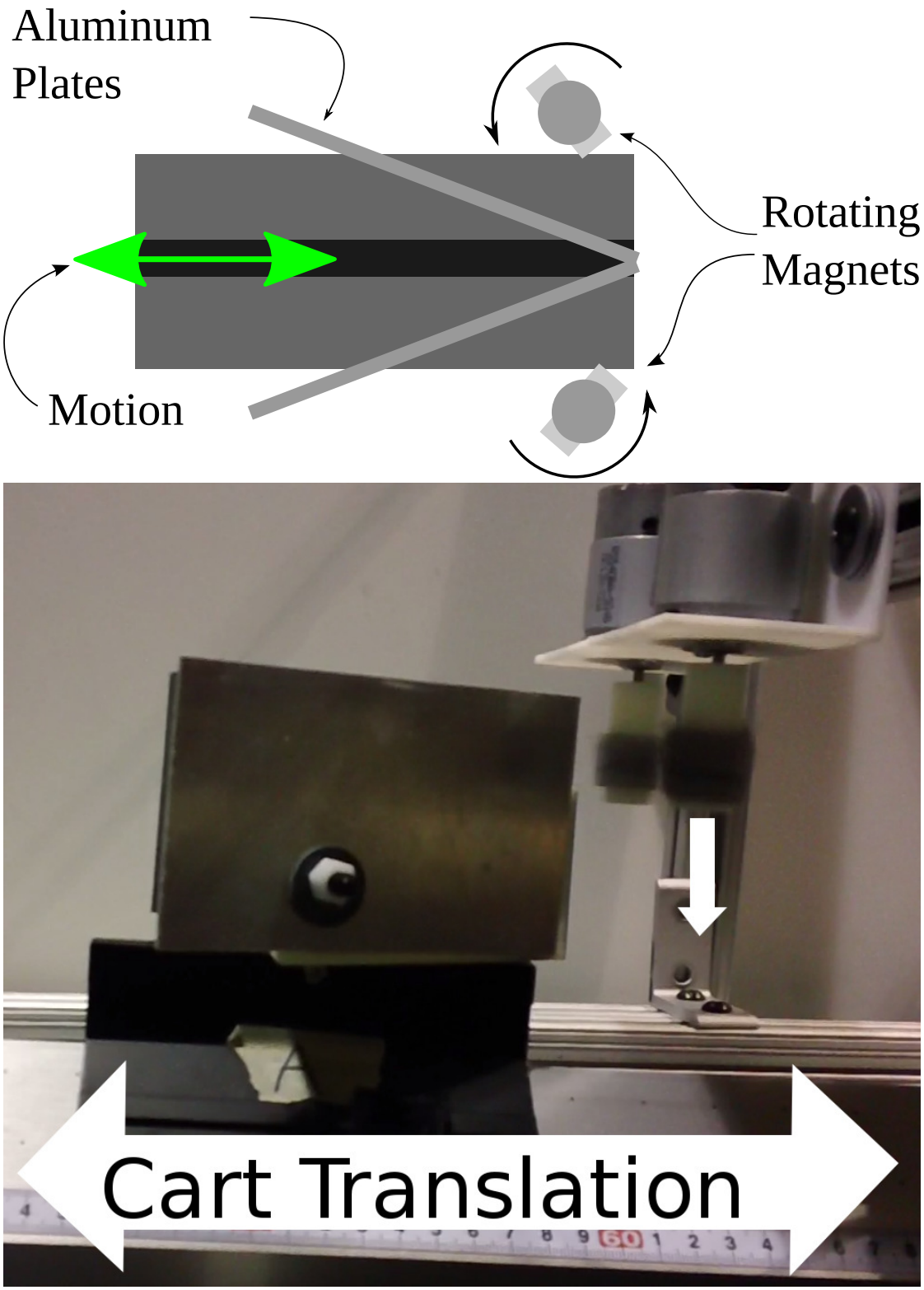

Figure 3.5: Top (left) and side (right) view of the experiments measuring induction coupler forces.

Table 3.1: Experiment Values

Variable	Value	Unit
Motor Voltage	12	V
Duty Cycle	25	%max
Motor Speed	4200	RPM
Motor Current	0.25	A
Motor Power	0.75	W

Table 3.2: Specific Force Comparison

System	Specific Force (mN/W)
Induction Couplers	3.33
Electromagnetic Dipoles	1.22 [46]
Coulomb Interactions	3×10^{-7} [44]

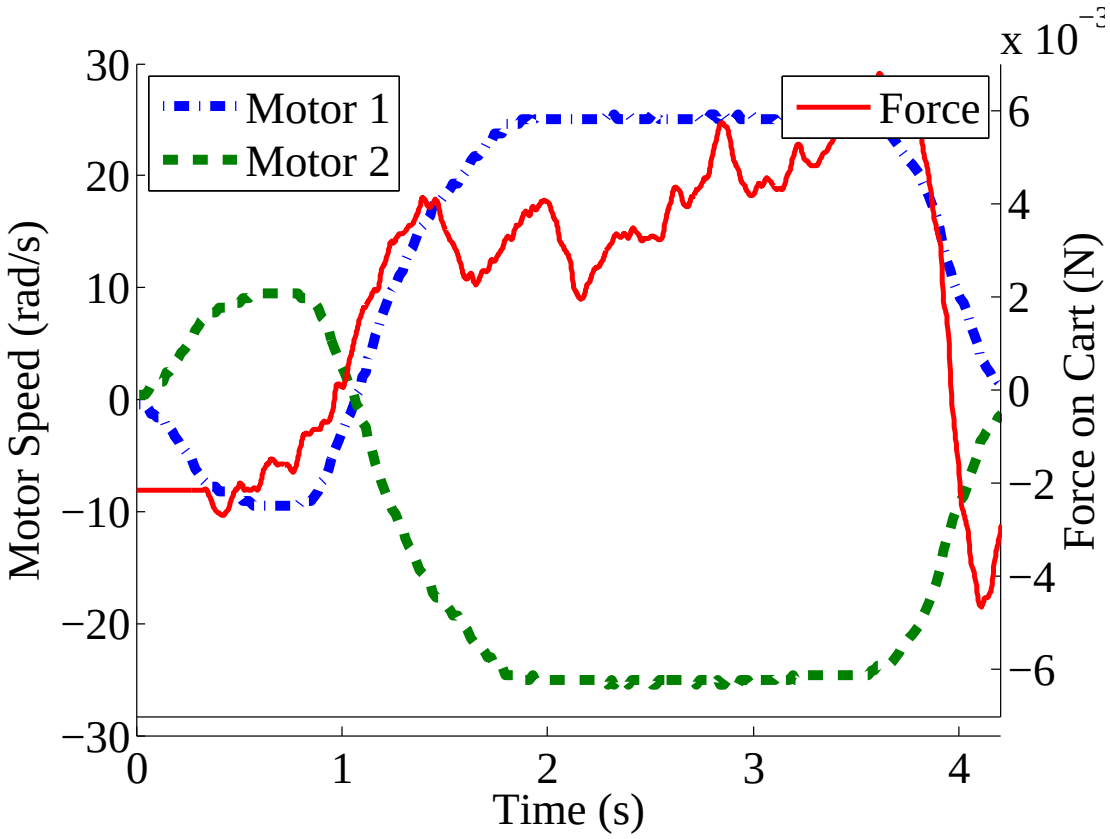

Figure 3.6: Force on a one-dimensional air-track levitated cart vs. motor speed.

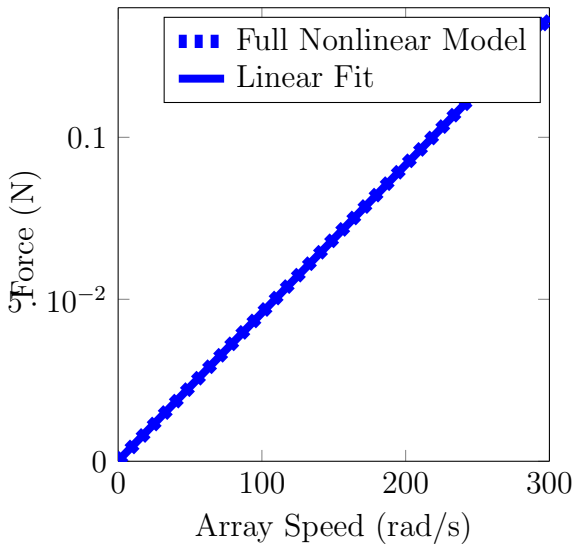

Figure 3.7: Linear fit between shear force and a magnet coupler's angular velocity.

3.3 Multi-Coupler System

An inspection spacecraft can use a system of several induction couplers to locomote near the surface of a target. The placement of these couplers affects the spacecraft's capabilities, driving further design considerations. This section addresses those considerations and simulates the operational capabilities of an inspection spacecraft navigating across the ISS. In a multi-coupler system, each coupler is the located on a vector $\boldsymbol{d}$ relative to the spacecraft's CoM and has a spin axis $\hat{\boldsymbol{a}}$ (Fig. 3.9). The force generated by each coupler varies linearly with with its angular speed, ω_i, when ω is small. The system kinematics are those of a standard 6 DoF rigid body.

$$\dot{R} = \omega^{\times} R \tag{3.2}$$

$$\begin{pmatrix} I\dot{\omega} \\ m\ddot{x} \end{pmatrix} = \begin{pmatrix} -\omega^{\times}(I\omega) \\ 0 \end{pmatrix} + \begin{bmatrix} 1 & 0 \\ 0 & R \end{bmatrix} Ju \tag{3.3}$$

where R is the direction-cosine matrix that relates coordinate systems for the target and inspector. ω is the inspector's angular velocity and x is its position,

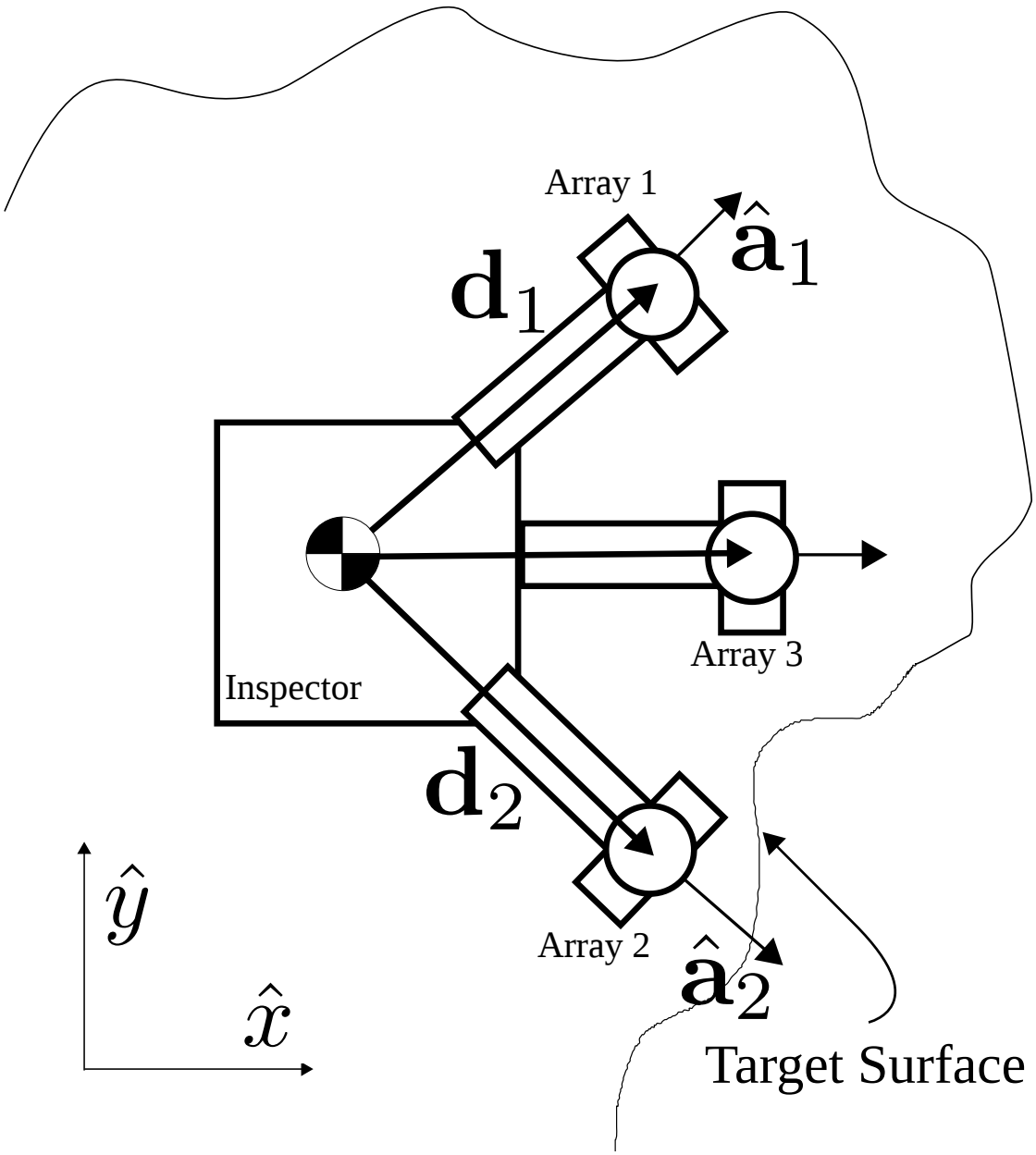

Figure 3.8: Top view of example induction coupler architecture.

both in the target's frame. I is the inspector's inertia tensor and m is its mass. The input Jacobian, J, transforms input speeds in the frame of each coupler,

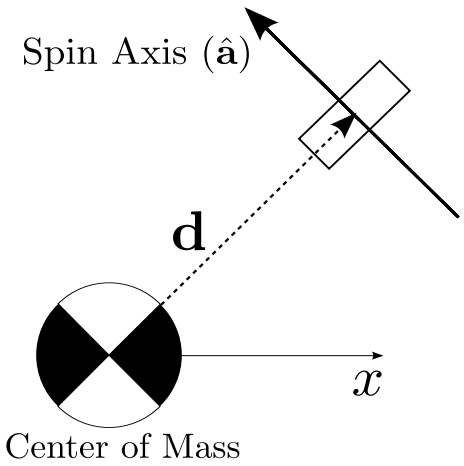

Figure 3.9: A single-magnet induction coupler.

$u = [\omega_1, \omega_2 ... \omega_N]^T$, to forces in the inertial frame.

$$J = C \begin{bmatrix} d_1^{\times} \left[(1-\beta_1)\, \hat{a}_1^{\times} \hat{n} + \beta_1 \hat{n} \right] & d_2^{\times} \left[(1-\beta_2)\, \hat{a}_2^{\times} \hat{n} + \beta_2 \hat{n} \right] & ... & d_N^{\times} \left[(1-\beta_N)\, \hat{a}_N^{\times} \hat{n} + \beta_N \hat{n} \right] \\ (1-\beta_1)\, \hat{a}_1^{\times} \hat{n} + \beta_1 \hat{n} & (1-\beta_2)\, \hat{a}_2^{\times} \hat{n} + \beta_2 \hat{n} & ... & (1-\beta_N)\, \hat{a}_N^{\times} \hat{n} + \beta_N \hat{n} \end{bmatrix} \tag{3.4}$$

The Jacobian in equation 3.4 imposes two design constraints:

- $\boldsymbol{d}_i \times \hat{\boldsymbol{a}}_i$ must be nonzero for at least one coupler so that the system can generate a control torque.
- Not all of the spin axes $\hat{\boldsymbol{a}}_i$ can be parallel. If they were, the Jacobian would not be full rank.

Three spinning arrays can govern three independent planar degrees of freedom. In practice, more should be used for redundancy and greater control authority. As long as the arrays have sufficient spatial separation their forces simply superimpose without the nonlinear coupling that might arise if one array's induced currents interact with another's magnetic field. A separation of 5.5 times the distance to the surface is enough to cause the magnetic field from one coupler to drop by an order of magnitude in the eddy-current region of the other. For a particular

application, these principles inform tradeoffs among force, power, mass, and the reliability of moving parts introduced by the additional arrays.

3.3.1 Simulation

A simulation of an inspection vehicle shown in Fig. 3.8 with parameters in table 3.3 demonstrates that a small spacecraft can successfully follow a trajectory and inspect a large area in a reasonable amount of time.

The example spacecraft uses three permanent magnet couplers to govern three independent planar degrees of freedom and traverse a path defined by several waypoints, where the inspector briefly pauses before moving on. Based on the experimental data in section 3.2, each coupler uses at most $0.75W$ for a maximum power consumption of $2.25\ W$ - within a cubesat's power budget[3]. The inspector's path is $3.4\ m$ long and includes 90 degrees of heading change to exhibit control in all three planar degrees of freedom.

Closed loop control is essential for induction coupler systems. Couplers are sensitive enough to their state that even numerical rounding errors in open-loop systems can throw the inspector off course. To compensate, the inspector uses a sequence of scheduled Linear Quadratic Regulator (LQR)[49] gains for feedback control between its desired state and the input speed to the induction couplers. As the inspector reaches each waypoint, it switches to the gains associated with the next waypoint.

Figs 3.10 and 3.11 show the simulation's waypoints, heading, and control input. Despite frequent pauses and turns, the inspector traverses the path at an average speed of $1\frac{m}{s}$. Extending these results, an inspector with a $0.1\ m$ inspection swath

could cover the 39 m^2 surface of the Destiny ISS module in just under two hours. The inspector's ability to stop itself cleanly at each waypoint means that this inspection could be executed in a lawnmower-like pattern, making the planning process simple.

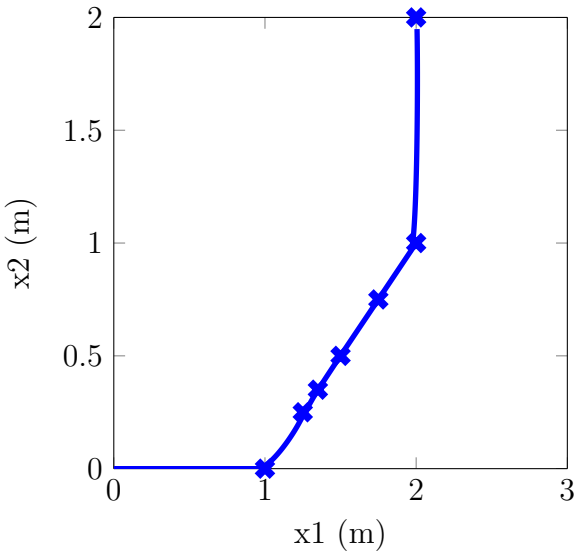

Figure 3.10: Trajectory of a simulated inspection vehicle with waypoints.

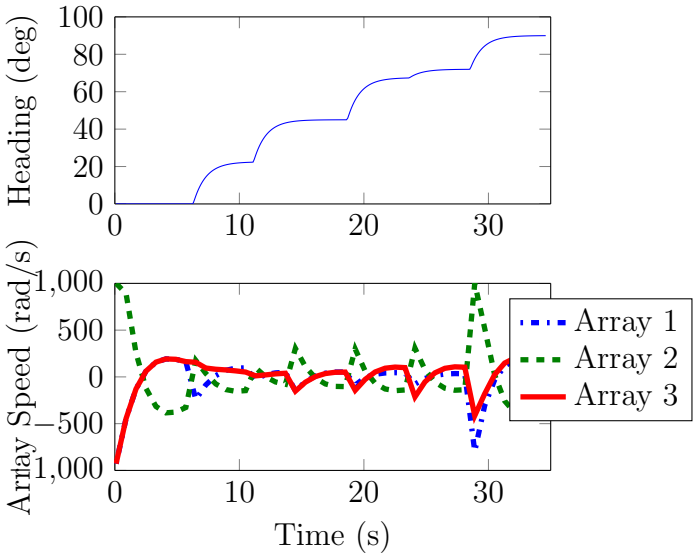

Figure 3.11: Heading and speed for a simulated inspection vehicle.

Table 3.3: Model Values

Variable	Value	Units
r_i	0.0127	m
r_o	0.0191	m
B_r	1.42	$N \cdot m^{-1} \cdot A^{-1}$
μ	1.08	
g	0.01	m
σ	3.53×10^5	$\frac{S}{m}$
b	0.01	m
m	4	kg
I	0.16	$kg \cdot m^2$

The simulation makes two assumptions: first, it ignores orbital effects that cause relative motion between the inspector and its target. Second, it assumes the inspector moves only in the plane parallel to the target with no out-of-plane motion. Section 3.4.1 expands on both assumptions.

3.4 Discussion

This section briefly discusses the limitations of induction couplers and directions for future developments.

3.4.1 Assumptions

Orbital disturbance forces and relative accelerations are significant concerns for any OOS application. A single induction coupler on a 4 kg spherical spacecraft of radius 0.1 m can generate a linear acceleration $a = 2 \times 10^{-3} \frac{m}{s^2}$ and an angular acceleration of $\alpha = 9 \times 10^{-3} \frac{rad}{s^2}$. These can easily compensate for perturbation forces in LEO [16][111].

Non-inertial accelerations are a consideration any time two spacecraft interact in orbit. The Clohessy-Wiltshire model[18] finds the linearized relative accelerations between the two spacecraft:

$$\begin{aligned} \ddot{x} &= 3n^2x + 2n\dot{y} \\ \ddot{y} &= -2n\dot{x} \\ \ddot{z} &= -n^2z \end{aligned} \tag{3.5}$$

$$n = \sqrt{\frac{\mu}{a^3}} \tag{3.6}$$

where x is along the line from the center of the earth to the target, z is along the target's angular momentum vector, and y completes the right-handed system, often pointing tangent to the target's orbit. In LEO, $\mu = 3.986 \times 10^{14}\ m^3 s^{-2}$ and $a = 4.15 \times 10^5\ m$, so $n = 1.13 \times 10^{-3}\ s^{-1}$. On a large structure like the ISS, x and z can be tens of meters. The ISS has a maximum dimension of $r = 54.3m$, creating maximum relative accelerations of $2.07 \times 10^{-4} m s^{-2}$. Even a single coupler can generate sufficient force to create accelerations an order of magnitude larger, warranting the simulation's assumption of an inertial target frame.

Out-of-plane forces created by induction couplers are another issue assumed away by the simulation. Induction coupler forces always have a component pointing directly away from the target surface. While small, this repulsive force will eventually drive the inspector away from the surface. There are three solutions to this problem: First, an induction coupler inspector can use topography of he surface to create attractive forces by placing couplers to either side of a curve or edge. This is a promising approach because there are few space structures that are completely flat over large scales (even solar panels have edges.) Second, a small thruster pointed directly away from the surface could apply forces towards the target as necessary. While a thruster would require propellant, an inspector using a

combination of thrusters and induction couplers would still get much more propellant economy than an all-thruster system and avoid plume impingement. Finally, an inspector could solve the repulsion problem by leveraging areas where orbital dynamics cause attractive acceleration between the inspector and the target, per equation 3.5.

3.4.2 Future Work

Induction coupler systems have many unexplored directions. The two most relevant to this chapter are dynamics augmented path planning and hardware improvement.

The relative accelerations between the inspector and the target could augment an inspector's capabilities. Specifically, future studies should explore planning paths using induction couplers to set initial conditions so that an inspector can traverse areas which would be inaccessible otherwise. Experimentally, future induction coupler implementations should use high-speed brushless motors to increase output forces.

3.5 Conclusion

This chapter presents a starting point for induction coupler technology. Preliminary experiments demonstrate specific forces of 3.33 $mN \cdot W^{-1}$ which are both larger and less power-hungry than other contactless actuators. Using these experimental values, a simulated mission shows that an inspection vehicle can use induction couplers to successfully traverse the ISS. Future work will focus on full six-degree-of-freedom maneuverability. These initial findings show that induction

couplers enable a unique ability for close-proximity inspection: inter-body force without mechanical contact, cooperation, or propellant.

CHAPTER 4

ACTIVE DETUMBLING WITH INDUCTION COUPLERS

Eddy-current forces are used as breaks on Earth, but can also stop spinning objects like out-of-control satellites in space. Specifically, permanent magnet induction couplers can form a three-axis damper that exhibits global Lyapunov stability. If the magnets are mounted on motors, the reaction torque applied on the magnets by the spinning target implies the angular velocity of the target. Spinning the magnets opposite the direction of the targets angular velocity produces a Lyapunov stable system that drives the angular velocity of the target to zero much faster than the damping from stationary magnets.

This chapter shows

1. Two static permanent magnets can create a Lyapunov-stable system with a spinning spacecraft.
2. Three orthogonal spinning magnets can sense the angular velocity of the target and provide appropriate damping toques.
3. Spinning permanent magnets get around the limits imposed by the speed of the angular velocity of the target on the ability of eddy currents to apply a damping torque.
4. A spinning-magnet actuator can always drive the angular velocity of the target to zero (Lyapunov stable.)

4.1 Lyapunov Stability of an EC Damped System

Even without active speed control, induction couplers can create a contactless system that is guaranteed to stably damp out a target's motion. Eddy-current forces provide an angular velocity damper on each axis as long as there are at least two orthogonal magnets. This follows from the fact that the only way a magnet produces no eddy-current toque on a nearby rotating body is if the axis of rotation is exactly aligned with the magnet's axis of symmetry. An arrangement of two orthogonal magnets guarantees that the angular velocity of a target can't align with the symmetry axes of all the magnets.

The target body has no potential energy and rotational kinetic energy makes up all of the body's kinetic energy.

$$E = T + V \tag{4.1}$$

$$V = 0 \tag{4.2}$$

$$T = \frac{1}{2}\boldsymbol{\omega} \cdot \mathbb{I} \cdot \boldsymbol{\omega} \tag{4.3}$$

The damping torque is proportional and opposite to the target's angular velocity.

$$\boldsymbol{\tau} = -c\boldsymbol{\omega} \tag{4.4}$$

The target's dynamics are simply Euler's equation of motion for a spinning body:

$$\mathbb{I} \cdot \dot{\boldsymbol{\omega}} + \boldsymbol{\omega} \times \mathbb{I} \cdot \boldsymbol{\omega} = \boldsymbol{\tau} \tag{4.5}$$

If there exists a Lyapunov function that is always less than or equal to the total energy of the system, it is zero when the state of the system is zero. If it has a derivative that is always negative, the system is stable in the sense of Lyapunov.

The total energy of the system is a Lyapunov function in the case of a spinning body damped by eddy-currents. From equation 4.3, $E = 0$ when $\boldsymbol{\omega} = 0$, meeting the first criterion of Lyapunov stability. To check the second condition of Lyapunov stability, find the sign of $\frac{dE}{dt}$:

$$\dot{E} = \dot{T} = \frac{^{N}d}{dt}\left(\frac{1}{2}\boldsymbol{\omega} \cdot \mathbb{I} \cdot \boldsymbol{\omega}\right) \tag{4.6}$$

$$\dot{T} = \frac{^{N}d}{dt}\left(\frac{1}{2}\boldsymbol{\omega}\right) \cdot \mathbb{I} \cdot \boldsymbol{\omega} + \left(\frac{1}{2}\boldsymbol{\omega}\right)\frac{^{N}d}{dt}\left(\mathbb{I} \cdot \boldsymbol{\omega}\right) \tag{4.7}$$

Note that the time derivative of the angular velocity in the body frame and the inertial spacecraft frame are the same because $\boldsymbol{\omega} \times \boldsymbol{\omega} = 0$.

$$\frac{^{N}d}{dt}\boldsymbol{\omega}^{\frac{B}{N}} = \frac{^{B}d}{dt}\boldsymbol{\omega} + \boldsymbol{\omega} \times \boldsymbol{\omega} = \dot{\boldsymbol{\omega}} \tag{4.8}$$

By definition $\boldsymbol{\tau} \equiv \frac{^{N}d}{dt}\left(\mathbb{I} \cdot \boldsymbol{\omega}\right)$ so the right-hand term of equation 4.6 becomes the LHS of equation 4.5

$$\dot{T} = \frac{1}{2}\dot{\boldsymbol{\omega}} \cdot \mathbb{I} \cdot \omega + \left(\frac{1}{2}\boldsymbol{\omega}\right) \cdot \left(\mathbb{I} \cdot \dot{\boldsymbol{\omega}} + \boldsymbol{\omega} \times \mathbb{I} \cdot \boldsymbol{\omega}\right) \tag{4.9}$$

Combining terms

$$\dot{T} = \boldsymbol{\omega} \cdot \left(\mathbb{I} \cdot \dot{\boldsymbol{\omega}} + \boldsymbol{\omega} \times \mathbb{I} \cdot \boldsymbol{\omega}\right) - \frac{1}{2}\boldsymbol{\omega} \cdot \boldsymbol{\omega} \times \mathbb{I} \cdot \boldsymbol{\omega} \tag{4.10}$$

But , $\boldsymbol{\omega} \cdot \boldsymbol{\omega} \times \mathbb{I} \cdot \boldsymbol{\omega} = 0$ so

$$\dot{T} = \boldsymbol{\omega} \cdot \left(\mathbb{I} \cdot \dot{\boldsymbol{\omega}} + \boldsymbol{\omega} \times \mathbb{I} \cdot \boldsymbol{\omega}\right) = \boldsymbol{\omega} \cdot \tau = \boldsymbol{\omega} \cdot \left(-c\boldsymbol{\omega}\right) \tag{4.11}$$

$$\dot{T} = -c\|\boldsymbol{\omega}\|^2 \tag{4.12}$$

Eddy-current dynamics dictate that $\forall c : c > 0$ and $\|\boldsymbol{\omega}\|^2 > 0$ when $\boldsymbol{\omega} \neq 0$. Thus, the system meets both conditions for Lyapunov stability. Recall from equations 4.1 and 4.2 that $E = 0$ when $\boldsymbol{\omega} = 0$ so the Lyapunov function is zero when the state is zero. Equation 4.12 shows that the derivative of the Lyapunov function is always negative when the system state is non-zero. As long as the spacecraft with the induction coupler can negate the absorbed energy through thrusters or reaction wheels

4.2 Feedback sensing of the target state

The induction coupler's damping effects can generate information about the target's rotational velocity. Sensing a target's spin rates is invaluable for planning collision-free maneuvers near a tumbling target. This analysis assumes that the magnet-wielding chaser spacecraft can know that it is an inertial frame, through star trackers, thrusters and gyros. If the permanent magnets are mounted on motors, the torque on the motor shaft when the magnets are held still always opposes the angular velocity of the target.

If the actuator consists of three magnets mounted on motors, the torque on the target is

$$\mathbf{F}_{net} \propto -\mathbf{v}^B\|\mathbf{B}\| \propto -\frac{m}{\|x\|^3}\left(\boldsymbol{\omega} \times \mathbf{r} - \boldsymbol{\omega}_m \times \mathbf{x}\right) \tag{4.13}$$

$$\boldsymbol{\tau} = \mathbf{r} \times \mathbf{F}_{net} \tag{4.14}$$

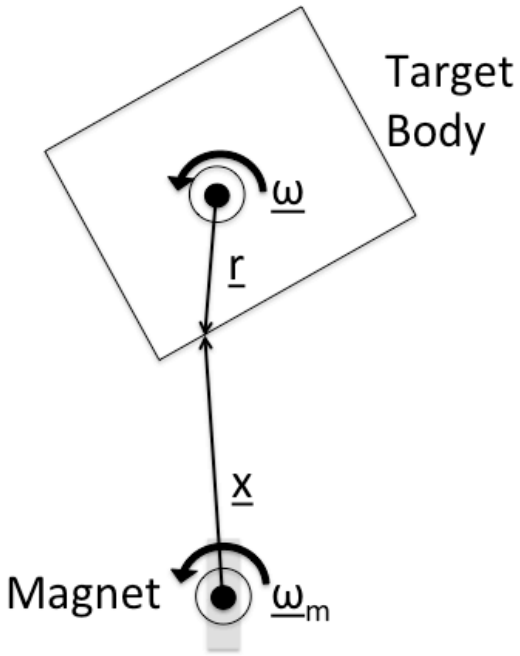

Figure 4.1: Diagram of target body and rotating magnet.

$$\boldsymbol{\tau} \propto -\mathbf{r} \times (\boldsymbol{\omega} \times \mathbf{r} - \boldsymbol{\omega}_m \times \mathbf{x}) \tag{4.15}$$

$$\boldsymbol{\tau} \propto -c\boldsymbol{\omega} + \mathbf{r} \times \boldsymbol{\omega}_m \times \mathbf{x} \tag{4.16}$$

The actuator spacecraft experiences equal and opposite torques from the target spacecraft. Thus, when $\boldsymbol{\omega}_m = 0$, the torques on the magnets imply the direction of the spin of the target. These torques act through the magnets and their motor shafts. Using that fact, the current needed to hold the magnets still in the presence of the external torques implies the direction and relative magnitude of the target angular velocity along each axis. Three magnets on linearly independent axes are necessary for this sensing technique to work because each motor can only sense torque along a single axis.

4.3 Spinning Magnets

Magnets mounted on motors are useful for more than just sensing the angular velocity of the target. Eddy-current forces generated by spinning (as opposed to static) permanent magnets can provide the same Lyapunov Stability as static magnets, but drive the angular velocity of the target to zero faster than static magnets. Spinning magnets remove the ceiling on the net torque imposed by the magnitude of the target bodys angular velocity (recall equation 4.4). Instead, the actuator spacecraft limits the maximum torque (equation 4.16.) These limits would come from the motor torque or the actuator spacecrafts ability to counter the reaction torque through reaction wheels or thrusters. The ability to provide torque independent of the angular velocity of the target prevents a situation where it takes near infinite time to actually bring the target to a stop.

4.4 Lyapunov Stability of Spinning Magnets

The torque produced by an array of spinning magnets generates a Lyapunov-stable system. This analysis continues to assume that the actuator spacecraft can sense the direction of the targets angular velocity as described in section 4.2. The equation for the energy of the target is the same as in equation 4.1 and is again be the Lyapunov function for the system. Following the analysis of section 4.1 and substituting the torque equation with spinning magnets from equation 4.16 into equation 4.8 gives:

$$\dot{T} = \boldsymbol{\omega} \cdot (-c\boldsymbol{\omega}) + \boldsymbol{\omega} \cdot (\mathbf{r} \times \boldsymbol{\omega}_m \times \mathbf{x}) \tag{4.17}$$

By picking $\boldsymbol{\omega}_m$ appropriately based on the direction of om,

$$\dot{T} = -c\|\boldsymbol{\omega}\|^2 - c_2\|\boldsymbol{\omega}\|\|\boldsymbol{\omega}_m\| \tag{4.18}$$

Thus meeting the criteria for Lyapunov stability, but with a Lyapunov function that converges on zero more quickly than the system with stationary magnets.

4.5 Conclusion

This chapter shows through a Lyapunov stability analysis that an array of magnets can always reduce the angular velocity of a target spacecraft to zero if the magnet frame (actuator spacecraft) remains inertial through thrusters and reaction wheels. These magnets can be either permanent or electromagnets, because the eddy-current forces only depend on relative motion between a target and a fixed set of magnets. However, it will take infinite time for the stationary magnets to bring the target to a complete stop. The same analysis shows that magnets mounted on spinning motors can de-spin the target more effectively. The spinning magnets can sense the rotation of the target through the external torque generated by the target when the magnet has no angular velocity. Based on this information, the magnet can then spin in the appropriate direction to slow the target.

CHAPTER 5

A LOW-COST TESTBED FOR MICROGRAVITY EXPERIMENTS

This chapter introduces a low-cost system for simulated microgravity experiments.

5.1 Test Bed Requirements

A low-friction test bed with a versatile closed-loop controller enables experiments that are essential for transforming induction couplers from a promising concept to a functional technology. This section outlines the capabilities that make the test bed system necessary for induction coupler development and the requirements on the system in order to provide these capabilities. An additional advantage of this test bed is its use of inexpensive off-the-shelf parts and software.

5.1.1 Justification for Test Bed Experiments

Experiments performed on a low-friction test-bed are integral to the development of induction couplers. The literature fails to address eddy-current forces that produce controlled actuation on a remote moving target. induction couplers operate in dynamic conditions that present numerical and analytical challenges for the simulation, analysis, and validation of eddy-current-based control without experiments. The equations governing the formation of currents by a changing magnetic field are essentially a vector form of the heat equation. A three-dimensional partial differential equation means that the forces produced by these interactions are impossible to find analytically except in a few constrained cases. Any useful actuator

would need to operate outside of these cases. Numerical models could find the forces, but there are problems with this approach as well. It is difficult for FEA to accurately incorporate both a non-steady-state external magnetic field and the dynamics of the target. Traditional FEA models are also specific to each actuator configuration. The overhead associated with setting up each FEA makes it hard to iterate quickly and build intuition about a new technology. Inevitably, these models must be simplified, but it is not yet clear which assumptions can even be made. The development of a working induction coupler needs validation of design choices and control systems beyond that is beyond the capabilities of numerical simulations.

Testing EC systems on a low-friction test bed has advantages over analytical and numerical models in several ways. Experimental characterization bypasses unmodeled effects that can be created by the many nonlinearities in the system. Experiments on a complete system will build valuable intuition for designing the prototype actuator. A physical demonstration of the capabilities of EC forces for actuation is far more compelling than models. Finally, the development of the test bed necessary for experimental characterization provides the capability to verify future models and test prototypes of both actuator hardware and control systems.

5.1.2 Minimum Requirements for Success

The test bed needs to meet a number of requirements. These requirements can be broken down into three broad categories:

1. Sensing Capabilities
2. Actuation Capabilities

3. Extensibility

Accurate system characterization and closed-loop control both require ability to measure the full state (acceleration, velocity, and position) of the target cart during an experiment. The need for accurate time-varying measurements of the targets state imposes a number a design constraints that are simple in concept, but non-trivial to implement. In order to capture the target's dynamics, the measurement frequency needs to be at least an order of magnitude larger than the dominant dynamics exhibited by the target under normal operating conditions. Additionally, the positional resolution needs to be fine enough to capture small position changes, because the system is only controllable over a small range. Finally, state measurements need to be consistently accurate over the course of an experiment. Hence, the system needs to compensate for sensor drift.

Quality measurements are not useful without the ability to produce controllable outputs and measure the state of the force-producing actuator. In order to create forces large enough to measurably affect the target, the actuator needs to produce at least two independent sinusoidal magnetic fields whose properties vary with time. The magnetic field is generated by the current through the electromagnet. As the control input ($\mathbf{u}$) to the system, the currents through the electromagnets should be both measurable and controllable (in a practical rather than formal sense.)

Another of the test bed's goals is to keep costs low while maximizing both the extensibility and reproducibility of the system. In order to achieve this flexibility, the components of the system should be easily replaced and upgraded to fit new experiments. The target cart should be able to accept targets of different sizes and materials, with the ability to hold them in different orientations so that the

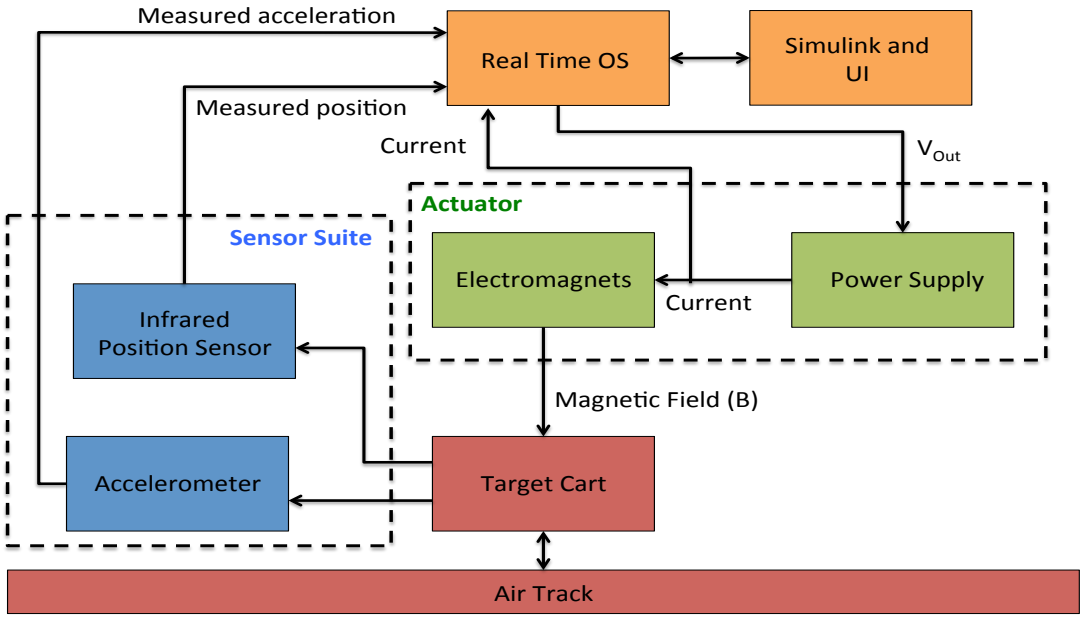

Figure 5.1: System architecture diagram illustrating the flow of information between components of the test bed. The track-cart subsystem is on the bottom, the sensor subsystem is on the left and the actuator subsystem is in the upper-right.

actuator can be validated in different scenarios. Additionally, reconfiguring the physical setup of hardware should be simple, as different experiments require different setups and the design of the prototype can change frequently based on new information.

5.2 System Architecture

The test bed consists of four subsystems (Fig. 5.1). The track-cart subsystem includes all of the moving parts and the air track that supports them. The sensor subsystem comprises the sensors that measure the physical state of the system. The actuator subsystem contains the electromagnets that generate the actuating magnetic field as well as the power supply. The sensor and actuator subsystems

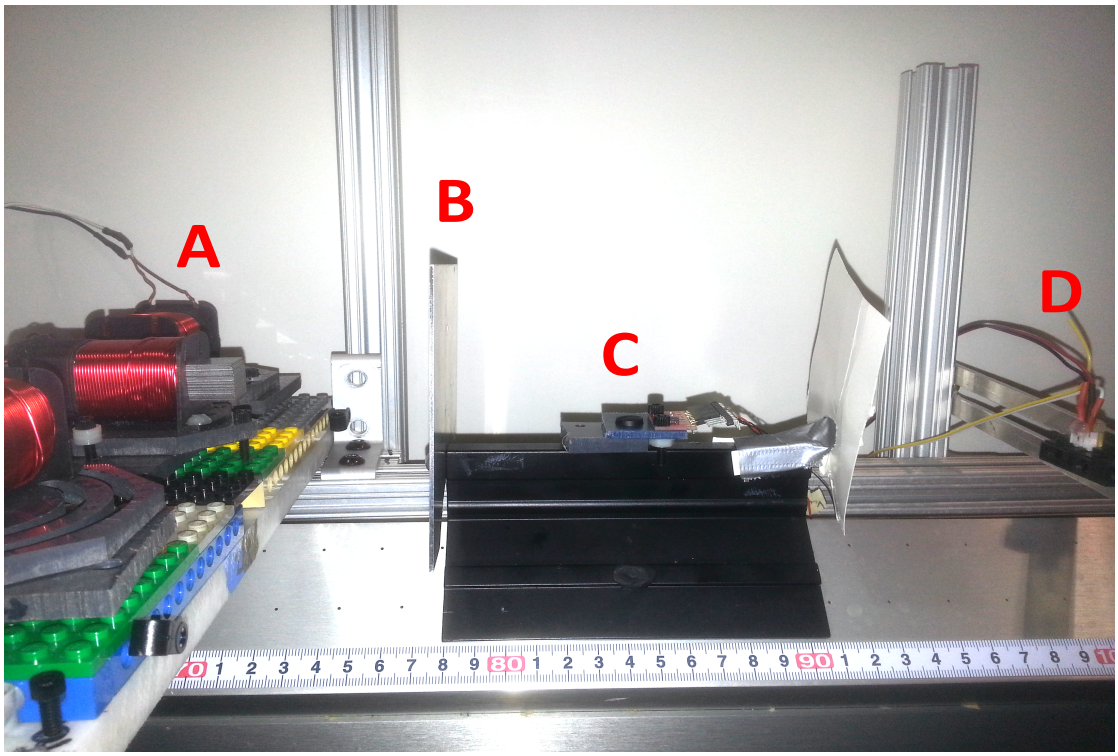

Figure 5.2: The test bed. Visible components: Actuation magnets (A); Cart (C) with accelerometer and conductive target (B); IR position sensor (D) on far right.

connect to the computer subsystem that serves as the "brain" of the entire system: recording data, estimating the state of the cart from the sensor inputs and closing the loop between the sensors and the actuator.

5.2.1 Track-Cart Subsystem

The track-cart subsystem is a heavily modified Pasco Scientific low-friction air track that is powered by a standard compressed air line. The track allows the target cart to exhibit low-friction dynamics similar to those found in a micro-gravity environment. The single DOF is beneficial because it simplifies the sensors necessary to measure the state of the system and simplifies the system for experiments that verify models or test parameter sensitivity.

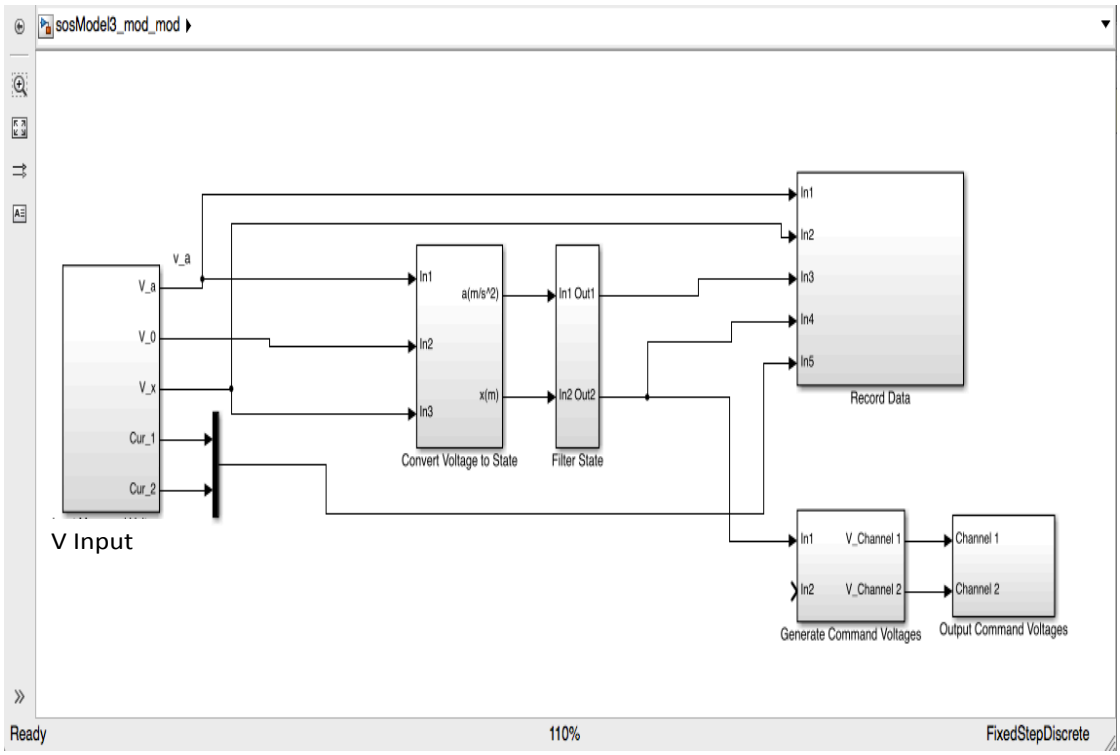

Figure 5.3: Simulink block diagram of control and data acquisition code running on the real- time OS.

Several modifications to the standard carts improve the extensibility of the system. Machined mounting points and modular mounting brackets enable the carts to accept any payload with the correct screw through-holes, making the carts able to accommodate future experiments that may have different payload requirements. The target mount is in front of the cart to ensure that the primary eddy-current interactions are between the actuator and the target, rather than the cart itself. Counterweights that are adjustable in directions both parallel and perpendicular to the axis of the cart prevent unbalanced loads from introducing friction into the system.

5.2.2 Computer

The core of the computer subsystem is a host computer running `Simulink` on Microsoft Windows and a target computer running the `Simulink xPC Target` real-time operating system. The real-time target handles analog to digital and digital to analog conversion (ADC and DAC) through a NI PCIe 6000 DAQ card. The real time target runs the Simulink diagram shown in figure 4 in a discrete loop with a 0.00025 second step size. This step size corresponds to a loop frequency of 4000 Hz, which exceeds the maximum frequency of the actuator (200 Hz) by more than an order of magnitude, allowing the system to capture and respond to all of the relevant dynamics. The loop first converts the voltage inputs to calibrated position and acceleration measurements. A Kalman filter implemented by the `Simulink DSP Toolbox` estimates the full state of the cart from the noisy sensor signals. A controller can then use the state estimate to inform the output voltage to the power supply and magnets.

5.2.3 Sensor Subsystem

The sensor subsystem comprises a Freescale Semiconductor MMA7361L accelerometer mounted to the cart and a Sharp GP2D120XJ00F IR position sensor. Due to its small size, the accelerometer can be mounted directly to the target cart without causing the payload to exceed specifications. However, the accelerometer cannot send its signal wirelessly because the necessary batteries and hardware would exceed the cart's weight payload. Extremely fine wire intended for medical applications provides power and data transfer while minimizing the effect on the cart's dynamics. Both sensors output analog voltage signals that are read by a NI

6861 PCIe DAQ card and converted from analog to a digital signal .

5.2.4 Actuator Subsystem

The actuator subsystem comprises three electromagnets and a two channel amplifier. The amplifier is a Carvin DCM 1500 audio amplifier. The amp accepts non-DC voltage signals on two channels and amplifies them, providing the currents pulled by the circuit up to current/voltage combinations, which exceed 1500 Watts between the two channels. The magnets are 15 mH laminate core speaker inductors. These parts are both off-the-shelf and designed to accommodate the large sinusoidal currents necessary to generate observable EC forces.

5.3 System Implementation and Assessment

The current implementation uses inexpensive, off-the-shelf components to sense the state of the system with greater precision than any of the components could achieve on their own. A real-time OS provides high frequency sensing, data collection, and analog outputs.

5.3.1 Part Selection

A large part of the design phase concentrated on part selection because there is no standardized way to instrument a low-friction test bed. Each one is usually custom made for a specific purpose. One of the goals of this project is to create a system that is replicable with easily available parts, instead of being at the

mercy of equipment specialized for other purposes. The goal of an easily replicable system is so that labs and schools can avoid a long generic design phase and focus on the specifics of their own low-friction experiments. This section presents the considerations informing the ultimate part selection.

Accelerometers have high bandwidth, but estimate position poorly. Conversely, position sensors have poor bandwidth, but are able to measure position directly. Computer filtering can compose multiple sensors, allowing them to supplement each other. The choice in accelerometer was not critical because MEMS devices have become both cheap and high quality. However, there are many choices for linear position sensors vision systems, optical encoders, laser sensors and infrared position sensors were all in consideration. These sensors all had a unique combination of price point, bandwidth, sensing range, sensing precision, and necessary computation. This test bed uses an IR position sensor because the sensor was inexpensive, precise, outputs easily convertible raw voltages rather than digital signals, and since the system doesn't require more than third of a meter sensing range the range of the sensor is not a downside.

There were several computing options available for reading analog voltage inputs, closing the loop, and producing analog voltage outputs. The three main possibilities were Labview, a microcontroller like an Arduino, and Simulink. The system required a high frequency control loop, which can only be achieved reliably with a microcontroller or a real-time operating system. Normal operating systems like Windows reserve the right to put threads on hold, so it is not guaranteed that outputs happen exactly when they need to. Arduinos can run a control loop at high frequencies, but are limited both in on-board computing power and the ability to record data. Labview works very well with all National Instruments products, but

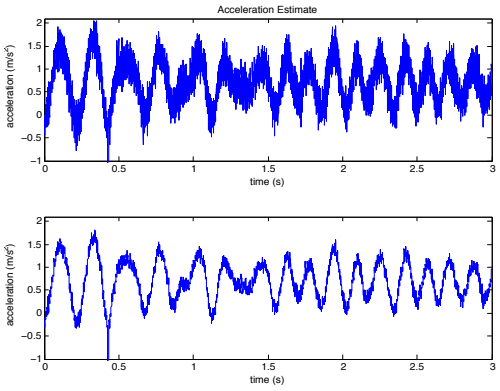

Figure 5.4: Acceleration estimate before (top) and after filtering (bottom.)

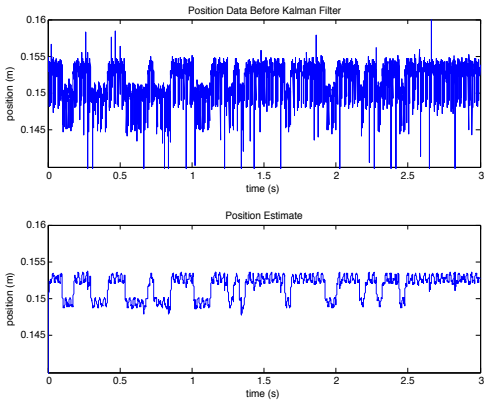

Figure 5.5: Position estimate before (top) and after filtering (bottom.)

did not have the easy customizability this system required. Ultimately, Simulink xPC target offered the most benefits and the least downsides.

5.3.2 Sensor Verification

The following graphs show test data demonstrating the capabilities of the senor suite. Using a Kalman filter to estimate the true state of the cart, the system can achieve sub-centimeter position precision for system dynamics slower than 20 Hz. While not ideal, this precision is sufficient for eddy-current actuator tests, which have demonstrated maximum forces of 0.05 N. These forces create system dynamics with a 5 Hz characteristic frequency under normal operating conditions: a 0.25 kg target cart and a 0.01 m minimum sensing precision. 5 Hz dynamics are sufficiently slow for the sensor suite to measure.

5.4 Discussion

In practice, the test system met all of the prescribed requirements and served as platform for several successful and unsuccessful (though still informative) experiments. The test bed provided the data in chapter 3 as well as preliminary tests for the experiments in 7 and several unsuccessful explorations into electromagnet-based induction couplers. The system does have several flaws as well. Leveling the track perfectly is impossible, and even then, tiny deviations in its height create potential wells that noticeably affect the cart's dynamics. On the sensor side, modern computer vision software has made high-end cameras extremely useful in controlled environments like laboratories as long as a project's budget can support them.

5.5 Conclusion

The quest to design any new spacecraft actuator eventually requires experimental verification. There are several low-friction test bed models available for experiments requiring simulated microgravity dynamics. However, both planar air bearing tables and rotational test beds have downsides. They introduce unwanted dynamics, have states that are hard to measure, and are expensive partially because they require specialized parts as well as consumables. These downsides and the technological gap in contactless orbital interactions motivated the design of a new low-friction test bed. This 1-D test bed has several advantages: it is easy to replicate because it is built from off-the-shelf components; it avoids as many extraneous dynamics as possible; and it is extensible thanks to input sensors, output actuators, and components that are easily modified and replaced. Novel spacecraft

construction will become less specialized and more widespread; the first satellite built by a high school recently achieved orbit. This trend will make simple, inexpensive test beds ever more important so that investigators can spend their time on the experiment itself rather than the experimental test bed.

5.6 Conclusion of Part One

Part I introduced induction couplers: a new technology for contactless spacecraft actuation. Chapter 2 outlines the implementation-independent properties shared by all induction couplers. It goes on to describe how a single coupler can take advantage of dynamics to pull on a target - an impossible task in a static situation. Chapters 3 and 4 explored two induction coupler applications: inspecting a large target and de-tumbling a target with unknown dynamics. Finally, chapter 5 explains the details of a simple, low-cost testbed for exploring induction coupler dynamics. Together, these results lay the groundwork for induction couplers to transform from proof-of-concept to a functional component of space-exploration infrastructure.

Part II

Complex Dynamical Systems: Design, Control, and Motion Primitives

CHAPTER 6

INTRODUCTION

Induction couplers offer a unique capability - contactless actuation with an uncooperative target. They also pose a unique set of challenges. Induction coupler systems are dynamic, high-dimensional, nonlinear, and control limited. These properties demand new methods for planning, control, and the system's design itself.

6.1 Motion Primitives

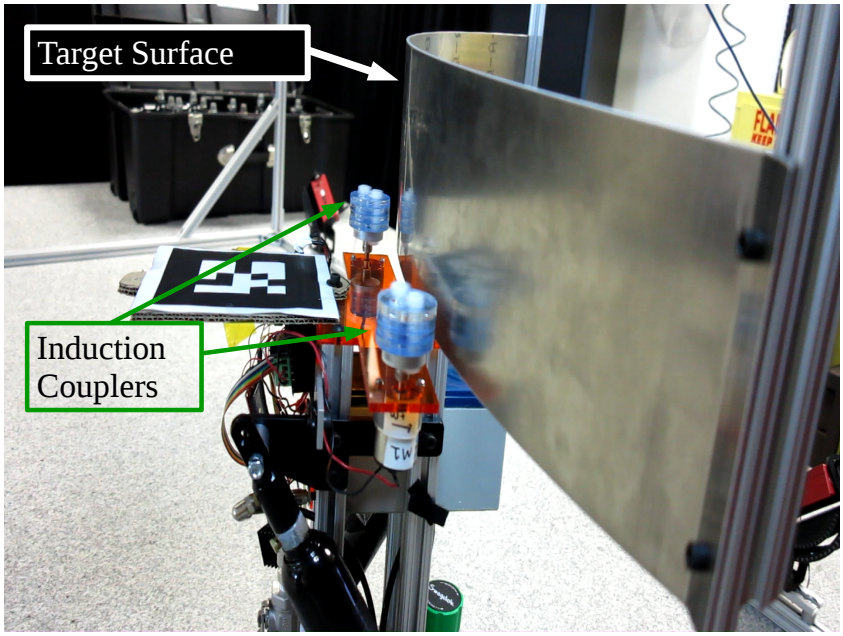

Figure 6.1: An experimental inspector on a low-friction testbed uses induction couplers to actuate off of an aluminum plate simulating the ISS exterior.

The goal of motion primitives is to build a library of maneuvers[25] that are the building blocks for global control strategies[79] and controller synthesis[82]. Hybrid trajectories composed of discrete transitions between continuous motion primitives have unlocked capabilities many nonlinear dynamical systems including humanoid

robots[35], dexterous arms [14] and helicopters [26] but this approach has not yet been tried in space systems. While probabilistic nature of motion planners have previously clashed with the need for strong guarantees in space operations, modern approaches can generate guarantees to address those concerns[10][29].

6.2 Control

Probabilistic methods like Rapidly-exploring Random Trees (RRTs) [51] are a common approach for attacking high dimensional systems. Several methods have demonstrated how RRTs can control systems with non-linear dynamics [78] and non-holonomic[42]. Probabilistic methods combine naturally with planning approaches that use local controllers to cover state space. These include sequential potential functions for navigation [20] and preimage backchaining, which uses sequential control 'funnels' to drive a system to a goal state [52, 57, 14].

The controller half of probabilistic co-generation is heavily influenced by LQR trees [105], which combine sequential stabilizing funnels with probabilistic methods and numerical verification [107]. Additionally, LQR trees provide coverage over all (reachable) state space by finding the regions of attraction for their control gains through SoS verification [88]. Our approach uses similarly verified coverage as information about the state space volume that a controller can drive to a stable goal state. Like LQR trees, our approach uses LQR control gains [49] in each individual controller. While simple, LQR gains can be quickly calculated and extended for control-limited systems [95].

RRTs in general and LQR trees in particular are single-query approaches - they drive the system to a single goal state. Single-query planners are good for a single

task or maneuver, but a system that may need to perform several different tasks needs a multi-query planner. There remain fewer analogs in dynamical systems for multi-query probabilistic planners like Probabilistic Road Maps (PRMs) [43, 61] than their single-query counterparts because many dynamical systems have only a few stable goal states. Thus, verification and controller generation for multi-query dynamical systems is an area of active research [55]. Following the lead of PRMs, our approach creates a safe roadmap through state space by connecting stable goal states with overlapping Region of Attractions (RoAs).

The plethora of possible goal states raise the question of how to evaluate the controller, because it can't be judged on driving the system to any single state. The number of states it can stabilize provides a different metric. Ideally, this metric would be the volume of the closed loop system's reachable set. Many systems can use the solution to the Hamilton-Jacobi-Bellman (HJB) equation to find their reachable set [61]. Other methods of verification include 'growing' reachable cells [21]. However, these methods are computationally intractable above three or four dimensions which makes them impractical even for dynamical systems that are unconstrained in three degrees of freedom.

Instead, our system needs an approximation for the full reachable set. One possible approximation is the volume covered by the RoAsof each set of control gains. Input-constrained systems without a clear metric for total energy defy traditional energy-based Lyapunov functions [45], so our method needs to generate Lyapunov functions by another path. Sum-of-Squares (SOS) programming leverages numerical optimization and increased computational power to algorithmically find a Lyapunov function for a system [73]. The function's level sets define a RoA in state space where the controller can always stabilize the system. These RoA

are often small in strongly nonlinear systems because a single LQR controller is based on a linearization of the system. One downside of SOS programming is that it is computationally intensive and scales poorly to high dimensional systems. However, recent research has shown that Diagonally-dominant SOS (DSOS) programming and Scaled-Diagonally-dominant SOS (SDSOS) programming are viable alternatives to SOS programming in high dimensions [1].

6.3 Algorithmic Design

Many systems are full of numerical design parameters that dominate their dynamics. These parameters can be anything from the wing width of an airplane to the volume of a chemical tank to the length of a pendulum or the number of joints in an arm. The resulting dynamic effects are then unavoidably linked to the system's control law. A naive set of parameters can render the system effectively useless. Ideally, the system's parameters would take its future controller into account to maximize its whole performance.

System design can be long and involved, so ideally it would leverage increased computing power to expedite the process and unlock the power of complex systems. Traditional methods for designing simple systems close the loop between the parameters and controller through a combination of intuition, analysis/tuning, and leveraging well-studied systems. This process tends to fall apart as the system becomes more novel or complex - a perfect place for more algorithmic approaches to step in [117]. As additive manufacturing, laser cutters, and cheap, multi-use electronics make new and on-the-fly system creation more common, design techniques need to match these advances [31].

Note that many systems don't need algorithmic design synthesis. Often, the design of a physical system is determined by external factors - manufacturing costs and well-understood designs are important considerations. A novel system is often intuitive or well understood; it may have a few free parameters which have well-known effects on performance [37]. However, even in these cases algorithmic system generation enables a symbiotic pairing between humans and machines - leaving the humans to do the creative work they are best at, while the computer takes care of the details.

Different fields have used algorithmic co-generation to design parameters and controllers across several applications. Chemical engineering uses several tools to simultaneously generate designs and control laws for large-scale systems [47, 91, 90, 9]. Aerospace engineers have applied co-generation to the designs of flexible spacecraft [33, 84, 98] and micro air vehicles before they were drones [40]. The co-generation methods used in aerospace and chemical engineering take a purely optimization-based approach, which can provide explicit performance guarantees. These guarantees are needed because the systems in question are often delicate and expensive.

Algorithmic co-generation can be especially useful in robotics, where systems need to adapt to many situations [84] and may be reconfigurable [48] or designed on the fly [118]. Robotic co-generation uses either optimization over the parameterized dynamics or genetic algorithms paired with simulations [4, 36].

Each of these systems has trade-offs. Optimization-based methods perform well in several cases: when the dynamics can be expressed analytically [83] or when the dynamics are smooth, low dimensional or linear. If a system doesn't meet these conditions, the optimization could fail to converge or require excessive

tuning (essentially reverting to hand-design.) Simulation-based co-generation can handle systems that defy traditional optimization. However, whereas simulations can demonstrate functionality, they give no guarantees. Additionally, both optimization and simulation-based methods primarily target systems with a single goal - whether it be a point in state space or a limit cycle.

6.4 Contributions

Part two comprises three primary contributions:

1. The four motion primitives an induction-coupled inspector can use to navigate the surface of a target - chapter 7.
2. Experimental demonstration of induction coupler motion primitives - chapter 7.
3. A new algorithm for simultaneously generating the design and controller for complex dynamical systems - chapter 8.

CHAPTER 7

MOTION PRIMITIVES FOR AN INDUCTION-COUPLED INSPECTOR

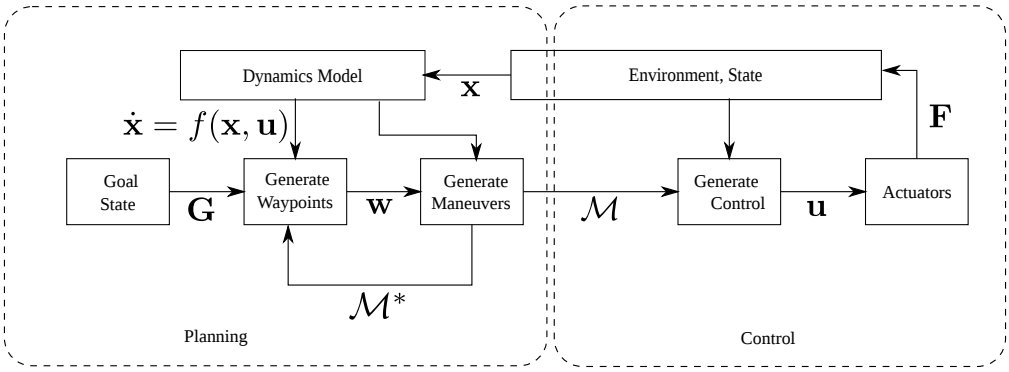

Figure 7.1: Induction Coupler System Diagram.

The first step towards an induction coupler locomotion system is to model the system and break the problem into motion primitives for each DOF. What is an induction coupled inspector capable of given different states? This is a difficult question because eddy-current forces depend both on the robot's pose and the geometry of the environment.

This chapter provides three contributions to planning and control using induction-coupler actuation, focusing on waypoint generation, control generation, and actuator modeling (figure 7.1). It first builds a dynamics model by extending 2D force model to find the force generated by arbitrary configurations of multiple induction couplers. The model leads to four basic control inputs and their associated motion primitives that can be combined to create six degree-of-freedom actuation: planar force (force in the plane of the target), planar torque (torque about an axis out of the plane), out-of-plane force, and out-of-plane torque. Simulations and experiments illustrate that each of these motions requires a different configuration of couplers and control input from those couplers. Finally, a multi-

movement trajectory shows how the primitives can be composed to create 6-DOF movements and motivates several requirements on induction coupler systems.

Section 7.1 presents an analytical model to solve for induction-coupler force. Section 7.2 describes and simulates the open-loop behaviors that cause motion in each DoF. Section 7.4 presents experimental verification of each motion with a prototype induction coupler system on a low-friction testbed, shown in figure 6.1. Section 7.5 addresses general considerations for multi-movement trajectories and simulates a full trajectory. Finally, section 7.6 discusses the implications for induction inspector design, control, and implementation.

7.1 Actuator Model

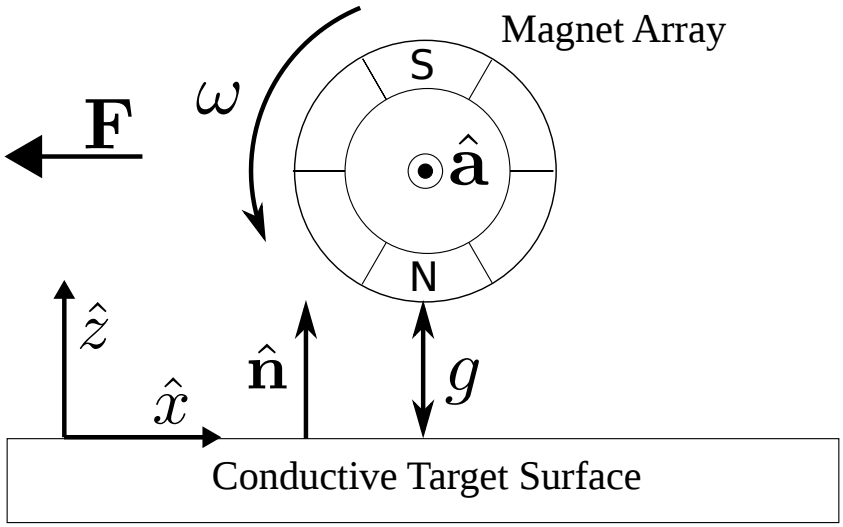

Figure 7.2: Diagram of a single induction coupler array

Maxwell showed that a time-varying magnetic field induces an electric current in nearby conductors. Magnetic fields generate a force on moving currents. These

two effects combine to create an eddy-current force between a source of a changing magnetic field and a conductive surface. Induction couplers can use mechanically moving permanent magnets or time-varying electromagnets to generate a time-varying magnetic field. This chapter focuses on the simplest and least power-intensive implementation of a mechanical induction coupler: a motorized, circular array of magnets.

Paudel and Bird derived an analytical solution for the force from a single rotating array of permanent magnets near a flat conductor. [75] In a Newtonian reference frame (S) fixed to the conductive surface as shown in figure 7.2, the force on the magnet array is

$$ {}^{S}\mathbf{F} = \frac{w}{8\pi\mu_0} \int_{-\infty}^{\infty} \Gamma(\xi, g) |B^s(\xi, g)|^2 d\xi \tag{7.1} $$

where Γ is a transmission function associated with the conductive surface and B is the spatial Fourier transform of the time-invariant part of the array's magnetic field. Γ and B are nonlinear functions of the system state. Γ depends on the array's angular rate ω, velocity $\mathbf{v}$ and distance from the surface g. B is a nonlinear function of g as well. Near a curved surface of the scale of typical spacecraft, the assumption of an infinite flat surface is *locally* valid for induction couplers because the operating gap is on the order of centimeters: very small compared to the curvatures of most target surfaces.

Eddy-current properties and geometry can extend these forces from constrained, single wheel models to dynamic models of a 6-DOF orbital inspector. This extension is important because the coupler's axis is rarely perpendicular to the surface normal, and it is much more convenient to represent the forces in a global coordinate system instead of one fixed to the target surface. Eddy-current

forces act only in opposition to change in magnetic field. So, the net force always acts in a direction perpendicular to the array's spin axis. Thus, a 3D formulation of the force in any reference frame can be found by tilting the force plane (shown in figure 7.2 along with $\hat{a}$.)

$$\begin{aligned}\mathbf{F} =& F_z(g,\omega,\mathbf{v})\,(\hat{\mathbf{a}}\times\hat{\mathbf{n}}) \\ &+F_y(g,\omega,\mathbf{v})\,(\hat{\mathbf{a}}\times\hat{\mathbf{n}})\times\hat{\mathbf{a}}\end{aligned} \tag{7.2}$$

F_z and F_y are the components of the planar force calculated in equation 7.1.

This statement of eddy-current forces is powerful because it is both analytical and general. The generality enables fast simulations of a 6-DOF inspection vehicle while the analytical nature enables provable statements about the system's stability. A full system consists of several couplers to control all six DOFs. Each[M2] coupler rotates around an axis, $\hat{\mathbf{a}_n}$, located at $\mathbf{d}_n$, shown in figure 7.3. The net control force is

$$\mathbf{F}_{net} = \sum_i F_z\,(\hat{\mathbf{a}}_i\times\hat{\mathbf{n}}_i) + F_y\,(\hat{\mathbf{a}}_i\times\hat{\mathbf{n}}_i)\times\hat{\mathbf{a}}_i \tag{7.3}$$

and the net control torque is

$$\boldsymbol{\tau}_{net} = \sum_i \mathbf{d}_i\times[F_z\,(\hat{\mathbf{a}}_i\times\hat{\mathbf{n}}_i) + F_y\,(\hat{\mathbf{a}}_i\times\hat{\mathbf{n}}_i)\times\hat{\mathbf{a}}_i] \tag{7.4}$$

$\mathbf{n}_i$ is the vector to the surface segment closest to array i.

The following sections use this model to demonstrate how a robotic inspector can use induction couplers to generate force and torque in all six rigid body DOFs.

7.2 Movement Primitives

7.2.1 Planar Movement

While moving in the plane parallel to the target surface, induction couplers resemble contactless wheels, but they generate force parallel to the surface that increases with their speed. Thus, a fixed arrangement needs at least two couplers to move in all three planar DOFs and three couplers to control each DOF independently.

Unlike wheels, induction couplers do not provide significant constraint force perpendicular to their rotation. Wheels skid if they accelerate too quickly, whereas induction coupler accelerations are limited only by the capabilities of their motors.

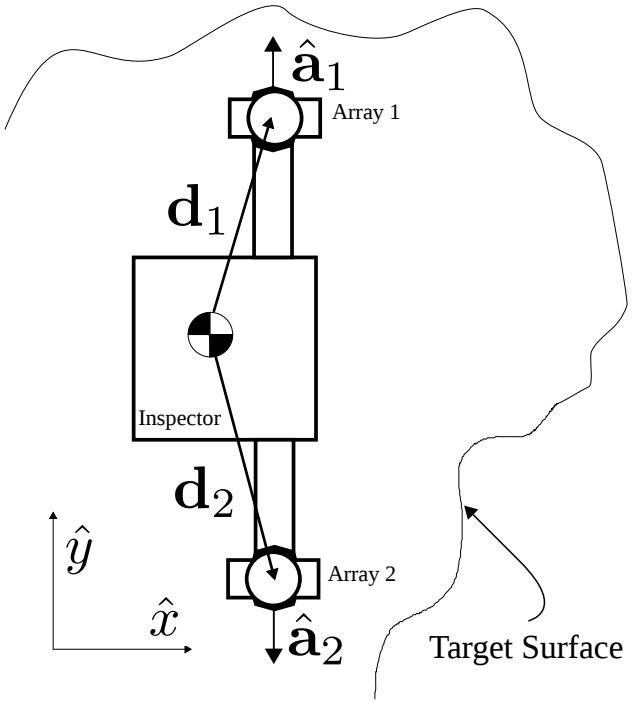

Figure 7.3: Configuration for planar control: An inspector with two arrays spinning about $\hat{\mathbf{y}}$ can translate and rotate above a flat target surface

An inspector can translate in the plane by using a pair of induction couplers like

differential drive wheels. Figure 7.3 shows this mode. Ideally, pure translational motion will involve no net torque. Applying these forces along a line of action that does not pass through the system's CoM naturally produces a torque. Without no-slip constraints, force and torque are coupled. Thus, the system is extremely sensitive to modeling error and implementing induction couplers for locomotion generally requires active control of all rigid-body DOFs.

An inspector also needs to rotate in the plane parallel to the surface. The simplest way for induction couplers to produce rotation about an axis normal to the surface without translation is similar to differential drive wheels, with two couplers spinning in opposite directions on axes parallel to the surface. Like pure translation, pure rotation in a real system is sensitive to the relative geometry of the coupler, the surface, and the CoMlocation, again demanding feedback control to decouple angular from translational motion.

7.2.2 Out-of-Plane Movement

It is more complicated for induction couplers to produce force and torque that control movement out of the plane parallel to the target surface because the forces from a single induction coupler are limited in their direction.

The force generated by spinning magnets is almost completely tangential to the surface. For large ω, the ratio of the normal to tangential components of the force increases slightly and can be used to repel away from the surface. However, these forces are small and act only in the $+\hat{\mathbf{z}}$ direction, giving no control in $-\hat{\mathbf{z}}$. By strategically summing forces across several couplers near different locations on a *non-flat* surface, the inspector can generate larger net forces in both $+\hat{\mathbf{z}}$ and $-\hat{\mathbf{z}}$.

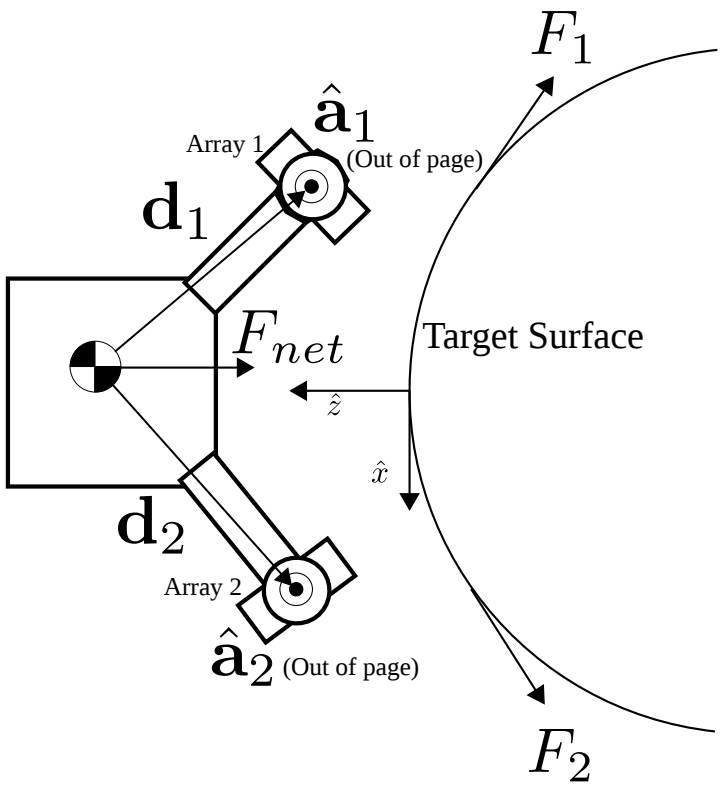

Figure 7.4: Configuration for out-of-plane control

Rotating two couplers oriented along the $\hat{\mathbf{y}}$ with opposing ω creates a force at each coupler whose $\hat{\mathbf{x}}$ components cancel and whose $\hat{\mathbf{z}}$ components sum, pulling the inspector towards the surface or pushing it away. This strategy is illustrated in figure 7.4.

Using tangential forces at each coupler, the inspector can control rotation about the $\hat{\mathbf{y}}$ axis by giving each coupler the same input speed ω. With only two couplers, force always couples with torque. A three-coupler array would allow the force and torque to be applied independently.

7.3 Simulation

In this section, simulations demonstrate each motion primitive: planar translation, planar rotation, out-of-plane translation, and out-of-plane rotation. In each case, the simulation constrains the inspector to the plane of interest to demonstrate open-loop motion primitives and match experimental constraints. In practice, a closed loop controller and more than two couplers are essential to enable motion out of the plane. The model considers an inspector that is the size of a micro- or nano-satellite, using two motors each with two magnets as induction couplers. The simulation parameters shown in table 7.1 match the experimental demonstrations in section 7.4.

Table 7.1: Simulation Parameters

Description	value	units
Max Coupler Speed, ω	32.7	rad s^{-}1
Max Coupler Power, P_{max}	2	W
Max Magnet Shear Speed, v	0.98	$\frac{m}{s}$
Magnet Surface Field, B	4667	Gauss
Mass m	10.2	kg
Inertia $\mathbb{J}$	$1.02 \cdot \mathbb{I}$	kgm^2
Gap in Planar Movement g	1	cm
Conductivity, σ	2.5 $\times 10^7$	Sm^{-1}
Curvature of non-flat target, κ	0.14	m^{-1}

7.3.1 Planar Movement

To demonstrate planar movement, the target is represented by a flat conducting plate in the x-y plane shown in figure 7.3.

In a simulation of planar translation the inspector first drives itself forward by

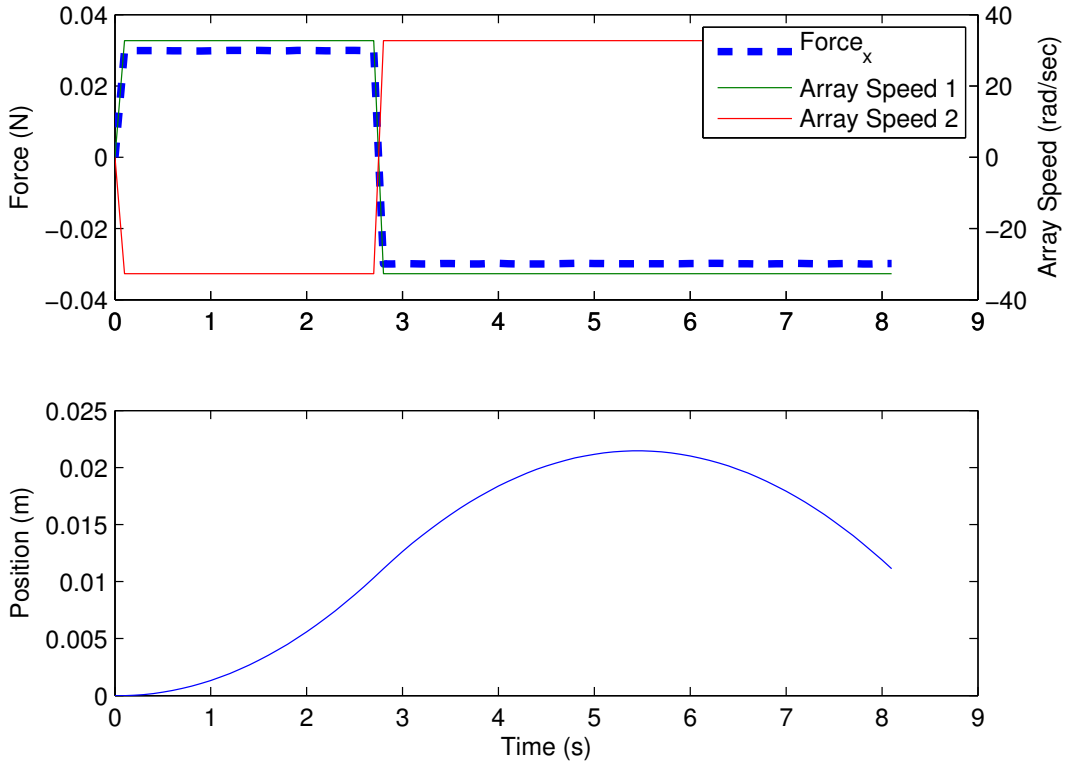

Figure 7.5: Simulation of planar translation. The top plot shows the speed inputs to the couplers and resulting control force. The bottom plot shows the inspector's position

commanding opposite speeds in each coupler. Because $\hat{\mathbf{a}}_1 = -\hat{\mathbf{a}}_2$, opposite speeds in the couplers result in both spinning in the same direction. The speeds of both couplers then reverse direction, creating a negative force and moving the inspector backwards. Figure 7.5 shows the coupler speeds, force, and displacement.

In a simulation of planar rotation the inspector commands the same speed to each coupler, rotating itself about the positive z axis. The speeds of both couplers then reverse direction, generating a torque about the negative z axis. Figure 7.6 shows the coupler speeds, torque, and heading.

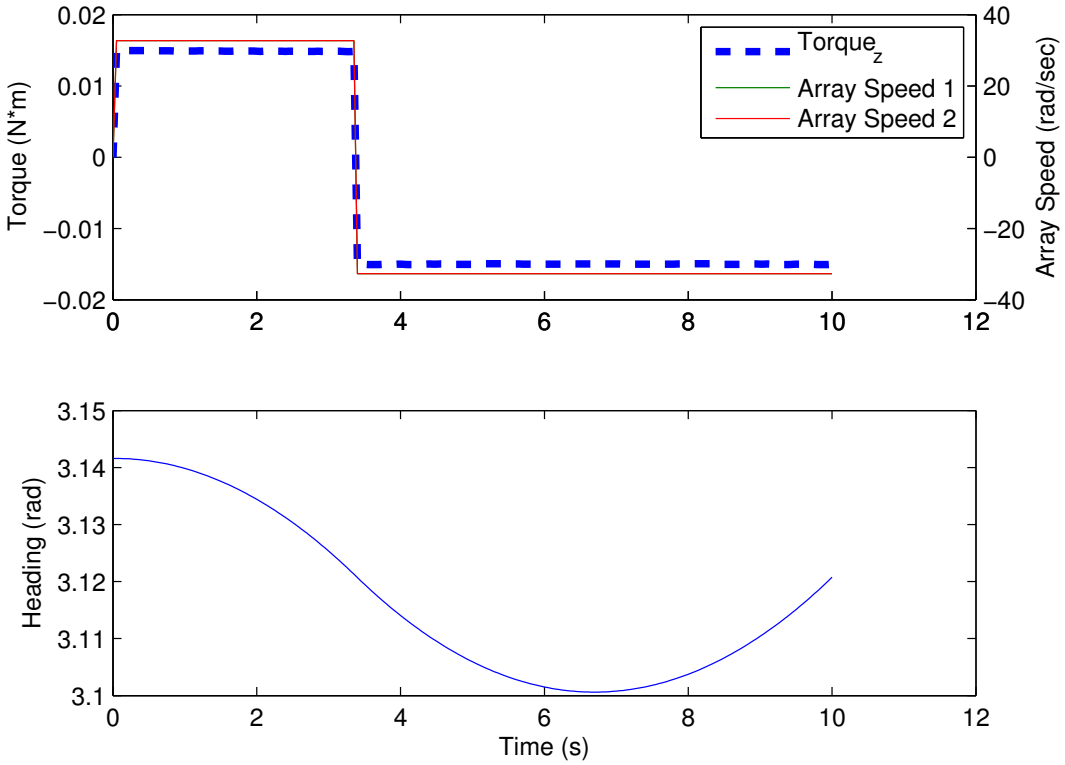

Figure 7.6: Simulation of planar rotation. The top plot shows the speed inputs to the couplers and resulting control torque. The bottom plot shows the inspector's heading. Note: the control speed is the same for both arrays

7.3.2 Out-of-Plane Movement

To demonstrate out-of-plane movement, the target is a curved surface in the x-z plane, shown in figure 7.4. The surface curvature matches an ISS module both in simulation and experiment to approximate real capabilities as much as possible. The induction couplers both spin about the y axis in the body frame so that they can produce motion in the x-z plane by generating force tangential to the surface.

In figure 7.7 the inspector pulls itself towards the surface by spinning with opposing speeds so that the z component of each tangential force is negative. When the forces from each coupler sum, the resultant force is entirely in the $-z$

direction, pulling the inspector towards the surface. The inspector then reverses the coupler speeds, pushing itself away from the surface and preventing a collision. Finally, it stops itself at its original position.

In figure 7.8 the inspector rotates about the y axis by spinning each coupler in the same direction.

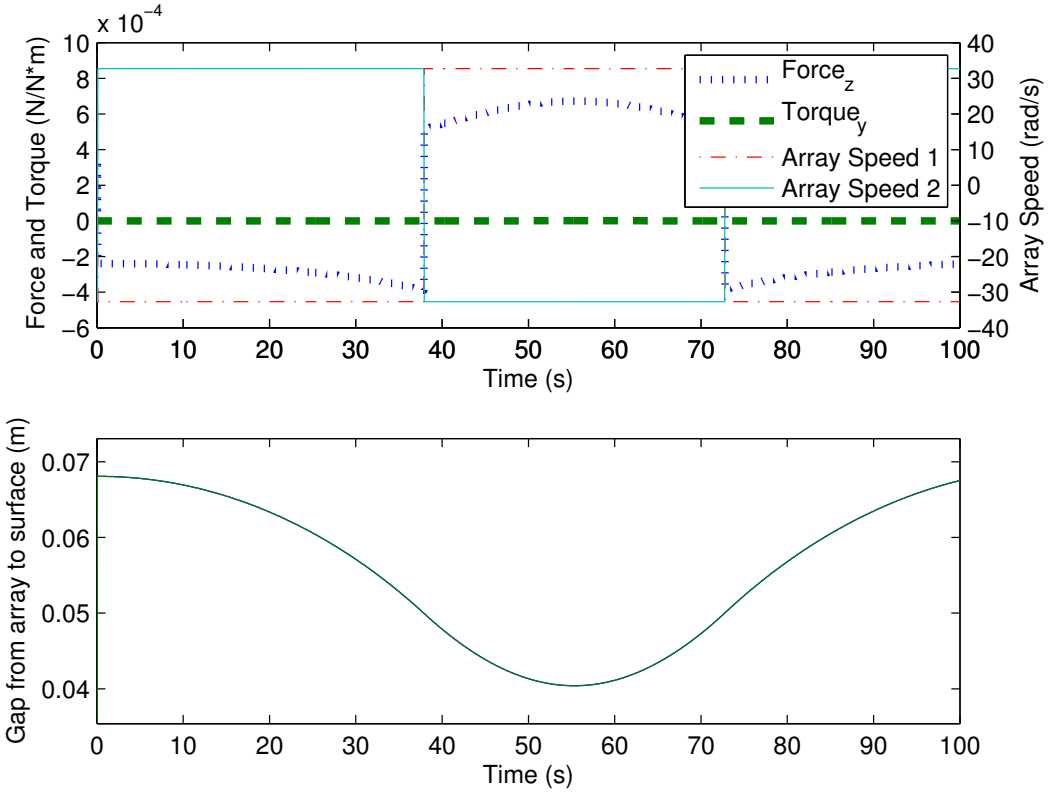

Figure 7.7: Simulation of out-of-plane translation. The top figure shows the input speeds for each coupler and the resultant force on the inspector. The bottom figure shows how the gap between each coupler and the surface change in response to the control force

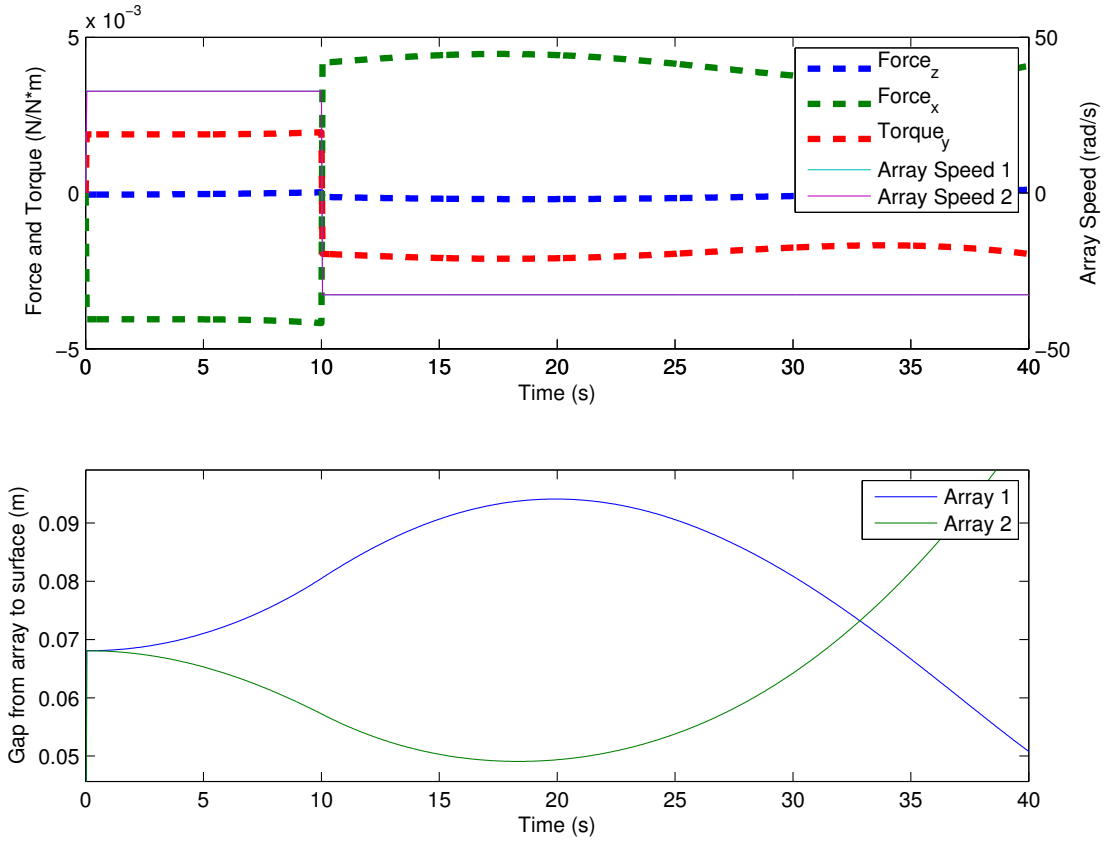

Figure 7.8: Simulation of out-of-plane rotation. The top figure shows the input speeds for each coupler and the resultant force and torque on the inspector. The bottom figure shows how the gap between each coupler and the surface change in response to the control force and torque

7.4 Experimental Demonstration

This section discusses an experimental demonstration of each motion primitive: planar translation, planar rotation, out-of-plane translation, and out-of-plane rotation–in an ideal situation. The demonstration consists of two prototype inspection vehicles, each with two spinning magnet arrays. One prototype, pictured in figure 7.9, demonstrates the planar movement suggested in figure 7.3. The other prototype, pictured in figure 6.1, demonstrates the out-of-plane movement shown in figure 7.4. These inspection vehicle analogues operate on a low-friction air-bearing test bed, which allowed them to simulate a space-like environment with

three DOFs.

The analogues operate close to, but not touching, an aluminum sheet-metal target during the experiments. During planar movement, a flat target sits above an analogue with arrays spinning about horizontal axes. Out-of-plane movement uses a vertically oriented, curved target and vertical spin axes. The gap between the arrays and the target was approximately one centimeter (more precision is impossible because of imperfections in the arrays and the target.) A single experiment ended as soon as there was contact between an array and the surface or the gap between them grew large enough to neuter the actuator.

Hardware: The induction couplers are Sparkfun Standard DC Gearmotors, each with a laser-cut cylinder containing one north- and one south-facing neodymium magnet. A 12V lead-acid battery powers the motors. The properties of the magnets and motors are in table 7.1. An Arduino microprocessor and Xbee radio enable remote open-loop commands and handle low-level motor control. A visual tag-based tracking system records the vehicle's heading and position with respect to the tags visible in figures 6.1 and 7.9. The aluminum target sits above the

Considerations: The arrays cannot be placed symmetrically about the CoM due to the constraints of the test platform. Similarly, the tracking points cannot be located at the CoM because the target occults it from the tracking system; the target plate was mounted directly above the vehicle out of necessity. These constraints mean that the experiments serve as a demonstration of individual motion primitives, rather than a full model validation.

7.4.1 Planar Movement

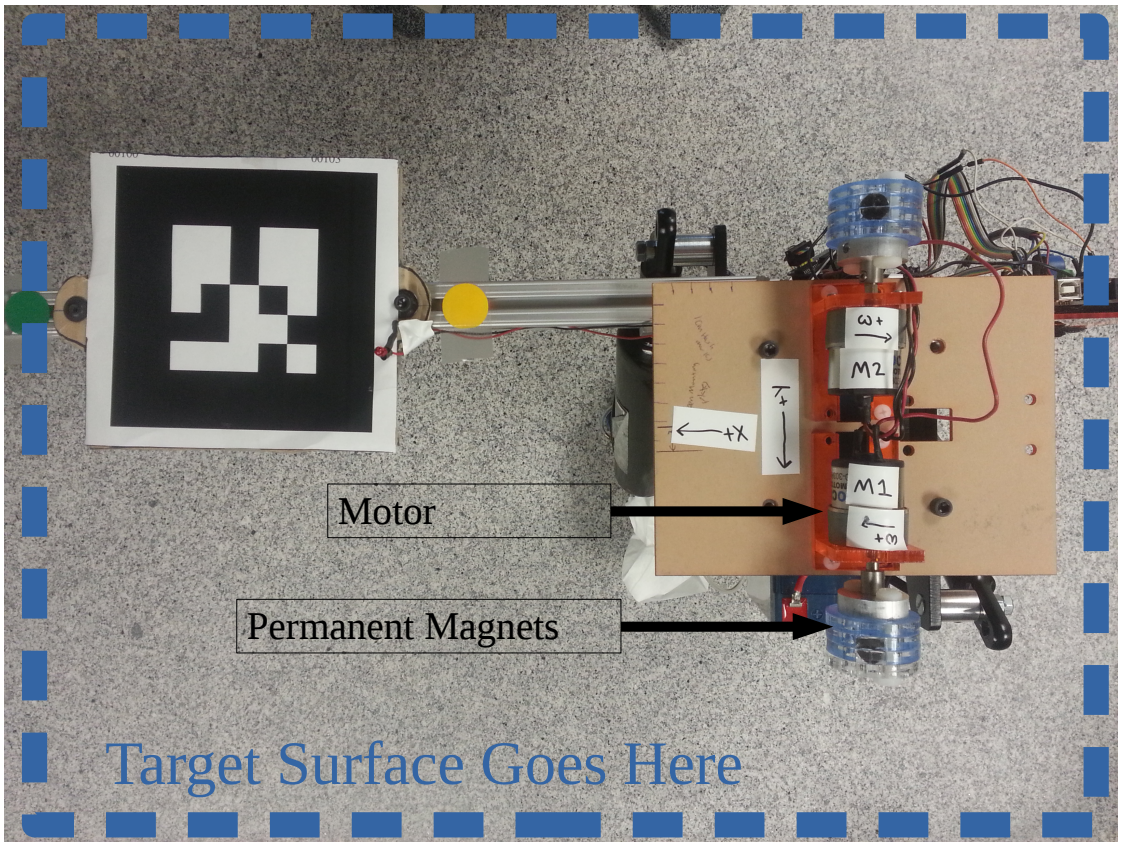

Figure 7.9: Overhead view of the platform for demonstrating induction-coupler-generated planar motion

Figure 7.10 shows the trajectory of the inspector during planar translation. The inspector spins both arrays forward to translate forward. The majority of the inspector is obscured because the arrays needed to remain directly under the target surface.

Figure 7.11 shows a maneuver in which the inspector uses induction couplers to rotate itself around the $-\mathbf{z}$ axis and then reverses its motion by generating torque around $+\mathbf{z}$. Note that $\hat{\mathbf{a}}_1 = \hat{\mathbf{a}}_2$, the opposite of the simulations.

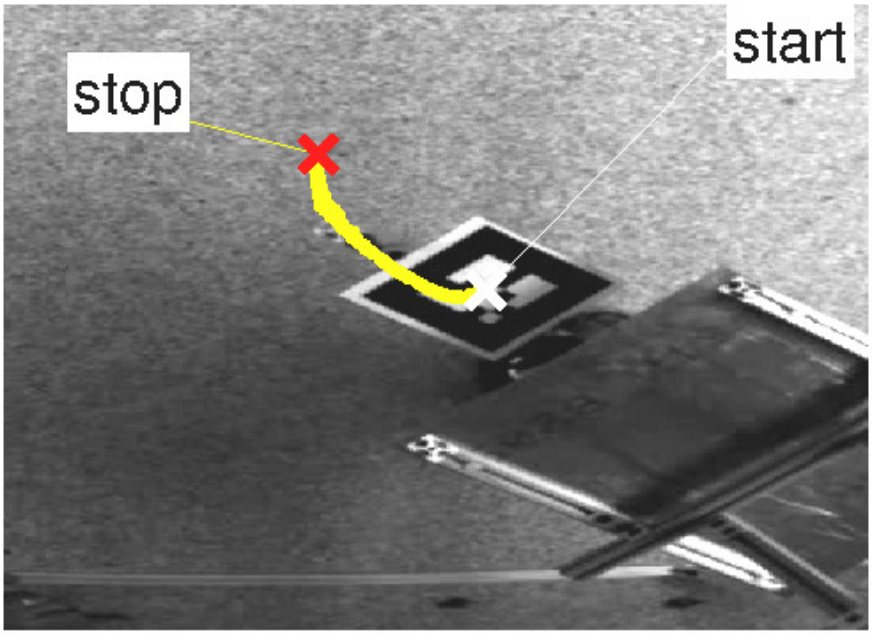

Figure 7.10: Trajectory during a planar translation maneuver. The body of the inspector is obscured by the target surface in the lower right part of the picture

7.4.2 Out-of-Plane Movement

Out-of-plane motion requires a different inspector-target setup when the experiments are restricted to three DOF The plate used to demonstrate out-of-plane movement has a curvature designed to match the Harmony module of the ISS. The out-of-plane demonstration inspector has two couplers, both with axes pointing in the $-\mathbf{y}$ direction, out of the page. Figure 7.12 shows the heading of the inspector as it rotates itself out of the plane about the $\hat{\mathbf{y}}$ axis. Figure 7.13 shows the closing gap as the inspector pulling itself towards the surface. Note that the distance it can travel before colliding with the plate is tiny, a clear motivation for closed-loop control.

Comparison between the average force in each primitive and its simulated coun-

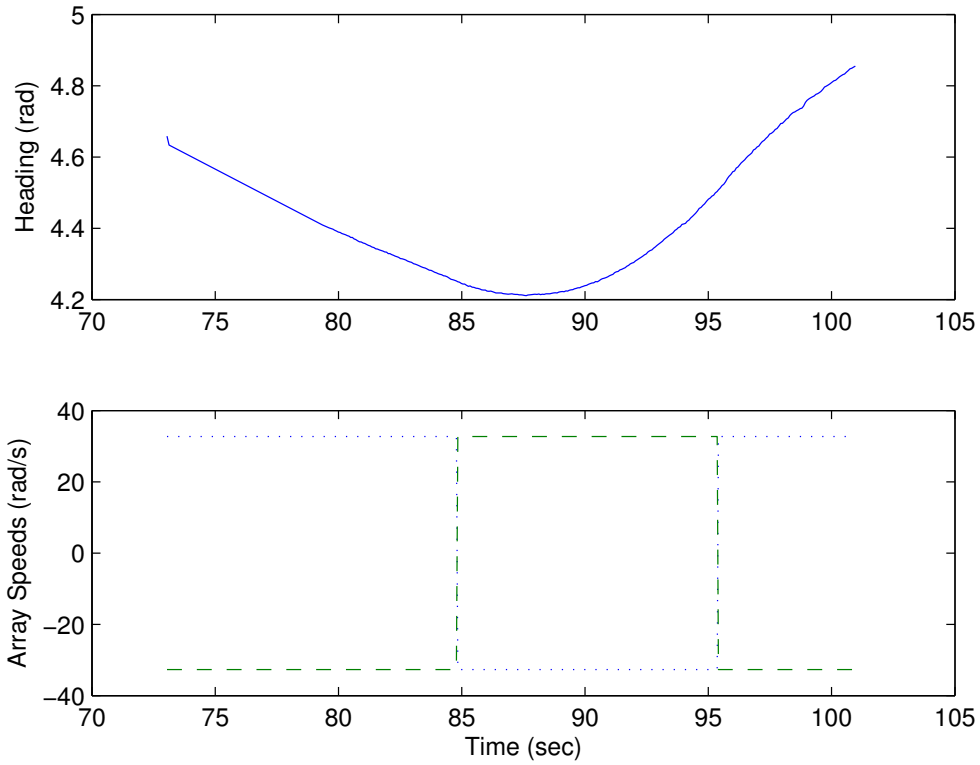

Figure 7.11: Inspector heading (top) and induction coupler speed (bottom) during open-loop planar rotation

terpart is critical in order to validate the force model and verify that the induction couplers are affecting the inspector's dynamics as expected. Out-of-plane translation provides cleanest force extraction because unlike the other three cases there there are no coupled torques, making it simple to find force of each coupler(f_c) from the distance between the inspector and its target ($d(t)$).

$$d(t) = x_t - x(t) = x_t - x_0 - v_0 t - \frac{1}{2m}(2f_c)t^2 \tag{7.5}$$

Here, x_t is the target's position, x_0 and v_0 are the inspector's initial position and velocity. m is the inspector's mass. The force falls out of the quadratic term in a quadratic fit to the data. In a similar manner, a Savitzky-Golay filter finds the average force during the other three noisier, torque-coupled primitives. The

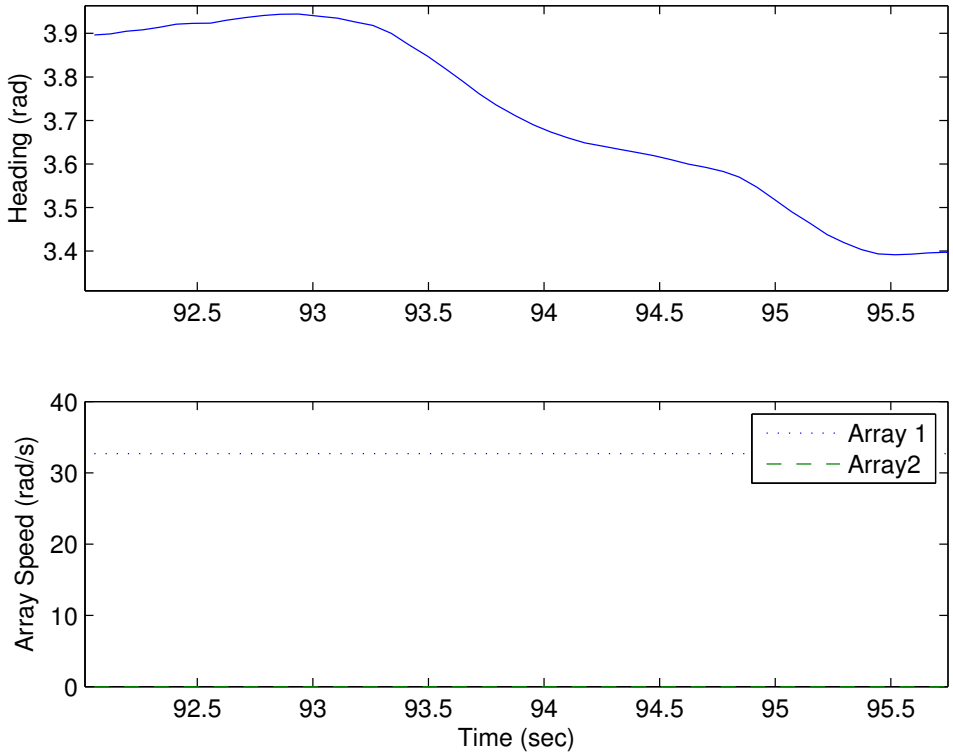

Figure 7.12: Inspector heading (top) and coupler speeds (bottom) during out-of-plane rotation

experimental forces compare favorably to those predicted by the coupler model in equations(7.2 - 7.4) and the simulations in section 7.3 when given the same parameters as the experiments. Table 7.2 shows a comparison of the simulated and experimental forces, verifying that the real actuator forces ($\mathbf{F}$) match the dynamics model ($\dot{x} = f(\mathbf{x}, \mathbf{u})$ in figure 7.1.

7.5 Multi-movement Trajectories

An inspector can chain together sequences of the four primitives to move between waypoints across the surface of a target. By connecting movements, the inspector

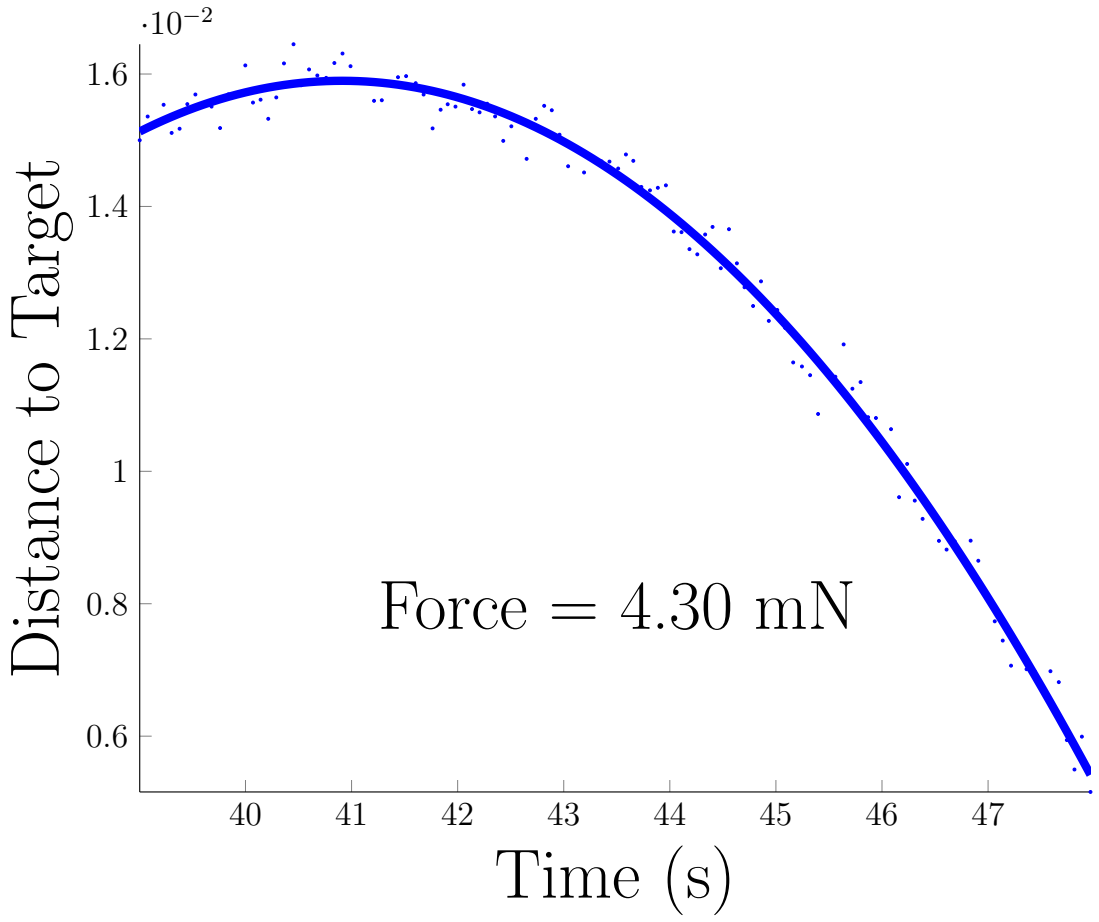

Figure 7.13: Distance between plate and center of tag during out-of-plane translation. A quadratic fit indicates a constant force of 4.30 mN

gains mobility, but movement sequences also introduce a new level of complexity. This section describes the considerations for a multi-movement controller and illustrates a trajectory in which an inspector chains together the four movements to move across the surface of an ISS module.

7.5.1 Zone of Safety

The state-dependent physics of induction couplers impose constraints on waypoint placement and maneuver sequencing:

Table 7.2: Simulated vs. Experimental Forces and Torques

Description	Experimental	Simulation	Units
Planar Translation	0.0151	0.0176	N
Planar Rotation	-0.0022	-0.0020	Nm
Out-of-plane Translation	0.0043	0.0037	N
Out-of-plane Rotation	-0.0018	-0.0012	Nm

The left-middle column shows the measured average force for translational movements and torque for rotational movements. The right-middle shows those same values from a simulation with the same physical parameters.

1. Waypoints need to be sufficiently close to the surface to maintain control.

2. Waypoints need to be sufficiently far from the surface to maintain safety.

Conditions (1) and (2) together define an operating 'zone of safety' near the surface. This zone can be thought of as a set of allowed waypoint states $\mathbf{w} \in \mathcal{Z}$ with $\mathbf{w} \in \mathbb{R}^{12}$. $\mathcal{Z}$ depends on the system dynamics

$$\dot{\mathbf{x}} = f(\mathbf{x}, \mathbf{u}) \tag{7.6}$$

which in turn are strongly tied to the inspector's configuration relative to its target.

Condition (1) encodes the dependence between an induction coupler's maximum force output and its distance from a conductive surface. If the waypoint causes large[1] gaps between the surface and a coupler, it will lose control authority. If enough couplers are rendered useless, the system can become uncontrollable and any velocity away from the surface will cause it to float off into space. Waypoints can prevent permanent uncontrollability in two ways: through proximity to the surface such that all the couplers are useful, or via a velocity component that will cause each coupler c_i, $i \in [1...k]$ to become useful at some time t_k in the future after the system dynamics drive its configuration,$\mathbf{x}_i$ closer to the surface. The closeness

condition can be expressed as:

$$\mathbf{w} \in \mathcal{Z} : \exists t_i \mid \forall c_i, \|\mathbf{x}_i(t_i)\| < r_{ineffective} \tag{7.7}$$

Condition (2) comes from the straightforward requirement that an inspector not crash into its target. Any waypoint needs to allow the inspector to stabilize itself without touching the target. In other words, a waypoint is unsafe if it will cause the inspector to crash regardless of control effort, $\mathbf{u}$. The distance condition can be expressed as:

$$\mathbf{w} \in \mathcal{Z} : \exists \mathbf{u}(t) \mid \forall t > t_0, \mathbf{x}(t_0) = \mathbf{w}, \mathbf{x}(t) \notin \mathbf{x}_{collision} \tag{7.8}$$

Determining Zone of Safety When is a waypoint in the zone of safety? How a planner asserts whether a given state is in $\mathcal{Z}$ can vary along a scale that trades decreasing computational and algorithmic complexity for increasing conservatism. The straightforward method to check a waypoint's inclusion in $\mathcal{Z}$ is to solve for a sequence of control inputs that satisfies both conditions on $\mathcal{Z}$. A non-convex optimization can encode both conditions directly and can verify that a point is in $\mathcal{Z}$. Verification with trajectory optimization is still slightly conservative because the inability to find a solution doesn't guarantee that the zone-of-safety conditions cannot be met. While straightforward and minimally conservative, this approach is computationally expensive, doesn't guarantee convergence, and requires significant parameter tuning.

[1]The distance where a coupler becomes ineffective depends on the coupler's properties, the inspector's properties, and the system's state.

A different approach is to encode $\mathcal{Z}$ in terms of system dynamics and actuator work:

$$T \leq \max \left(\int_S \mathbf{F}_{couplers} \cdot d\mathbf{s} \right) \tag{7.9}$$

where T is the system's linear kinetic energy, and $\mathbf{F}_{couplers}$ is the total force produced by the inspector's induction couplers. S is the worst-case path – the path that makes it as hard as possible for the inspector to prevent itself from achieving escape velocity or from crashing into the surface. The work-energy condition is more conservative than the optimization approach, because it requires the inspector to have the ability to bring itself to a stop (dissipating its translational kinetic energy) instead of simply avoiding the surface or an escape trajectory.

Lyapunov functions can verify that a waypoint is in $\mathcal{Z}$. This check is the most conservative method of the three but also the easiest to implement and compute. A waypoint is in $\mathcal{Z}$ if there exist a set of gains and a stable point that has a region of attraction including the waypoint but excluding the target surface. By definition, the inspector won't leave the region of attraction and will not crash or permanently escape. More details on algorithmically finding and verifying regions of attraction are in chapter 8.

7.5.2 Multi-Movement Considerations

In addition to the zone of safety constraints, the unique physics of induction couplers introduce several considerations for trajectory generation. The straddle consideration encodes the geometric requirement that the induction coupler system needs a non-flat surface to generate a force towards the target (recall figure 7.4.) The force from each coupler will always have a component perpendicular to, and

pointing away from, the closest point on the surface (recall equation 7.3.) As such, the inspector needs to use the net force from all of its couplers to produce a net force directly towards the target. Larger angles between the vector directed towards the target's center and the vectors from each coupler to its closest surface point will decrease the components of the surface-perpendicular force that points directly away from the target, thus making attractive forces easier. Additionally, the spin axes of any coupler pair coupler producing attractive forces need to have a component parallel to the curve's axis. The upshot is that 'straddling' the surface between two or more couplers is a good strategy when the inspector needs to move towards the target or maintain a certain distance. A path-planning algorithm should select waypoints accordingly.

An inspector can execute any motion with either of two control laws, but it is better to use a different law for long maneuvers than stabilization. Like traditional thrusters[111], induction couplers can provide quick impulses or sustained closed-loop control. Each of these strategies serves a different purpose: impulsive actuation should generate velocity for large rotations or translations, while continuous control is best for stabilizing the inspector's state and adjusting its configuration. While technically either approach could be used for both purposes, the nature of induction coupler forces encourages this mode-separation for two reasons: nonlinearities and repulsive forces. While the system can be linearized so that a feedback controller can stabilize it to a trajectory or waypoint, its nonlinearities make feedback control impossible for large translations or rotations. This leaves open the possibility of a strategy like model predictive control [15]. However, recall that one component of an induction coupler's force always points directly away from the target surface. This repulsive component increases relative to the total force with the coupler's speed. As such, both bang-bang control (using im-

pulses for closed loop control) and sustained force in a single direction during a long movement will both tend to drive the inspector away from the surface and eventually out of the zone of safety.

7.5.3 Example Trajectory

The example trajectory in figure 7.14 has five phases. Each one is an example of a different maneuver that an inspector like the one in figure 7.15 would use to locomote over the surface of a large target like the ISS' Harmony Module.

1. Translation parallel to the surface in the direction of the curve's axis.
2. Rotation in the plane parallel to the surface.
3. Translation towards and away from the surface.
4. Translation parallel to the surface along the curve.
5. Rotation out of the plane parallel to the surface.

In step 1 the inspector moves along the module's z axis. It creates an impulsive force and momentum in the $+\hat{z}$ direction by spinning the couplers with axes perpendicular to the desired motion in a short burst with angular speed ω. This impulse will also generate momentum away from the target, which if left unchecked would drive the inspector out of the zone of safety. It uses couplers c_2 and c_4 with a simple PD controller to maintain a constant distance from the target throughout the step. Finally, as it nears the waypoint, the inspector activates a (different) PD controller for couplers c_1 and c_3 to dissipate its velocity from the initial impulse.

$$t_0 \leq t < t_1$$

$$^1\mathbf{u}_{imp} = \{t_0 < t < t_0 + \Delta t : [\omega\ 0\ \omega\ 0\ 0\ 0]^T\}$$

$$^1\mathbf{u}_{pd1} = (-k_p x_1^{err} - k_d \dot{x}_1^{err})[0\ 1\ 0\ \ -1\ 0\ 0]^T$$

$$^1\mathbf{u}_{pd3} = \{x_3^{err} < \Delta x_3 : (-k_p x_3^{err} - k_d \dot{x}_3^{err})[1\ 0\ 1\ 0\ 0\ 0]^T\}$$

In step 2 the inspector rotates a full 90 degrees in the plane parallel to the surface. c_1 and c_3 spin in opposite directions to produce an impulsive torque about the global $-\hat{x}$ axis. The inspector then rides its angular velocity to a new orientation. Unlike step 1, there is no distance holding feedback control[2]— the drift away from the target prevents any of the couplers from crashing into the surface. As in step 1, a PD feedback loop slows the inspector at the end of the maneuver, this time based on its angular orientation.

$$t_1 \leq t < t_2$$

$$^2\mathbf{u}_{imp} = \{t_1 < t < t_1 + \Delta t : [-\omega\ 0\ \omega\ 0\ 0\ 0]^T\}$$

$$^2\mathbf{u}_{pd\phi} = \{\phi^{err} < \Delta\phi : (-k_p \phi^{err} - k_d \dot{\phi}^{err})[-1\ 0\ 1\ 0\ 0\ 0]^T\}$$

In step 3 the inspector repositions itself closer to the surface after the drift during step 2. c_5 and c_6 are now oriented parallel to the cylinder's axis and produce forces perpendicular to the surface by counter-rotating according to a PD controller.

$$t_2 \leq t < t_3$$

$$^3\mathbf{u}_{pd1} = (-k_p x_1^{err} - k_d \dot{x}_1^{err})[0\ 0\ 0\ 0\ 1\ \ -1]^T$$

In step 4 the inspector translates along the surface in the $-\hat{y}$ direction by briefly using the same inputs as step 1 to impulsively generate momentum and maintaining distance according to the strategy in step 3. In-plane translation perpendicular to the curve's axis differs from translation parallel to the curve's axis because the

movement doesn't preserve the inspector's orientation with respect to the surface. Instead, the inspector will appear to rotate with respect to the surface, bringing some couplers closer and some farther away. The gap between one set of couplers and the surface would eventually render them ineffective.

$$t_3 \leq t < t_4$$

$${}^4\mathbf{u}_{imp} = \{t_3 < t < t_3 + \Delta t : [\omega\ 0\ \omega\ 0\ 0\ 0]^T\}$$

$${}^4\mathbf{u}_{pd2} = (-k_p x_2^{err} - k_d \dot{x}_2^{err})[1\ 0\ 1\ 0\ 0\ 0]^T$$

In step 5 the inspector rotates about $\hat{z}$ to reorient after translating. It uses a PD controller and a single coupler to drive itself back to an orientation where each set of couplers are equidistant from the surface. During this movement there is also an inevitable force tangential to the surface, undoing some of the progress in step 4.

$$t_4 \leq t < t_5$$

$${}^5\mathbf{u}_{pd\psi} = (-k_p \psi^{err} - k_d \dot{\psi}^{err})[0\ 0\ 0\ 0\ 0\ 1]^T$$

The inspector in the simulation shown in figure 7.15 is a hybrid between the simple inspectors that demonstrated single movements. It has a set of additional couplers so that it can control its distance from the surface in both its starting orientation and after rotating 90 degrees. This illustrates an inherent flaw in designs with fixed coupler positions that section 7.6.1 discusses further.

During the simulation, the inspector zeros its linear and angular velocity between each maneuver. In practice, this would be done by one LQR (Linear

[2]Distance-holding feedback control is possible but was not implemented for simplicity.

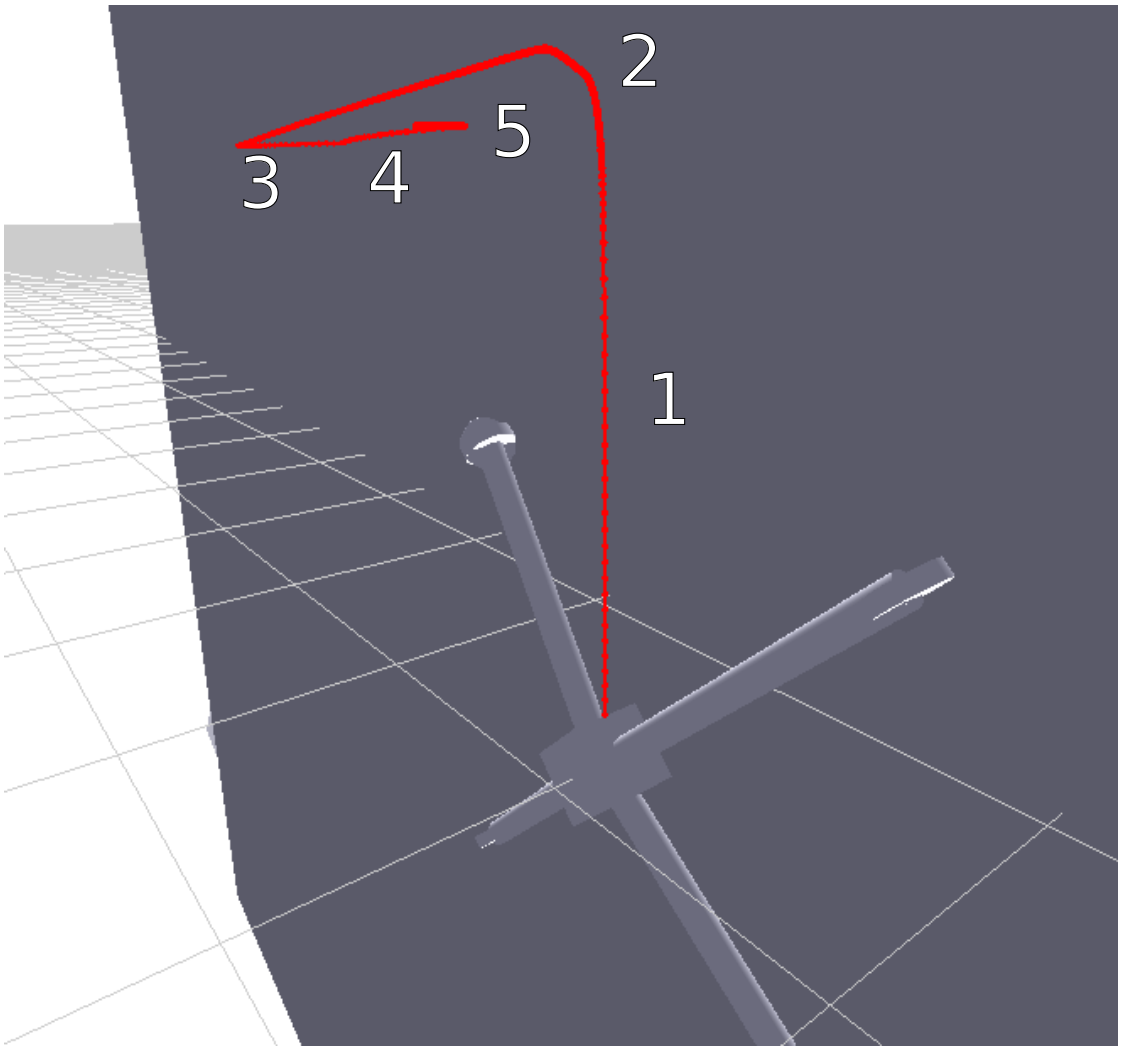

Figure 7.14: Multi-motion trajectory using all four motion primitives.

Quadratic Regulator) controller built from a system model linearized around the waypoint or several local LQR controllers clustered around the waypoint. Other work discusses this strategy, so for simplicity the simulation starts step n at $\mathbf{w}_{n-1}$ as long as the inspector reached with low velocity and a small pose offset.

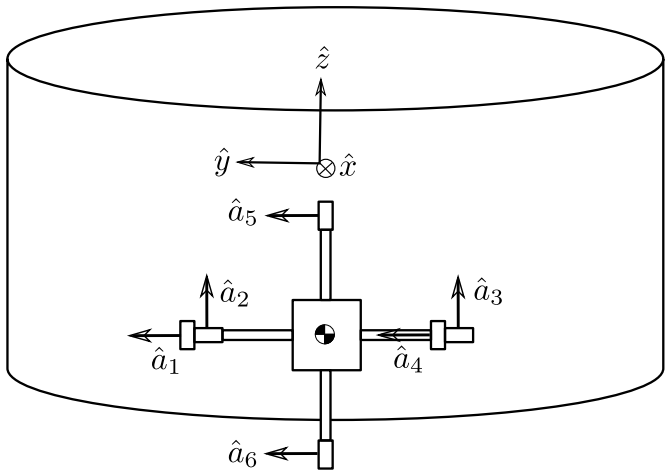

Figure 7.15: Diagram of the setup for an example trajectory composed of multiple motions.

7.6 Discussion

The experiments and simulations of induction coupled motion primitives have several implications for the inspection spacecraft's design, trajectory generation, and physical implementation.

7.6.1 Design Lessons

The design of inspector's structure, its control laws, and waypoint selection should all take into account the zone-of-safety conditions. Control authority over the gap

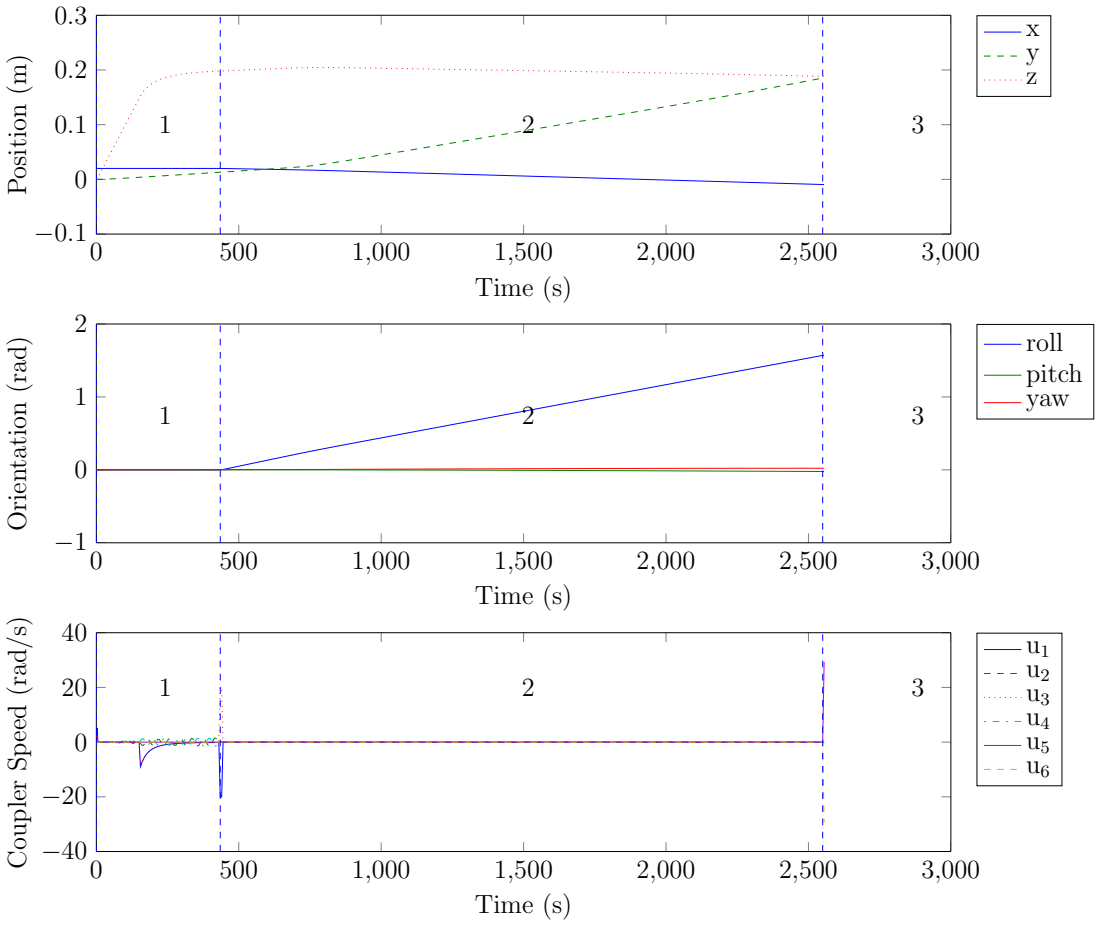

Figure 7.16: Inspector position, heading and control during maneuvers one and two.

between the inspector and the target surface is essential to satisfy both conditions of the zone of safety. The inspector achieves this control authority by positioning two couplers spin axes parallel to a curve's axis close enough to surface to be effective. It can do this through careful rigid-body motion or reconfigurable couplers which places a design restriction either on feasible trajectories or the coupler's physical attachments. In the first case, any would need to account for the coupler's configuration at all time, and in the second case the couplers could mount to actuated limbs.

The inspector's velocity can easily drive it out of the zone of safety — send-

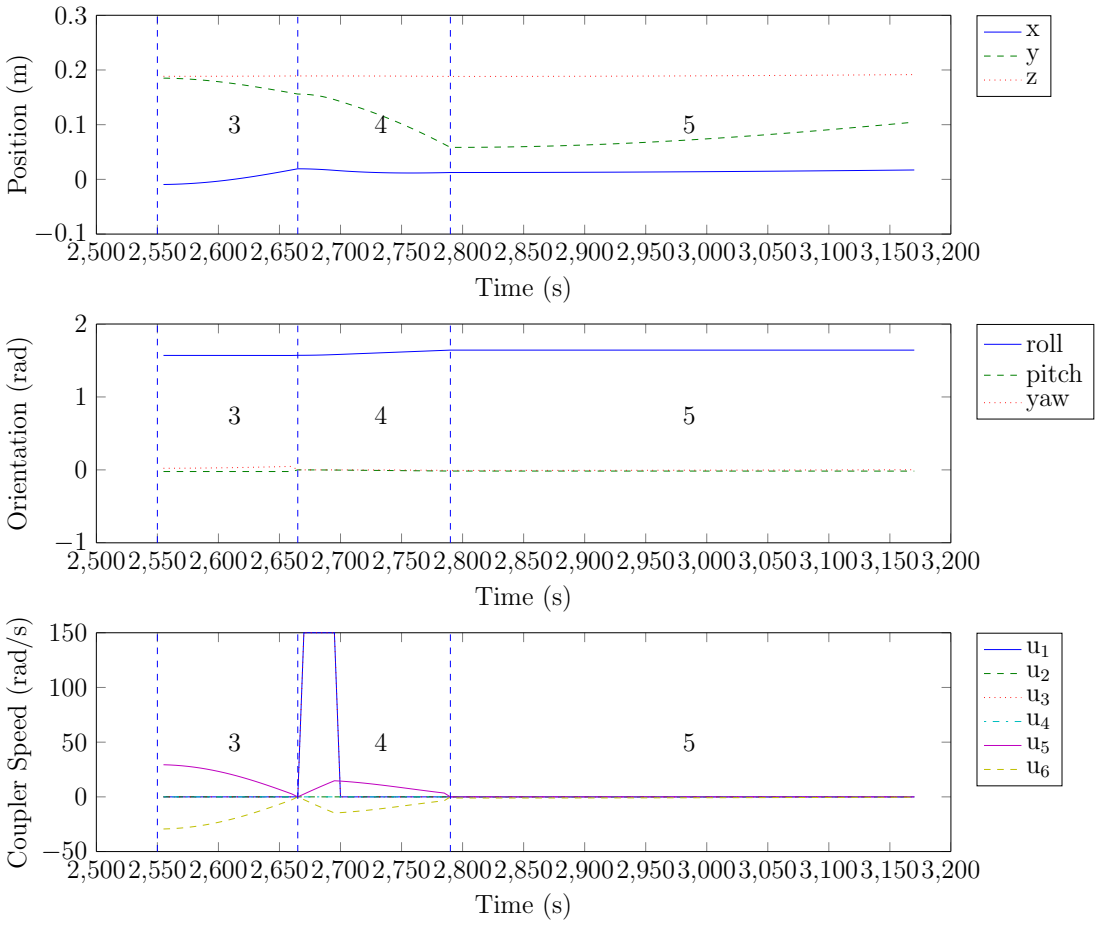

Figure 7.17: Inspector position, heading and control during maneuvers three through five.

ing it flying off into space or crashing into the surface. Trajectories can encode this danger by capping waypoint velocities and generating impulses accordingly. Many experiments, both real and simulated, left the zone of safety because the couplers applied a force for too long. Since the system has no inherent resistance to displacement or velocity, the damping ratio, ξ, is entirely dependent on the closed-loop gains. Without an appropriate selection of proportional and derivative gains (k_p and k_d) the inspector will overshoot waypoints, escape the zone of safety, and encounter disaster. To create a safely damped system, the control gains should

enforce

$$\xi = \frac{k_d}{2\sqrt{mk_p}} \geq 1 \tag{7.10}$$

Controllers and trajectories should also account for the nonlinear relationship between an induction coupler's input speed and output force. Recall that as a coupler's speed increases, its force component perpendicular to the target increases faster than the parallel component. The rotating force vector can cause input commands to drive the inspector away from the surface, even when that input is supposed to pull it towards the surface! This danger is another reason for the path planner to limit maximum command velocities and for control laws to use closed-loop gains that create a critically damped system.

7.6.2 Physical Implementation

The simulations in sections (7.3,7.5) and the experiments in section 7.4 reveal several possible improvements for future induction coupler systems. Hybrid controllers and mechanically mobile couplers could both address the system's extreme sensitivity to environmental geometries. Even during simulations, accumulated numerical errors could be enough to disrupt an open loop trajectory. In the experiments, modeling errors from inevitable misalignments in motors and measurement uncertainties led to several unexpected effects including stronger force/torque coupling and smaller zones of safety.

It is well known that feedback control can compensate for disturbances and modeling errors. However, the control laws for each motion primitive depend on an appropriate configuration for executing that maneuver. For example, a pair of couplers need to be oriented with axes perpendicular to the desired motion

to control translation in that direction. Thus, an effective controller needs both discrete and continuous components, with guards on the discrete transitions to protect the system from executing an inappropriate control law given the system's true configuration.

Mechanically mobile couplers offer another approach to robustness. The configuration of each coupler is a dominating effect on actuation forces, so even a small decoupling between the coupler's position and the inspector's CoM will lead to more control authority. The static coupler arrangement on the experimental and simulated inspectors has the advantage of simplicity, but the associated restrictions ultimately make static arrangements a poor choice. Instead, couplers could mount to the end of actuated arms that move them relative to the inspector's body. Several studies address the additional levels of control that reconfigurable space robots require[116][66]. Speculatively, the inspector could treat its actuators as a distributed system, with each coupler measuring its own distance and orientation to the surface, collaborating with others to achieve the larger goal of controlling the body's state. Ultimately, the position and orientation of the couplers makes the difference between success and failure so its a good strategy to maximize control over these key state variables.

7.7 Conclusion

This chapter presents a system that can actuate an orbital inspection vehicle in six DOFs near a conductive surface without mechanical contact. Induction couplers enable contactless, propellantless motion on orbit — a unique capability that can form the basis of orbital servicing missions. The construction of a generalized

model enables fast dynamic simulations of an inspector using multiple induction couplers to actuate near a target surface. These couplers enable four different open-loop maneuvers that together span 6-DOF: planar translation, planar rotation, out-of-plane translation, and out-of-plane rotation.

Theory and experiment show that couplers rotating on axes parallel to the plane generate planar motion similarly to a differential drive. Two or more couplers can take advantage of the surface geometry to generate motion out of the plane parallel to the target. This arrangement generates force in the $\hat{z}$ direction by two or more creating shear forces whose $\hat{x}$ and $\hat{y}$ components cancel but whose $\hat{s}$ components add. Flipping the direction of only one of these couplers produces a torque coupled with a force, enabling rotation out of the plane. Simulations demonstrate each of these four maneuvers in an ideal scenario and a prototype system on a low-friction air table shows that they work in practice as well as theory. A full three-dimensional trajectory illustrates the capabilities and challenges of composing multiple primitives.

Future work will focus on two areas: adaptive controllers and movement planning. A robotic inspector will need adaptive controllers to account for induction coupler's strong dependence on poorly known parameters of the environment. The inspector will also need to plan movements carefully because its ability to exert control with an induction coupler is based on both its kinematics and the local geometry.

CHAPTER 8

PROBABLILISTIC DESIGN/CONTROL CO-CREATION

This chapter introduces a new approach to algorithmic dynamical system design. Our probabilistic co-generation method uses techniques from evolutionary design, motion planning, and controller verification to generate designs and evaluate them on controller coverage. This process results in physical design parameters and a multi-query controller. These together attempt to maximize the volume of state-space that the system can explore without becoming unstable. Algorithmically generated designs that can safely reach many goal states are especially valuable to our motivating system: an inspector spacecraft using induction couplers. The inspector exhibits a confluence of problematic characteristics for traditional co-generation methods - complex dynamics, multiple goal states, and high dimensionality. While designed for a specific system, this method is broadly applicable to the design of systems with similar characteristics.

Why does the world need another approach to algorithmic design and controller synthesis? New technologies enable systems that fall through the holes in the existing methods.[1] Consider the induction inspector in chapter 3. Unlike a free-flying inspection vehicle [17], it uses novel electromagnetic actuators that allow it to grapple surfaces without mechanical contact. These actuators have advantages, requiring no propellant, but a poorly designed controller can send the inspector spinning into space. The probabilistic co-generation approach can unlock multi-query controllers for an entire class of systems with nonlinear, high-dimensional

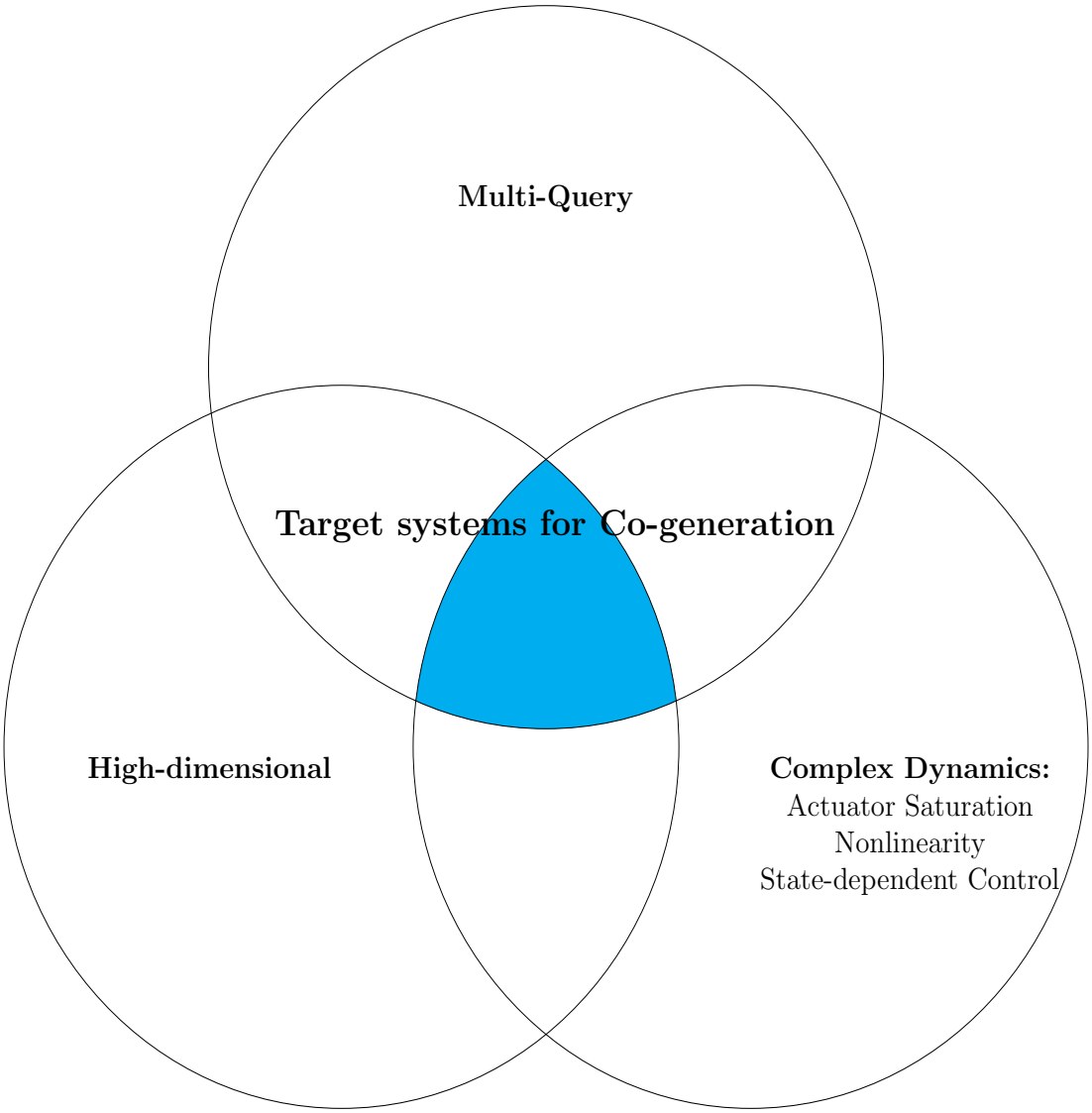

Figure 8.1: Probabilistic co-generation addresses high-dimensional, multi-query systems with complex dynamics.

dynamics and limited control authority (figure 8.1.)

8.1 System Description

The probabilistic co-generation method is meant for complex dynamical systems where other methods fall short. In general, these systems have nonlinear, state-

[1]See section 6.3 for state-of-the-art in algorithm-based design/control synthesis

dependent actuators, a high dimensional state space, and many stable points. Consider a many-link pendulum with limited actuators at each joint. The actuators are sufficient to hold the joints in many stable configurations, but other states can't be kept from chaotic motion. More complicated real-world examples include some underactuated walkers [37] and many electromagnetically actuated systems [96] including the inspection spacecraft described in subsection 8.1.2.

8.1.1 General System Description

Co-generation targets systems with parameterized designs, $\mathcal{D}(\mathbf{p})$ where $\mathbf{p}$ are mutable and numerical parameters of the system. In the thought experiment, $\mathbf{p}$ are the length and mass of each pendulum link. These parameters are either discrete (number of links) or continuous (properties of the links.) $\mathcal{D}$, along with fixed parameters and information about the environment, must have enough information to numerically model the system.

$\mathcal{D}$ and the independent environment variables[2] specify the nonlinear dynamics of the system with a state $\mathbf{x}$ and control input $\mathbf{u}$.

$$\dot{\mathbf{x}} = f(\mathbf{x}, \mathbf{u}) \tag{8.1}$$

A controller $\mathcal{C}$ defines a set of control actions $\mathbf{u}$(t,$\mathbf{x}$) that can drive the system to a stable goal state, $\mathbf{x}$_G. The total volume of the regions of attraction in $\mathcal{C}$ define V($\mathcal{C}$) - the volume of state space that $\mathcal{C}$ can successfully drive to some $\mathbf{x}$_G. While V($\mathcal{C}$) has little meaning in an absolute sense, it provides a metric to compare

[2]Independent environment variables can be fixed design parameters (like a fixed mass) or external factors that affect the dynamics, like an external magnetic field

different $\mathcal{D}$ based on how much state space they can explore before "wandering" into a possibly unrecoverable state.

In general, the co-generation problem is to find a $\mathcal{D}$ and $\mathcal{C}$ that create a system that exhibits some desired performance. In the toy example, performance is based on possible joint configurations and in the motivating example, performance is based on controllable rigid-body configurations. The larger the set of achievable configurations, the better the performance.

Traditional human-intuited or optimization-based design and controllers fall short when there exists a combination of:

- $\mathbf{x}$ is high dimensional.
- $\mathbf{p}$ is high dimensional.
- f($\mathbf{x}$,$\mathbf{u}$) is nonlinear and not analytically solvable.
- $\mathbf{u}$ saturates, especially if $\mathbf{u}_{max}$ and $\mathbf{u}_{min}$ are functions of $\mathbf{x}$.
- The system cannot be controlled over all of state space, regardless of the design.
- Unknown goal specifications and a large number of possible goal points.

The dimensionality of $\mathbf{p}$ and $\mathbf{x}$ that constitute 'high dimensional' varies based on the behavior of the other criteria. High dimensional systems with slowly changing dynamics and state-independent actuators are often still amenable to optimization-based design. At some dimension, human intuition breaks down and optimizers fail to converge. In these cases, a probabilistic approach to both the design and control may be needed.

8.1.2 Motivating System Description

The real-world system motivating this approach is a robotic inspection spacecraft using induction couplers for contactless manipulation. Induction couplers create actuation forces from the interaction between time-varying magnetic fields of spinning magnets or oscillating electromagnets and induced currents in conductive targets. These forces allow a spacecraft to manipulate a target and locomote itself without physical contact at distances of several centimeters.

Induction couplers enable unique capabilities, but also exhibit the behaviors that make traditional design-and-then-control difficult. The rigid body system itself has a 12 dimensional state space. Each actuator could be placed anywhere on the inspector, with any orientation - six parameters per actuator. The actuation forces both increase nonlinearly and change direction with the control input. The actuation force's direction and magnitude also depend on the distance and relative orientation between the surface and the actuator. With enough distance, the actuators become effectively useless which can cause the system to become uncontrollable if too many actuators are too far from the target. Finally, a robotic inspector needs the ability to stabilize itself in many different configurations. With this complexity and number of free parameters, creating a design without considering its associated controller could lead to systems with poor performance. The actuators' nonlinear, state-dependent, and saturated response make it hard to intuit a design that can lead to a useful controller. Algorithmic co-generation is a natural solution.

This chapter includes:

- A new probabilistic algorithm for simultaneous design and control (section

8.2.)

- A comparison showing that the algorithm converges on a known optimal solution in a simple system (section 8.4.1.)
- Experimental validation that the algorithm beats human design in a comp (section 8.4.2.)

8.2 Algorithm

The goal of the algorithm is to find both a design, $\mathcal{D}$, and controller, $\mathcal{C}$, that together maximize the volume of state space over which the controller can successfully stabilize the system. This controller is composed of a set of local control gains associated with both a stable point $\mathbf{x}$ and a RoA of the gains about $\mathbf{x}$. Each RoA is an analytically defined ellipsoidal level set ρ. The closed-loop system employing the gains associated with ρ converges to $\mathbf{x}$ from any point within ρ. Because all $\mathbf{x}$ in $\mathcal{C}$ are stable points of the system, the system can stabilize any state that lies within any ρ. Together, the total volume of state space covered by all the ρ in $\mathcal{C}$ creates a "controllable volume", $\mathrm{V}(\mathcal{C})$.

By its nature, the controllable volume is a conservative proxy for the amount of state space the system can visit and then return to a stable point. The controllable volume addresses both concerns of the system: the ability to achieve as many states as possible and to do so safely, without either drifting away (a state that can never be stabilized) or violating constraints like 'don't crash' that can be encoded in the various ρ. Thus, the controllable volume in algorithm 1 makes a good fitness function for exploring the design space.

The controllable volume can act as a fitness function for exploring the design-

Algorithm 1 Find Controllable Volume

$\mathcal{D} \Leftarrow$ input design
for i = 1 to max_controllers **do**
  $\mathbf{x} \Leftarrow$ random state $\in$ stable states
  [**A**,**B**] $\Leftarrow$ linearization of $\mathbf{f}(\mathbf{x},\mathbf{u})$ around $\mathbf{x}$
  [**K**,**S**] $\Leftarrow$ LQR(**A**,**B**,**Q**,**R**)
  $\rho \Leftarrow$ level set for the closed loop system using **K** about $\mathbf{x}$
  $\mathcal{C}$.add-node($\mathbf{x}$,**K**,**S**, ρ)
end for
for all node $\mathcal{N}$ in $\mathcal{C}$ **do**
  if $\rho_i \cap \rho \neq \emptyset$ **then**
    $\mathcal{C}$.add-edge(ρ_i, ρ)
  end if
end for
OUT = Volume($\mathcal{C}$)

space through one of four algorithm classes: stochastic search, grid-based search, gradient-based optimization, and genetic algorithms. A stochastic design-space exploration (shown in algorithm 2) is fast, but has the downside that improvement over multiple iterations is random. Both grid-based searches and gradient-based optimization fail on the high-dimensional systems in question. Genetic algorithms are a good compromise because they systematically attempt to improve on each iteration, while avoiding the full computational complexity of most optimization methods.

Algorithm 2 Stochastic Design-Space Exploration

$\mathcal{C}$.init(NULL)
best_V $\Leftarrow$ 0
best_design $\Leftarrow$ NULL
while no_convergence **do**
  $\mathcal{D} \Leftarrow$ new parameterized design
  V $\Leftarrow$ Stochastic Control-Volume($\mathcal{D}$)
  if V > best_V **then**
    best_V $\Leftarrow$ V
    best_design $\Leftarrow \mathcal{D}$
  end if
end while

8.2.1 Algorithm Execution

While the algorithm hasn't exceeded a total number of loops set by `max_iterations` and improvements in the fitness function haven't stalled (the number of loops without a better $\mathcal{D}$ hasn't exceeded `max_no_improve`), the algorithm iteratively generates new designs, controllers, and their associated fitness functions. $\mathcal{D}$ and the independent environment variables define a new dynamical system that needs a controller. This generation can either be stochastic (high speed with no guarantees) or part of a genetic algorithm.

The algorithm populates the controller by first picking a state from the set of stable states, defined either explicitly (with a pre-defined range for a continuous set of points) or implicitly (with a function that checks the stability of each sampled point.) It then linearizes the system about that state and finds the LQR gains for that linearized system. SOS finds a verified polynomial level set ρ that is added to the controller along with the LQR gains. This process proceeds until it meets a termination condition like reaching some maximum number of gain nodes.

Once the controller is fully populated with gain nodes, a graph is created by generating an edge between gain nodes. A conservative connection policy connects only two nodes $\mathcal{N}_1$ and $\mathcal{N}_2$ with $\mathbf{x}_1$ and $\mathbf{x}_2$ such that $\mathbf{x}_1 \in \rho_2$ and $\mathbf{x}_2 \in \rho_1$. The fitness function returns the total volume filled by the RoAs in the controller.

The algorithm returns a design $\mathcal{D}$ and an accompanying controller $\mathcal{C}$ that maximize stabalizable volume.

8.2.2 Controller Execution

A possible control policy using $\mathcal{C}$ is as follows:

Start with an initial state $\mathbf{x}_0$ and a target state $\mathbf{x}_G$. Find two gain nodes, $\mathcal{N}_0$ and $\mathcal{N}_G$ such that whose level sets encompass $\mathbf{x}_0$ and $\mathbf{x}_G$ respectively. Perform a graph search to connect the two nodes and generate a series of waypoint nodes $\mathcal{N}_1$ ... $\mathcal{N}_k$. Assuming the connection policy in section 8.2.1, while inside ρ_i the system should use $\mathbf{K}_i$ until it is inside ρ_{i+1} and then switch to $\mathbf{K}_{i+1}$, effectively "hopping" between nodes. This policy provides stability guarantees because the system is always driving itself towards a stable point while within the RoA of that point and using the gains associated with that RoA. Figure 8.2 shows the RoAs and associated path for a simple example.

The system can then use other path planners to reach stable states near the node states. One approach is to generate a new sequence of nodes with overlapping RoAs that lead to the goal state, like a fractal of the larger map. This approach assumes smooth dynamics, but the RoA of the node state already makes that assumption.

This control policy is not optimal and leaves significant room for improvement because moving this way gives no performance guarantees beyond stability. It is meant to illustrate how the results of the co-generation algorithm can be incorporated into a control policy that allows the system to traverse volume of $\mathcal{C}$ without additional controller synthesis. Further discussion of control policies is in section 8.5.2.

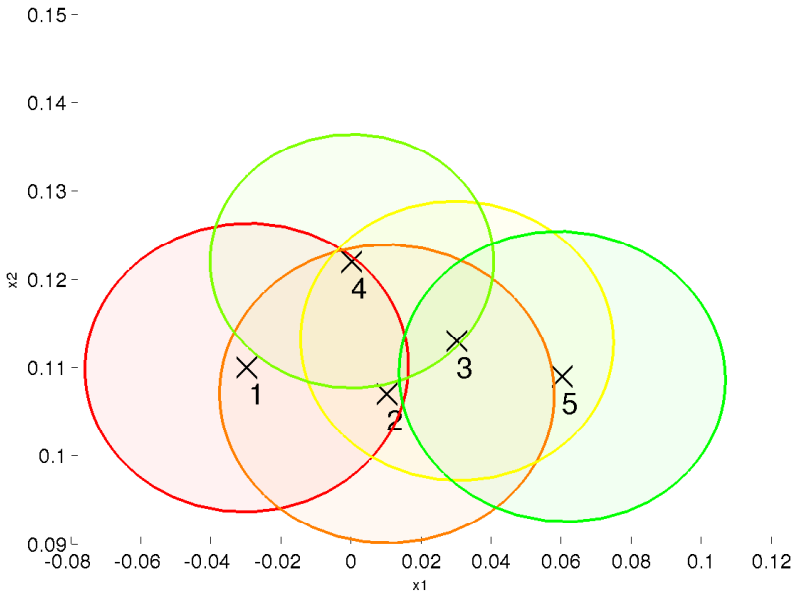

(a) Two-dimensional regions of attraction.

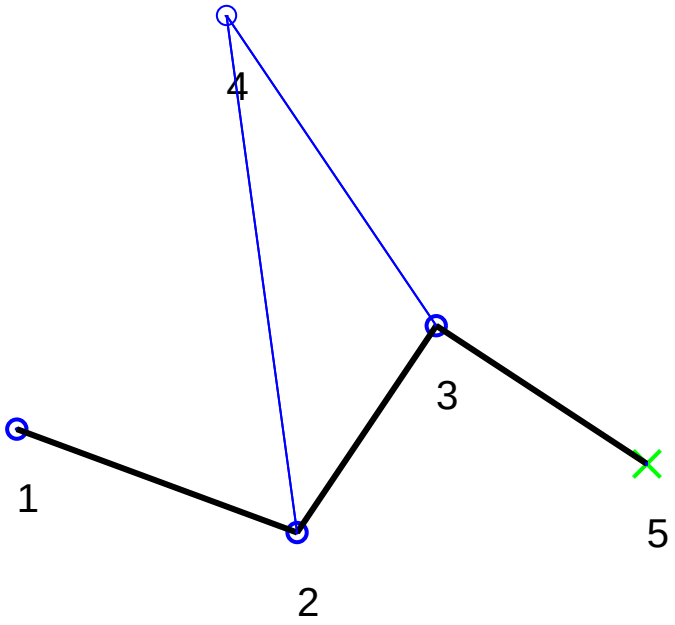

(b) Graph and example control-gain-path from node 1 to node 5.

Figure 8.2

8.3 Implementation Details

The number of gain nodes necessary to allow controllers to cover possibly controllable states varies with the smoothness of the dynamics. $V(\mathcal{C})$ can converge with a smaller `max_controllers` when the gradients of the dynamics are small and the RoA for individual nodes are large compared to the size of the state space. The user needs to pick the parameters built into the controllers unless they are included as design parameters. In our example the matrices $\mathbf{Q}$ and $\mathbf{R}$ that generate LQR gains are built-in controller parameters.

Different regions of state-space may be more important than others. The algorithm can incorporate this information in two ways. One option is to assign more weight towards picking node centers in a region of interest during the sampling step. Another option is adding weight to points in the region of interest during the integration step. Our implementation assigns the same weight to each state.

Several different methods can find a RoA for each gain node. SOS is the most widely used and toolboxes like `SPOT` [59] simplify the process of generating and manipulating Lyapunov functions. However, SoS does not scale well to high dimensions. Alternatives include simulation-based approaches, DSOS programming and SDSOS programming [1].

Numerical methods are necessary to find the volume of each controller because there is no good way to find the volume covered by several overlapping ellipses analytically. We use Monte Carlo integration because of the high dimensionality. In our implementation, a set of points from the Halton sequence is generated across the convex hull of the controller and each point checks whether it is contained in any RoA. The Halton sequence's deterministic sampling points allow volumes to

be reliably compared while still exhibiting the large dispersion needed to capture high-dimensional volumes. There are many increasingly fancy ways to implement Monte Carlo integrators for more accuracy.

The samples from the integration step also populate the edges of the controller's graph. Each point is already checking whether it is in any RoA, which in the worst case checks each RoA in the controller. To populate the graph, the sample points check whether they are in each RoA, keep track of the RoAs containing them, and then add an edge between all gain nodes associated with those RoAs.

There are many evolutionary algorithms, each with several parameters. CMA-ES[34] is a strong choice because it is derivative-free and designed for non-linear but continuous problems. CMA-ES has easy-to-use open source implementations in most major languages [5]. Any optimization algorithm's convergence is sensitive to many input parameters, and evolutionary algorithms are no exception. However, CMA-ES found feasible designs in two unrelated systems using its default parameters and the control-volume fitness function, suggesting that it is a good choice for probabilistic design-control.

8.4 Experiments

We demonstrate the co-generation algorithm with two systems: a double pendulum and a robotic inspection spacecraft using novel actuators . The pendulum is a simple example demonstrating that the algorithm converges on a known optimal design. The spacecraft system shows how the co-generation algorithm can generate designs for systems that are intractable for traditional design methods. The generated spacecraft design outperforms the intuitive symmetric design of the type

that often outperforms generated designs.

The success criteria for the co-generation algorithm are:

1. Generate a design that can be controlled in a quantifiable volume of state space.
2. Generate a design that is as good or better a intuition-driven human design.

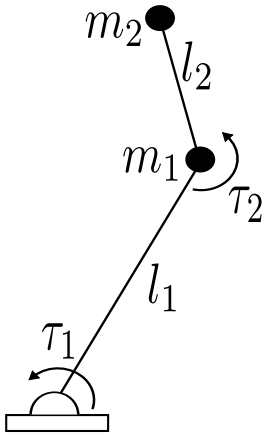

Figure 8.3: The pendulum. Co-generation maximizes the stable states achievable by limited τ_1 and τ_2.

Without criterion 1 the algorithm would be completely useless. Real usefulness comes from criterion 2. Many algorithmic designs succeed at criterion 1 but fail at 2. The human design used as a baseline exhibits the symmetries and even distribution of struts that would intuitively allow the system to stabilize itself in the largest possible state-space volume.

8.4.1 Pendulum

The double pendulum in figure 8.3 is a simple nonlinear system with four states, two actuators - one at each joint, and an analytical equation of motion. Its sim-

plicity means that its amenable to both hand design and other co-generation methods. Using probabilistc co-generation to find a design and controller is overkill. However, the double pendulum is a good baseline system that demonstrates how probabilistic co-generation arrives at the same conclusions as other methods, given enough time.

Equation 8.2 describes the pendulum's dynamics. For abbreviation, $\alpha = m_1 l_1^2 + m_2(l_1^2 + l_2^2)$, $\beta = m_2 l_2^2$, $\delta = m_2 l_2^2$, $c_i = \cos(\theta_i)$, $s_i = \sin(\theta_i)$, $c_{ij} = \cos(\theta_i + \theta_j)$.

$$\begin{bmatrix} \alpha + 2\beta c_2 & \delta + \beta c_2 \\ \delta + \beta c_2 & \delta \end{bmatrix} \begin{bmatrix} \ddot{\theta}_1 \\ \ddot{\theta}_2 \end{bmatrix} + \begin{bmatrix} -\beta s_2 \dot{\theta}_2 & -\beta s_2(\dot{\theta}_1 + \dot{\theta}_2) \\ \beta s_2 \dot{\theta}_1 & 0 \end{bmatrix} \begin{bmatrix} \dot{\theta}_1 \\ \dot{\theta}_2 \end{bmatrix} + \begin{bmatrix} m_1 g l_1 c_1 + m_2 g(l_1 c_1 + l_2 c_{12}) \\ m_2 g l_2 c_{12} \end{bmatrix} = \begin{bmatrix} \tau_1 \\ \tau_2 \end{bmatrix} \tag{8.2}$$

Each of the two actuators saturates at $\tau_i = u_{max}$. These two limited actuators create a non-linear system with four continuous sets of stable points and a state-space that is largely unstable.

The double pendulum has a simple design space: the lengths and masses of its arms, l_i and m_i. The arm mass/length design space has a clear optimum design using the controllable volume metric: minimizing the masses and lengths of the arms gives the actuators maximum control over the pendulum's joint angles. Optimization via MATLAB's `fmincon` confirms the optimality of this design, making it the clear choice as an experimental baseline. The volume of the interconnected RoAs for this design provides a baseline controllable volume.

In figure 8.4, the co-generation algorithm generates designs using increasing values of `max_iterations` in a stochastic search. The generated design's controllable volume approaches the baseline value as `max_iterations` increases, demonstrating convergence on the optimal design. An evolutionary algorithm using controllable volume as a fitness function explores the design space quickly and converges to the optimal values in a few iterations (figure 8.5.)

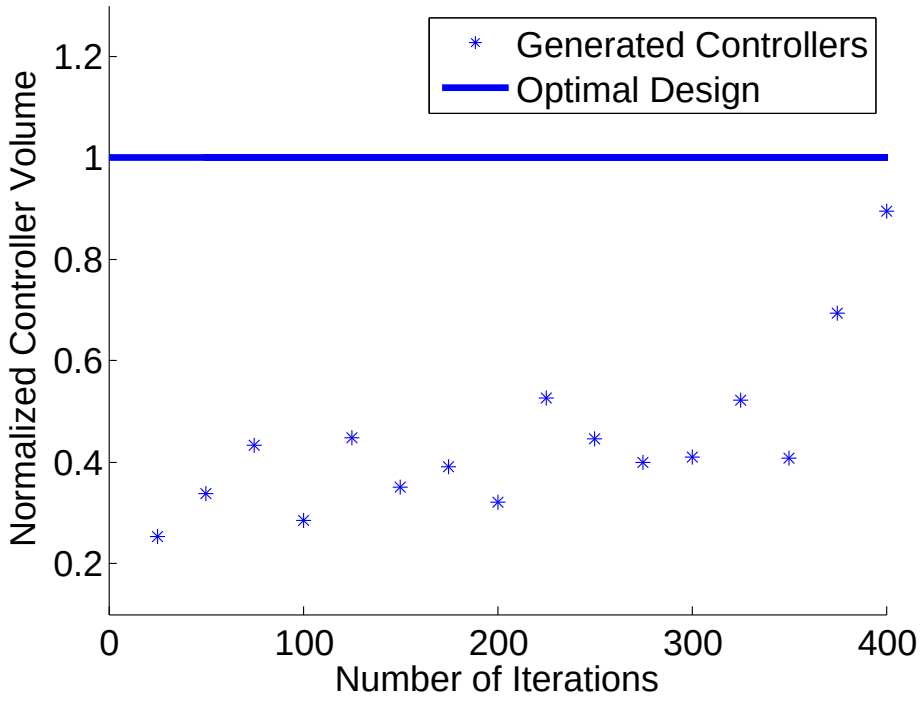

Figure 8.4: The controllable volume of designs generated by a stochastic search converges on the controllable volume of the optimal design. The volumes are normalized by the controllable volume of the optimal design.

8.4.2 Spacecraft

The other test system, an inspection spacecraft, is a complex system that uses novel electromagnetic actuators to interact with a conductive target without contact. The control forces from these actuators are nonlinear, position dependent,

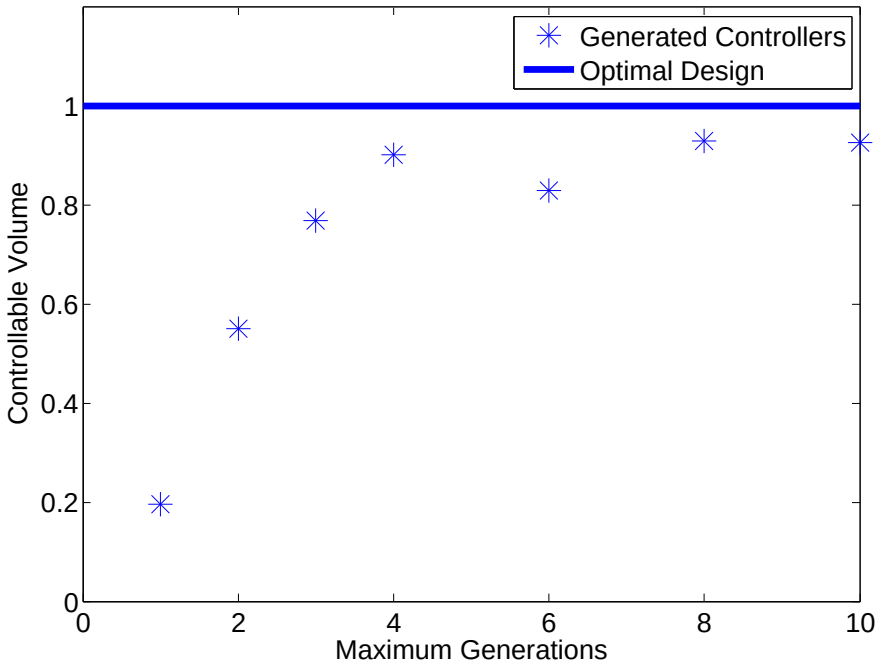

Figure 8.5: The controllable volume of designs generated by a stochastic search converges on the controllable volume of the optimal design. The volumes are normalized by the controllable volume of the optimal design.

and prone to saturation. Coupled with the spacecraft's rigid-body dynamics, the actuators create a system that exhibits all the criteria listed in section 8.1. This complexity causes traditional methods to fall short and motivates the creation of the co-generation algorithm.

The experimental model is a simplified version of a real system currently in development [87]. The model spacecraft is a rigid body with three degrees of freedom (two translational, one rotational.) Struts attach the actuators to the main mass of the system so that the actuators' positions aren't constrained by the inspector's body geometry. The angles between the spacecraft body and the four struts are the free parameters, $\mathbf{p}$, specified during the design of the system. The length of the struts and mass of the spacecraft are fixed parameters, while the position of the surface (that magnetically interacts with the actuators) and

dynamics of the actuators are external environmental variables.

Optimization methods fail to generate designs and controllers for this system, even with a smaller set of parameters than the real system. Both `fmincon` and `SNOPT` can't provide a baseline design because they fail to converge on solutions. This failure drove our new method in the first place. Without optimized designs, a system designer would need to turn to their intuition. The human baseline is this intuitive design that places struts symmetrically spanning the space of possible positions, which ideally would make the system stabilizable in as many configurations as possible.

The results in figure 8.6 show the design and a projection of the control volume for both the human and algorithmically generated design. The designs (subfigures 8.6a and 8.6b) show the body, strut positions, and target surface. Subfigures 8.6c and 8.6d) show 2-d projections of the regions of attraction onto the x-y plane. The baseline design has a stabilizable volume $V_h = 1.14E-11$. After `65` iterations, the algorithm produced a design with a stabilizable volume $V_a = 3.4E-11$. The ratio $\frac{V_a}{V_h} = 2.99$ shows that the algorithm succeeds on both criteria 1 and 2.

Closer inspection of the resulting design yields unexpected insight into the system as well. The algorithm's design consistently places a strut pointed straight down; its actuator as close to the surface as possible. The state-dependence of the actuators explains this placement because their effectiveness decreases with r^4 from the surface. However, there is a trade-off between this arrangement and the human-designed baseline which places actuators farther out to the side to provide more control when the inspector rotates. Post hoc this trade-off is obvious and could be analyzed with traditional methods. However, the size of the design space and complexity of the dynamics completely obscures that clarity during the initial

design process. This insight is specific to the particular model, but it demonstrates how the co-generation algorithm can lead to insights about complex systems. The co-generation leads to both an expanded control volume and a design insight that would have been lost in a traditional design-and-then-controller-synthesis process.

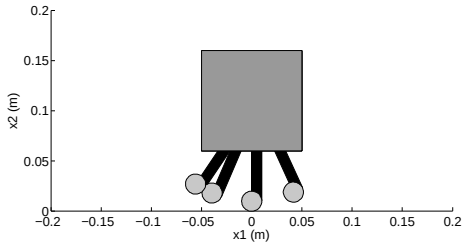

(a) Algorithmic Design

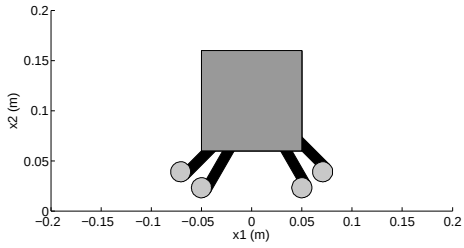

(b) Baseline Design

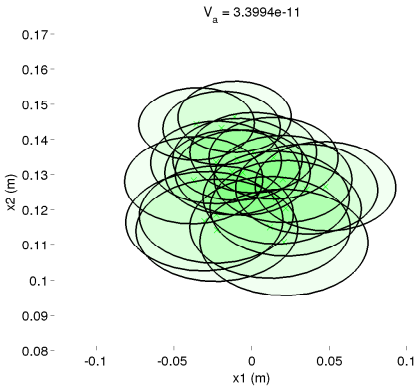

(c) Algorithmic Controller

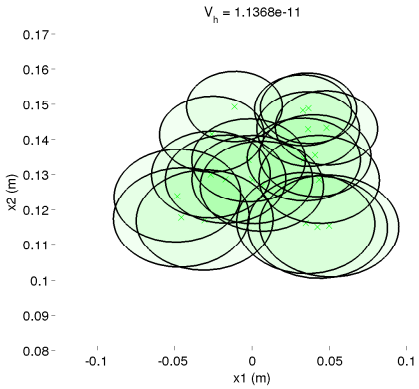

(d) Baseline Controller

Figure 8.6: Algorithmic design and controllers (left) and human design and controllers (right.) The system comprises a main body attached to a set of nonlinear actuators by struts. The co-generation algorithm uses the angles of these struts as the free parameters ($\mathbf{p}$). In an unexpected result, the algorithm showed that symmetry between the four actuators led to less controllable area than a design with a central actuator.

8.5 Discussion

The algorithm presented here is meant as a proof-of-concept for algorithmic design based on a controller metric. There are many possible extensions and areas for future work both in the design and controller halves.

8.5.1 Design

There are multiple methods for generating a design at each iteration. The implementation in this chapter uses two different approaches: a naïve stochastic approach and an evolutionary algorithm. While we used CMA-ES because of its flexibility and convenient implementation, the specific evolutionary algorithm is a mutable design choice. Evolutionary algorithms don't always converge on a global optimum. Their final results depend on the initial design distribution (figure 8.7) and many other parameters. However, evolutionary algorithms' iterative improvements and wide search space support the goal of probabilistic co-creation to generate *feasible* designs and controllers, rather than *optimal* ones.

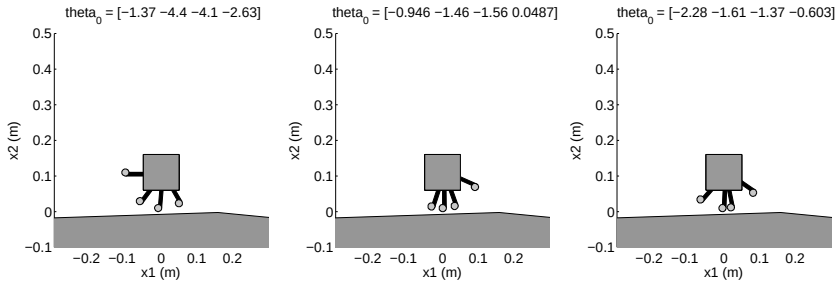

Figure 8.7: Three designs generated by an evolutionary algorithm from random initial distributions. After ten generations, the designs do not converge on an optimum, but all outperform the human baseline.

A gradient-based optimization method using the control volume as a cost function could replace the entire co-generation algorithm if the number of parameters is small and the dynamics are smooth. Most complicated systems don't fulfill these requirements, especially if some parameters can change discretely (three vs. four struts.) Many other algorithms can generate superior simultaneous designs and controllers if the system is amenable to gradient-based optimization.

8.5.2 Control

New center points for new gain nodes can be generated in different ways to maximize coverage or connections between nodes. Selecting only new center points that fall within an existing RoA maximizes connections between nodes; the new node's RoA is guaranteed to intersect the existing RoA, forming a connection. Selecting gain node centers that are already within the RoA of another node guarantees that the control policy described in section 8.2.2 will succeed. Alternately, selecting only new center points that do not fall within, an existing region increases coverage and decrease redundant controllers for the same points. Dynamics-based distance metrics can also be used to pick new center points that are 'dynamically close' to existing regions, leading to new regions that expand coverage and are likely to connect to others [78, 30]. V($\mathcal{C}$) need not necessarily be composed of many LQR regions of attraction. If the dynamics are analytically tractable, SoS can find a single parameterized RoA for the entire range of goal states [55]. This single RoA reduces computation significantly because it requires only one verification but it doesn't lead directly to controller synthesis as a graph of connected gain nodes.

Time-Invariant LQR (TILQR) controllers must be centered around a stable point. This restricts $\mathcal{C}$ to a volume of state space immediately around the set

of goal points while using TILQR gains. Limiting the controller to TILQR gains limits V($\mathcal{C}$), trading volume for consistency. $\mathcal{C}$ could expand farther into state space by including Time-Varying LQR (TVLQR) gains through methods like LQR trees [105]. The trees' TVLQR controllers would stabilize the system to pre-computed trajectories that lead to stable points or other time-varying LQR controllers. LQR trees have verified RoAsthat can add to the V($\mathcal{C}$) design metric. The downside of the expanded control volume is that LQR trees depend on accurate trajectory optimization which can fail to converge for complicated systems, especially when the specific dynamics are unknown a priori because of the design's mutability.

The final control policy need not be limited to jumping between the LQR gains in $\mathcal{C}$. Several different robust on-line planners exist, including Model-Predictive Control (MPC) and LQR trees. These control laws outperform LQR gain hopping most of the time. When using these controllers, $\mathcal{C}$ remains valuable because it can provide constraints for MPC that prevent it from driving the system to an uncontrollable state. Additionally, the gain nodes could provide goal regions for LQR tree generation.

8.6 Summary and Conclusion

Designs for complex dynamical systems often require decisions that can benefit from a tight loop between the design parameters and the control system instead of the traditional approach: design first, controller later. This chapter presents an approach to algorithmic design that uses volume of state space as a metric. This volume acts as a conservative metric for the robustness of the generated controller and by proxy, the quality of the design. The approach is appropriate for high-

dimensional systems with several parameters thanks to its probabilistic nature.

8.7 Conclusion of Part Two

Part II attacked the challenges posed by a robotic inspector locomoting with induction couplers. The inspector is a high-dimensional, nonlinear, dynamical system with state-dependent control authority and actuator limits. Chapter 7 built up motion primitives that allow an induction-coupled inspector to actuate all six rigid-body degrees of freedom. The chapter extended the model from 3 to account for arbitrary coupler orientations, simulated and experimentally demonstrated the motion primitives, and composed them into a full trajectory around an ISS module. An induction inspector's control authority is strongly and non-intuitively coupled to its design. Chapter 8 addressed this challenge by introducing a new probabilistic design and controller generation algorithm for complex nonlinear systems.

8.8 Closing Thoughts

This thesis is a two part exploration into induction couplers. The first part encompasses the space-oriented details of the technology; the second looks at the technology more broadly as a dynamical system through a robotics lens. The reader should come away with three points. First, the theoretical groundwork for future development of induction coupler actuators: models that illustrate their capabilities and limitations. Here, it is important to note that while most of the specific work has focused on permanent-magnet induction couplers, many facts apply to electromagnet-based induction couplers as well.

Second, the reader should learn some practical lessons in building and testing induction couplers and electromagnetic spacecraft systems in a terrestrial environment.

Finally, tools from robotics can be leveraged to enhance human creativity. The probabilistic co-creation algorithm attempts to shine a light in this direction. Until now, a system's complexity and operating limits have been constrained by human ability to analyze them and reason about them. Powerful processors and better numerical models can enable human engineers to work more closely with computers to create previously intractable systems.

BIBLIOGRAPHY

[1] Amir Ali Ahmadi and Pablo a. Parrilo. Towards Scalable Algorithms with Formal Guarantees for Lyapunov Analysis of Control Systems via Algebraic Optimization. *Domino.Research.Ibm.Com*, 25479:11, 2014.

[2] Rob Ambrose, Brian Wilcox, Ben Reed, Larry Matthies, Dave Lavery, and Dave Korsmeyer. Robotics, Tele-Robotics and Autonomous Systems Roadmap. Technical report, NASA, 2012.

[3] Scott Sterling Arnold, Ryan Nuzzaci, and Ann Gordon-Ross. Energy budgeting for CubeSats with an integrated FPGA. In *IEEE Aerospace Conference Proceedings*, pages 1–14, 2012.

[4] Joshua E Auerbach and Josh C Bongard. Dynamic Resolution in the Co-Evolution of Morphology and Control. *Artificial Life XII. Proceedings of the 12th International Conference on the Synthesis and Simulation of Living Systems*, pages 451–458, 2010.

[5] A; Auger and N; Hansen. CMAES Source Code.

[6] Jae-Sung Bae, Jai-Hyuk Hwang, Jung-Sam Park, and Dong-Gi Kwag. Modeling and experiments on eddy current damping caused by a permanent magnet in a conductive tube. *Journal of Mechanical Science and Technology*, 23(11):3024–3035, January 2010.

[7] Young K Bae. A Contamination-Free Ultrahigh Precision Formation Flying Method for Micro- , Nano- , and Pico-Satellites with Nanometer Accuracy. *Space Technology and Applications International Forum - STAIF 2006*, pages 1213–1223, 2006.

[8] R. K. Baerwald and R. S. Passamaneck. Monopropellant thruster exhaust plume contamination measurements. Technical Report ADA048797, 1977.

[9] V Bansal, J D Perkins, E N Pistikopoulos, R Ross, and J M G Van Schijndel. Simultaneous Design and Control Optimisation Under Uncertainty. *Computers and Chemical Engineering*, 24:261–266, 2000.

[10] Kostas E. Bekris and Lydia E. Kavraki. Greedy but safe replanning under kinodynamic constraints. *Proceedings - IEEE International Conference on Robotics and Automation*, (April):704–710, 2007.

[11] Dennis Bernstein, Harris McClamroch, and Anthony Block. Development of Air Spindle and Triaxial Air Bearing Test beds for Spacecraft Dynamics and Control Experiments. In *Proceedings of the American Control Conference*, pages 3967–3972, 2001.

[12] C. P. Bridges, B. Taylor, N. Horri, C. I. Underwood, S Kenyon, J. Barrera-Ars, L Pryce, and R Bird. STRaND-2: Visual inspection, proximity operations & nanosatellite docking. In *IEEE Aerospace Conference Proceedings*, 2013.

[13] O. Brzobohatý, V. Karásek, M. Šiler, L. Chvátal, T. Čižmár, and P. Zemánek. Experimental demonstration of optical transport, sorting and self-arrangement using a tractor beam. *Nature Photonics*, 7(February):1–5, 2013.

[14] R. R. Burridge, Alfred a. Rizzi, and D.E Koditschek. Sequential Composition of Dynamically Dexterous Robot Behaviors. *The International Journal of Robotics Research*, 18(6):534–555, 1999.

[15] E F Camacho and C B Alba. *Model Predictive Control*. Advanced Textbooks in Control and Signal Processing. Springer, 2013.

[16] Thomas E. Carter. State Transition Matrices for Terminal Rendezvous Studies: Brief Survey and New Example. *Journal of Guidance, Control, and Dynamics*, 21(1):148–155, 1998.

[17] H Choset and D Kortenkamp. Path planning and control for free-flying inspection robot in space. *Journal of Aerospace Engineering*, (April):74–81, 1999.

[18] R.S. Clohessy, W.H.; Wiltshire. Terminal Guidance System for Satellite Rendezvous. *Journal of the Aerospace Sciences*, 27(9):653–658, September 1960.

[19] Elliott Coleshill, Layi Oshinowo, Richard Rembala, Bardia Bina, Daniel Rey, and Shelley Sindelar. Dextre: Improving maintenance operations on the International Space Station. *Acta Astronautica*, 64(9-10):869–874, 2009.

[20] D.C. Conner, a.a. Rizzi, and H. Choset. Composition of local potential functions for global robot control and navigation. *Proceedings 2003 IEEE/RSJ International Conference on Intelligent Robots and Systems (IROS 2003) (Cat. No.03CH37453)*, 4(October), 2003.

[21] D.C. Conner, H Choset, and a Rizzi. Towards provable navigation and control of nonholonomically constrained convex-bodied systems. *Proceedings of the 2006 IEEE International Conference on Robotics and Automation (ICRA06)*, (May):4416–4418, 2006.

[22] Freeman J. Dyson. Electron spin resonance absorption in metals. II. Theory of electron diffusion and the skin effect. *Physical Review*, 98:349–359, 1955.

[23] Alex Ellery, Joerg Kreisel, and Bernd Sommer. The case for robotic on-orbit servicing of spacecraft: Spacecraft reliability is a myth. *Acta Astronautica*, 63(5-6):632–648, 2008.

[24] Angel Flores-Abad, Ou Ma, Khanh Pham, and Steve Ulrich. A review of space robotics technologies for on-orbit servicing. *Progress in Aerospace Sciences*, 68:1–26, 2014.

[25] E Frazzoli, M a Dahleh, and E Feron. Real-time motion planning for agile autonomous vehicles. *AIAA Journal of Guidance and Control*, 25(1):116–129, 2002.

[26] Emilio Frazzoli, Munther a. Dahleh, and Eric Feron. Maneuver-based motion planning for nonlinear systems with symmetries. *IEEE Transactions on Robotics*, 21(6):1077–1091, 2005.

[27] Steven E Fredrickson, Larry W Abbott, Steve Duran, J David Jochim, J William Studak, Jennifer D Wagenknecht, and Nichole M Williams. Mini AERCam: development of a free-flying nanosatellite inspection robot. In *Proceedings of SPIE Vol. 5088*, pages 97–111, 2003.

[28] Jessica a. Gersh-Range, William R. Arnold, Mason a. Peck, and H. Philip Stahl. ¡title¿A flux-pinning mechanism for segment assembly and alignment¡/title¿. In James B. Heaney and E. Todd Kvamme, editors, *SPIE Optical Engineering + Applications*, pages 815005–815005–7. International Society for Optics and Photonics, September 2011.

[29] Jeremy H. Gillula, Haomiao Huang, Michael P. Vitus, and Claire J. Tomlin. Design of guaranteed safe maneuvers using reachable sets: Autonomous quadrotor aerobatics in theory and practice. *Proceedings - IEEE International Conference on Robotics and Automation*, pages 1649–1654, 2010.

[30] Elena Glassman and Russ Tedrake. A quadratic regulator-based heuristic for rapidly exploring state space. In *Proceedings - IEEE International Conference on Robotics and Automation*, pages 5021–5028, 2010.

[31] J. Gowdy and a.a. Rizzi. Programming in the architecture for agile assembly. *Proceedings 1999 IEEE International Conference on Robotics and Automation (Cat. No.99CH36288C)*, 4, 1999.

[32] Tomasz M. Grzegorczyk, Johann Rohner, and Jean Marc Fournier. Optical mirror from laser-trapped mesoscopic particles. *Physical Review Letters*, 112(2):23902, January 2014.

[33] a. L. Hale, W. E. Dahl, and . J. Lisowski. Optimal simultaneous structural and control design of maneuvering flexible spacecraft. *Journal of Guidance, Control, and Dynamics*, 8(1):86–93, 1985.

[34] N. Hansen and A. Ostermeier. Adapting arbitrary normal mutation distributions in evolution strategies: the covariance matrix adaptation. *Proceedings of IEEE International Conference on Evolutionary Computation*, 1996.

[35] Kris Hauser, Timothy Bretl, Kensuke Harada, and Jean-Claude Latombe. Using Motion Primitives in Probabilistic Sample-Based Planning for Humanoid Robots. In Srinivas Akella, NancyM. Amato, WesleyH. Huang, and Bud Mishra, editors, *Algorithmic Foundation of Robotics VII SE - 32*, volume 47 of *Springer Tracts in Advanced Robotics*, pages 507–522. Springer Berlin Heidelberg, 2008.

[36] Gregory S. Hornby, Hod Lipson, and Jordan B. Pollack. Generative representations for the automated design of modular physical robots. *IEEE Transactions on Robotics and Automation*, 19(4):703–719, 2003.

[37] J W Hurst, J E Chestnutt, and a a Rizzi. Design and Philosophy of the {B}i{MASC}, a Higly Dynamic Biped. *Proceedings of the IEEE International Conference of Robotics and Automation*, pages 1863–1868, 2007.

[38] Aaron Jacobovits and A Street. SSC03-IV-7 AeroAstro s Escort A Microsatellite for On-Orbit Inspection of Space Assets. In *17th Annual AIAA/USU Conference on Small Satellites*, pages 1–9, Logan, Utah, 2003.

[39] Jian-Ming Jin and Jiamming Jin. *The finite element method in electromagnetics*. Wiley, 2002.

[40] Raphael Kajiwara, I.; Haftka. Simultaneous Optimum Design of Shape and Control System for Micro Air Vehicles. In *40TH Structures, Structural Dynamics, and Materials Conference and Exhibit*, 1999.

[41] Marshall H Kaplan, Bradley Boone, Robert Brown, Thomas B Criss, and Edward W Tunstel. Engineering Issues for All Major Modes of In Situ Space Debris Capture. In *AIAA 2010 Conference & Exposition*, number September, pages 1–20, Anaheim, California, 2010.

[42] Sertac Karaman and Emilio Frazzoli. Sampling-based optimal motion planning for non-holonomic dynamical systems. *2013 IEEE International Conference on Robotics and Automation*, pages 5041–5047, May 2013.

[43] L.E. Kavraki, L.E. Kavraki, P. Svestka, P. Svestka, J.-C. Latombe, J.-C. Latombe, M.H. Overmars, and M.H. Overmars. Probabilistic roadmaps for path planning in high-dimensionalconfiguration spaces. *Robotics and Automation, IEEE Transactions on*, 12(4):566 – 580, 1996.

[44] Lb King and Gg Parker. Spacecraft formation-flying using inter-vehicle coulomb forces. Technical report, 2002.

[45] De Koditschek. The application of total energy as a Lyapunov function for mechanical control systems. In *Dynamics and control of multibody systems*, pages 131–156. American Mathematical Soc., 1989.

[46] Edmund M.C. Kong, Daniel W. Kwon, Samuel a. Schweighart, Laila M. Elias, Raymond J. Sedwick, and David W. Miller. Electromagnetic Formation Flight for Multisatellite Arrays. *Journal of Spacecraft and Rockets*, 41(4):659–666, 2004.

[47] Ioannis K. Kookos and John D. Perkins. An Algorithm for Simultaneous Process Design and Control. *Industrial & Engineering Chemistry Research*, 40:4079–4088, 2001.

[48] Keith Kotay, Daniela Rus, Marsette Marty Vona, and Craig McGray. The self-reconfiguring robotic molecule: Design and control algorithms. In *Workshop on Algorithmic Foundations of Robotics*, pages 376–386. Citeseer, 1998.

[49] Huibert Kwakernaak and Raphael Sivan. *Linear optimal control systems*, volume 1. Wiley-Interscience New York, 1972.

[50] Elisabeth Lamassoure, Joseph H. Saleh, and Daniel E. Hastings. Space Systems Flexibility Provided by On-Orbit Servicing: Part 2. *Journal of Spacecraft and Rockets*, 39(4):561–570, 2002.

[51] S.M. LaValle and Jr. Kuffner, J.J. Randomized kinodynamic planning. *International Journal of Robotics Research*, 20(5):378–400, 2001.

[52] T. Lozano-Perez, M. T. Mason, and R. H. Taylor. Automatic Synthesis of Fine-Motion Strategies for Robots. *The International Journal of Robotics Research*, 3:3–24, 1984.

[53] Yong Lu, Mingliang Zhang, and Dong Gao. Connection stiffness and dynamical docking process of flux pinned spacecraft modules. *Journal of Applied Physics*, 115(6):063904, February 2014.

[54] Zahid Mahimwalla, Kevin G Yager, Jun-ichi Mamiya, Atsushi Shishido, and Christopher J Barrett. *Optical Nano and Micro Actuator Technology*. Taylor & Francis, 2012.

[55] Anirudha Majumdar. Algebraic verification for parameterized motion planning libraries. In *American Control Conference*, pages 250–257, 2012.

[56] Gennady Markelov, Rolf Brand, Georg Ibler, and Wolfgang Supper. Numerical assessment of plume heat and mechanical loads and contamination on multi-layer insulation in hard vacuum. *Vacuum*, 86(7):889–894, 2012.

[57] M. T. Mason. The Mechanics of Manipulation. In *Robotics and Automation. Proceedings. 1985 IEEE International Conference on (Volume:2)*, pages 544–548, 1985.

[58] S. Matsumoto, Y. Ohkami, Y. Wakabayashi, M. Oda, and H. Ueno. Satellite capturing strategy using agile Orbital Servicing Vehicle, Hyper-OSV. *Proceedings 2002 IEEE International Conference on Robotics and Automation (Cat. No.02CH37292)*, 3(May), 2002.

[59] A. Megretski. Systems polynomial optimization tools (SPOT), 2010.

[60] H.F.; Meissinger and J. Collins. Mission Design and System Requirements for a Multiple-Function Orbital Transfer Vehicle. In *AIAA Space Technology Conference*, number September, pages 1–11, 1999.

[61] I.M. Mitchell, a.M. Bayen, and C.J. Tomlin. A time-dependent Hamilton-Jacobi formulation of reachable sets for continuous dynamic games. *IEEE Transactions on Automatic Control*, 50(7):947–957, July 2005.

[62] S. Ali a. Moosavian and Evangelos Papadopoulos. Free-flying robots in space:

an overview of dynamics modeling, planning and control. *Robotica*, 25(March 2007):537–547, 2007.

[63] Arun Natarajan and Hanspeter Schaub. Linear dynamics and stability analysis of a coulomb tether formation. *Advances in the Astronautical Sciences*, 120(4):1635–1649, July 2005.

[64] Arun Natarajan and Hanspeter Schaub. Linear dynamics and stability analysis of a coulomb tether formation. *Advances in the Astronautical Sciences*, 120(4):1635–1649, 2005.

[65] Arun Natarajan, Hanspeter Schaub, and Gordon G Parker. Aas 06-229 Reconfiguration of a 2-Craft Coulomb Tether. *Aerospace*, 60:209–218, 2007.

[66] Thai Chau Nguyen-Huynh and Inna Sharf. Adaptive reactionless motion for space manipulator when capturing an unknown tumbling target. *Proceedings - IEEE International Conference on Robotics and Automation*, pages 4202–4207, May 2011.

[67] Michael C. Norman and Mason a. Peck. Simplified Model of a Flux-Pinned Spacecraft Formation. *Journal of Guidance, Control, and Dynamics*, 33(3):814–822, May 2010.

[68] Michael C. Norman and Mason a. Peck. Stationkeeping of a Flux-Pinned Satellite Network. *Journal of Guidance, Control, and Dynamics*, 33(5):1683–1687, September 2010.

[69] Andrew Ogilvie, Justin Allport, Michael Hannah, and John Lymer. Autonomous robotic operations for on-orbit satellite servicing. *SPIE Defense and Security Symposium*, pages 1–12, 2008.

[70] Takahisa Ohji, Hiroaki Hara, Kenji Amei, and Masaaki Sakui. Three-dimensional motion of a small object by using a new magnetic levitation system having four I-shaped electromagnets. *IEEE Transactions on Magnetics*, 44(11):4159–4162, November 2008.

[71] Takahisa Ohji, Masaaki Sato, Kenji Amei, and Masaaki Sakui. Generation of method AC ampere force using eddy current inside a nonmagnetic thin plate and its effect on electrodynamic suspension. *Electrical Engineering in Japan (English translation of Denki Gakkai Ronbunshi)*, 170(3):48–56, February 2010.

[72] N Jehnson P, Westphal M, and Schuff. Analytical method for the compensation of eddy-current effects induced by pulsed magnetic field gradients in NMR systems. *Journal of Magnetic Resonance (1969)*, 90:264–278, 1990.

[73] Stephen Papachristodoulou, Antonis; Prajna. the Sum of Squares Decomposition '. In *2002 Proceedings of the 41st IEEE Conference on Decision and Control*, volume 3, pages 3482–3487, 2002.

[74] G.G. Parker, L.B. King, and H. Schaub. Steered spacecraft deployment using interspacecraft Coulomb forces. In *2006 American Control Conference*, pages 6—-pp. IEEE, 2006.

[75] Nirmal Paudel and Jonathan Z. Bird. Modeling the Dynamic Electromechanical Suspension Behavior of an Electrodynamic Eddy Current Maglev Device. *Progress In Electromagnetics Research B*, 49(February):1–30, 2013.

[76] Nirmal Paudel, S Paul, and Jz Bird. General 2-D transient eddy current force equations for a magnetic source moving above a conductive plate. *Progress In Electromagnetics Research B*, 43(July):255–277, 2012.

[77] Subhra Paul, Walter Bomela, Nirmal Paudel, and Jonathan Z. Bird. 3-D eddy current torque modeling. *IEEE Transactions on Magnetics*, 50(2):905–908, February 2014.

[78] Alejandro Perez, Robert Platt, George Konidaris, Leslie Kaelbling, and Tomas Lozano-Perez. LQR-RRT*: Optimal sampling-based motion planning with automatically derived extension heuristics. In *Proceedings - IEEE International Conference on Robotics and Automation*, number 0, pages 2537–2542, 2012.

[79] Giordano Pola, Antoine Girard, and Paulo Tabuada. Approximately bisimilar symbolic models for nonlinear control systems. *Automatica*, 44:2508–2516, 2008.

[80] E. Bou Porter, A.K., D.J. Alinger, R.J. Sedwick, J. Merk, R.A.Opperman, A. Buck, G. Eslinger, P. Fisher, D.W., Miller. RINGS: Demonstration of Electromagnetic Formation Flight and Wireless Power Transfer, 2013.

[81] N. Praly, M. Hillion, C. Bonnal, J. Laurent-Varin, and N. Petit. Study on the eddy current damping of the spin dynamics of space debris from the Ariane launcher upper stages. *Acta Astronautica*, 76:145–153, July 2012.

[82] Subramanian Ramamoorthy and Benjamin Jack Kuipers. Controller Synthesis using Qualitative Models and Constraints. *Computer*, 2002.

[83] J.S. Rastegar, Lidong Liu Lidong Liu, and D. Yin. Task-specific optimal simultaneous kinematic, dynamic, and control design of high-performance robotic systems. *IEEE/ASME Transactions on Mechatronics*, 4(4):387–395, 1999.

[84] Thambirajah Ravichandran, David Wang, and Glenn Heppler. Simultaneous plant-controller design optimization of a two-link planar manipulator. *Mechatronics*, 16:233–242, 2006.

[85] Benjamin Reinhardt, Brandon Hencey, and Mason Peck. Characterization of Eddy Currents for Space Actuation. In *AIAA/AAS Astrodynamics Specialist Conference*. American Institute of Aeronautics and Astronautics, 2012.

[86] Benjamin Reinhardt and Mason Peck. Eddy-Current Space Tug. In *AIAA Space 2011 Conference and Exposition*, Long Beach, CA, 2011. AIAA.

[87] Benjamin Reinhardt and Mason Peck. A New Actuator for On-Orbit Inspection. In *Proceedings of the AIAA/USU Conference on Small Satellites*, 2014.

[88] Philipp Reist and Russ Tedrake. Simulation-based LQR-trees with input and state constraints. *Proceedings - IEEE International Conference on Robotics and Automation*, pages 5504–5510, 2010.

[89] P C Rem and P A Leest. A model for eddy current separation. 16(96), 1997.

[90] Luis a. Ricardez-Sandoval, Hector M. Budman, and Peter L. Douglas. Application of Robust Control Tools to the Simultaneous Design and Control of Dynamic Systems. *Industrial & Engineering Chemistry Research*, 48:801–813, 2009.

[91] Luis a. Ricardez-Sandoval, Hector M. Budman, and Peter L. Douglas. Simultaneous design and control: A new approach and comparisons with existing methodologies. *Industrial and Engineering Chemistry Research*, 49:2822–2833, 2010.

[92] Hanspeter Schaub and Islam I. Hussein. Stability and reconfiguration analysis of a circularly spinning two-craft Coulomb tether. *IEEE Transactions on Aerospace and Electronic Systems*, 46(4):1675–1686, 2010.

[93] Jana L Schwartz, Mason A Peck, and Christopher D Hall. Historical Review of Air-Bearing Spacecraft Simulators Introduction. *Journal of Guidance Control and Dynamics*, 26(4):513–522, 2003.

[94] Samuel Adam Schweighart, Raymond J Sedwick, and Samuel Adam Schweighart. *Electromagnetic Formation Flight Dipole Solution Planning*. PhD thesis, MIT, 2005.

[95] POM Scokaert and JB Rawlings. Constrained linear quadratic regulation. *IEEE Transactions on Automatic Control*, 43(8):1163–1169, 1998.

[96] Joseph P. Shoer and Mason a. Peck. Flux-Pinned Interfaces for the Assembly, Manipulation, and Reconfiguration of Modular Space Systems. *The Journal of the Astronautical Sciences*, 57(3):667–688, March 2013.

[97] W.R Smyth. *Static & Dynamic Electricity*. 5th edition, 1989.

[98] J. Sobieszczanski-Sobieski and R. T. Haftka. Multidisciplinary aerospace design optimization: survey of recent developments. *Structural Optimization*, 14(Berkes 1990):1–23, 1997.

[99] Henry a. Sodano and Daniel J. Inman. Modeling of a New Active Eddy Current Vibration Control System. *Journal of Dynamic Systems, Measurement, and Control*, 130(2):021009, 2008.

[100] Henry a. Sodano and Daniel J. Inman. Modeling of a New Active Eddy Current Vibration Control System. *Journal of Dynamic Systems, Measurement, and Control*, 130(2):021009, 2008.

[101] Hanspeter Stevenson, Daa; Schaub. Terrestrial testbed for remote Coulomb spacecraft rotation control Daan Stevenson * and Hanspeter Schaub. *International Journal Space Science and Engineering*, 2(1):96–112, 2014.

[102] R L Stoll. *The analysis of eddy currents*. Oxford University Press, London, 1974.

[103] Fumihito Sugai, Satoko Abiko, Teppei Tsujita, Xin Jiang, and Masaru Uchiyama. Development of an Eddy Current Brake System for Detumbling. pages 8–13, 2012.

[104] Brook R. Sullivan, David Barnhart, Lisa Hill, Paul Oppenheimer, Bryan Benedict, Gerrit van Ommering, Laurie Chappell, John Ratti, and Peter

Will. DARPA Phoenix Payload Orbital Delivery (POD) System: FedEx to GEO. *Proceedings of the AIAA SPACE Conference*, pages 1–14, 2013.

[105] R. Tedrake, I. R. Manchester, M. Tobenkin, and J. W. Roberts. LQR-trees: Feedback Motion Planning via Sums-of-Squares Verification. *The International Journal of Robotics Research*, 29:1038–1052, 2010.

[106] Peter Terren. Tesla Downunder.

[107] Mark M. Tobenkin, Ian R. Manchester, and Russ Tedrake. Invariant funnels around trajectories using Sum-of-Squares programming. *IFAC Proceedings Volumes (IFAC-PapersOnline)*, 18(1):9218–9223, 2011.

[108] Be Tweddle. Relative computer vision based navigation for small inspection spacecraft. In *AIAA Guidance, Navigation and Control Conference*, number August, pages 1–15, 2011.

[109] Donald M. Waltz. *On-orbit servicing of space systems*. Krieger Pub Co, original edition, 1993.

[110] Shuquan Wang and Hanspeter Schaub. Spacecraft collision avoidance using Coulomb forces with separation distance feedback. *Advances in the Astronautical Sciences*, 127 PART 1(3):197–216, 2007.

[111] J R Wertz, D F Everett, and J J Puschell. *Space Mission Engineering: The New SMAD*. Space technology library. Microcosm Press, 2011.

[112] L.L. Whitcomb. Underwater robotics: out of the research laboratory and into the field. *Proceedings 2000 ICRA. Millennium Conference. IEEE International Conference on Robotics and Automation. Symposia Proceedings (Cat. No.00CH37065)*, 1:709–716, 2000.

[113] William R. Wilson, Laura L. Jones, and Mason a. Peck. A Multimodule Planar Air Bearing Testbed for CubeSat-Scale Spacecraft. *Journal of Dynamic Systems, Measurement, and Control*, 135(4):045001, May 2013.

[114] Z. P. Xia, Z. Q. Zhu, and David Howe. Analytical magnetic field analysis of halbach magnetized permanent-magnet machines. *IEEE Transactions on Magnetics*, 40(4):1864–1872, 2004.

[115] Wenfu Xu, Bin Liang, Bing Li, and Yangsheng Xu. A universal on-orbit

servicing system used in the geostationary orbit. *Advances in Space Research*, 48(1):95–119, 2011.

[116] Wenfu Xu, Bin Liang, Cheng Li, Yu Liu, and Yangsheng Xu. Autonomous target capturing of free-floating space robot: Theory and experiments. *Robotica*, 27(03):425, July 2009.

[117] X. Yao and T. Higuchi. Promises and challenges of evolvable hardware. *IEEE Transactions on Systems, Man, and Cybernetics, Part C (Applications and Reviews)*, 29(1):87–97, 1999.

[118] Mark Yim, Wei-Min Shen, Benham Salemi, Daniela Rus, Mark Moll, Hod Lipson, and Eric Klavins. Modular Self-reconfigurable Robot Systems: Challenges and Opportunities for the Future. {*IEEE*} *Robotics \& Automation Magazine*, 14(March):43–52, 2007.